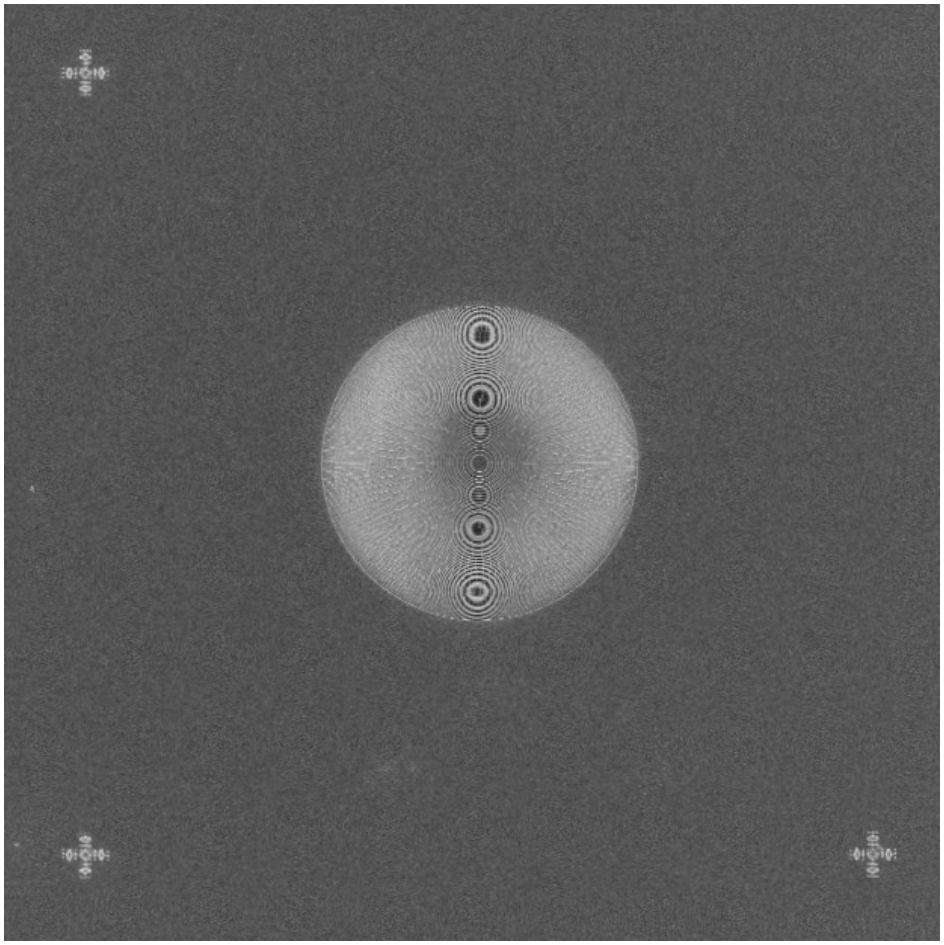

Fabrication of double-sided Fresnel zone plates and absolute measurements of their diffraction efficiency in an X-ray-tube-based setup

Master's thesis in Nanotechnology

VIKTORIA YURGENS

Department of Microtechnology and Nanoscience
CHALMERS UNIVERSITY OF TECHNOLOGY
Gothenburg, Sweden 2019

Master's thesis 2019

Fabrication of double-sided Fresnel zone plates and absolute measurements of their diffraction efficiency in an X-ray-tube-based setup

VIKTORIA YURGENS

Department of Microtechnology and Nanoscience
Photonics Laboratory
Chalmers University of Technology
Gothenburg, Sweden 2019

Fabrication of double-sided Fresnel zone plates and absolute measurements of their diffraction efficiency in an X-ray-tube-based setup
VIKTORIA YURGENS

Supervisors:
Dr. Frieder Koch, Laboratory for Micro and Nanotechnology, Paul Scherrer Institute
Dr. Christian David, Laboratory for Micro and Nanotechnology, Paul Scherrer Institute
Examiners:
Prof. Jörgen Bengtsson, Department of Microtechnology and Nanoscience, Chalmers University of Technology
Prof. Åsa Haglund, Department of Microtechnology and Nanoscience, Chalmers University of Technology

Department of Microtechnology and Nanoscience
Photonics Laboratory
Chalmers University of Technology
SE-412 96 Gothenburg
Telephone +46 31 772 1000

Cover: Scanning electron microscope image of a Fresnel zone plate with 100 μm diameter and 50 nm outermost zone width, of the type fabricated and tested in the thesis. The three cross-like features show the marker search performed in the electron beam lithography alignment step, where the zone plate on the frontside of the silicon nitride membrane is aligned to the identical zone plate on the backside of it.

Typeset in LaTeX
Gothenburg, Sweden 2019

Fabrication of double-sided Fresnel zone plates and absolute measurements of their diffraction efficiency in an X-ray-tube-based setup

VIKTORIA YURGENS
Department of Microtechnology and Nanoscience
Chalmers University of Technology

Abstract

Diffractive lenses for X-rays, so-called Fresnel zone plates (FZPs), are used as focusing elements in X-ray imaging applications in synchrotrons all over the world. One of the main characteristics of FZPs is their diffraction efficiency. Measurements of the absolute diffraction efficiency as a function of the X-ray energy can reliably be done using synchrotron radiation, but require beamtime at synchrotrons which is not available on a routine basis. Here, the design, construction and characterization of an in-lab X-ray-tube-based setup for measuring the absolute diffraction efficiency of single- and double-sided FZPs is presented. The broad spectrum from the X-ray tube is monochromatized using a set of copper- and nickel filters, giving an approximate X-ray energy of 8.4 keV; the spectrum is simulated and confirmed through spectrometer measurements. Single- and double-sided line-doubled Fresnel zone plates with different characteristics have been fabricated and measured using the setup, yielding absolute diffraction efficiencies of up to 6.4%. Diffraction efficiency maps, showing the spatial distribution of the diffraction efficiency, have been obtained for each zone plate. The measurements have given important information regarding issues with the fabrication process related to the alignment between the two halves of double-sided zone plates, and these issues have been investigated further. Finally, measurements have been performed where the misalignment in double-sided zone plates has been determined by employing a functionality of the setup where the measured zone plates can be tilted around two different axes.

Keywords: X-ray optics, Fresnel zone plate, absolute diffraction efficiency, Moiré pattern, zone plate misalignment, laboratory X-ray source, X-ray spectrum, X-ray microscopy.

Acknowledgements

I would first of all like to thank my supervisors at Paul Scherrer Institute (PSI): Frieder Koch, for his patience, willingness to help and wonderfully pedagogic way of explaining, and Christian David, for giving me the opportunity to write a master's thesis on this subject, and for always taking the time to discuss, advise or construct things with me. I am also very thankful to the rest of the *X-ray Optics and Applications* group at PSI – Florian Döring, Adam Kubec, Maxime Lebugle, Vitaliy Guzenko, Benedikt Rösner, Gediminas Seniutinas, and Eugen Deckardt – for their positivity, help and valuable advice, and for always having a good time regardless of the results in the lab. I would also like to thank all of the members of the Laboratory for Micro- and Nanotechnology at PSI – from my very first day I have felt welcome and never had a doubt that I can ask for help or guidance, be it inside the cleanroom or outside of it. It is a great laboratory to work in and I feel very lucky to have been a part of it.

I am grateful to Anna Bergamaschi from the *SLS Detectors* group at PSI for the support about the MÖNCH03 detector, and to Joan Vila-Comamala from the TOMCAT - X02DA beamline of the Swiss Light Source for lending and instructing me about the Amptek X-ray spectrometer. I am thankful to Timm Weitkamp, Mario Scheel, and Jonathan Perrin from the ANATOMIX beamline at Synchrotron SOLEIL for letting me take part in the commissioning of the beamline and for giving me insights into the immense work and knowledge needed behind it.

Last but not least I would like to thank my examiners at Chalmers University of Technology, Jörgen Bengtsson and Åsa Haglund, for their valuable comments and encouragement during the course of my work. It was always highly appreciated.

Viktoria Yurgens, Villigen, January 2019

Contents

List of Figures

List of Tables

1
Introduction

X-ray imaging has a wide range of applications covering areas from physics, chemistry and biology to medical science, materials science and archaeology [1]. Progress in X-ray microscopy [2] has made sub-micron and nanometer resolutions possible, much thanks to the development of third-generation synchrotron sources with highly coherent and extremely brilliant light. Together with the improvements in micro-focusing optics for hard X-rays[1], the progress is steadily moving towards even smaller resolutions, shorter acquisition times and new opportunities in the many research fields employing synchrotron radiation [3, 4].

Hard X-rays can be focused using either reflective, refractive or diffractive optics, with the latter class consisting of so-called Fresnel zone plates (FZPs). In collaboration with Synchrotron SOLEIL [5], a synchrotron facility near Paris, France, members of the *X-ray Optics and Applications* group at the Paul Scherrer Institute, Villigen, Switzerland [6], are working on the fabrication of FZPs for ANATOMIX [7], one of the synchrotron's beamlines. The ANATOMIX beamline for X-ray tomography enables high-resolution radiographic imaging of hundred nanometer- to several centimeter thick samples, as well as real-time and *in situ* studies of samples without previous dehydration or chemical fixation. The beamline is intended to be used for transmission X-ray microscopy (TXM) at photon energies up to as high as 18 keV.

FZP-based hard X-ray TXM is performed only at a few synchrotrons in the world, among which is the beamline 6-2c at the Stanford Synchrotron Radiation Lightsource, operating at energies from 4.5 to 13 keV [8], the P05 beamline at PETRA III, using energies between 5 and 50 keV [9], the I13 beamline at the Diamond Light Source, operating at energies from 8 to 30 keV [10], and the TOMCAT beamline of the Swiss Light Source, employing energies between 8 and 45 keV [11]. To efficiently focus light with energies as high as these, one needs to have FZPs with extreme structure aspect ratios – the size of the focus is determined by the zone plate lateral dimensions, and the required height of the zone plate structures increases with increasing energy. Due to the limitations in the fabrication process this means that tricks such as fabricating double-sided zone plates [12] need to be employed. Such approaches, however, suffer from alignment problems.

[1] Hard X-rays typically refer to X-rays with energies between a few and several hundred keV, whereas soft X-rays are usually considered to be X-rays with energies between about 100 eV and 2 keV [3].

1.1 Preliminary aim and objectives

Due to the access to synchrotron beamlines in general being very rare, it is not possible to continuously test the quality of the Fresnel zone plates being fabricated by the *X-ray Optics and Applications* group for the ANATOMIX beamline. This leads to the aims of this thesis:

1.1.1 Preliminary aim of thesis

In order to get updated information about the zone plate fabrication process, the diffraction efficiency, and the possible misalignment in double-sided zone plates, the group needs an in-lab setup for these types of measurements. The purpose of this master's thesis was therefore to build and characterize such a lab-based X-ray-tube setup, made for measuring the diffraction efficiency and alignment of both single- and double-sided Fresnel zone plates, enabling routine tests without any dependency on synchrotron beamtimes, and accelerating and improving the zone plate optimization process to a great extent. In addition, a goal was to independently be able to fabricate single- and double-sided FZPs according to the requirements set by the team at ANATOMIX, which ordered zone plates for the energies 6 keV, 10 keV and 18 keV.

At the start of this master's thesis, the group already had an X-ray-tube-based setup for measuring the diffraction efficiency of zone plates. This setup, however, gave only the relative efficiency, gave no information about the performance of different parts of the zone plates, and relied on measurements performed at synchrotrons. A new setup, with added functionality in terms of a spatially resolved and absolute-valued map of the zone plate diffraction efficiency, together with the possibility of measuring the misalignment in double-sided FZP, was therefore of great importance to the group.

1.1.2 Interim objective

The half-time goal for the master's thesis was to independently have fabricated and characterized at least one chip of functioning single-sided FZPs, and to have built a rough but operational setup consisting of a new detector and microfocus X-ray tube with which absolute and spatially resolved diffraction efficiency measurements could be performed. During the second half of the project the functionality of alignment measurements between the two halves of double-sided FZPs would be added to the setup. At the end of the project at least one chip with double-sided zone plates should independently have been fabricated and fully characterized with the new setup. Furthermore, a standard procedure for testing zone plates with the new setup and performing data analysis should have been developed.

1.1.3 Demarcations

Single- and double-sided iridium (Ir) line-doubled FZPs, such as as those made by Mohacsi *et al* [12], were the only zone plates fabricated in this project. Other types, such as gold zone plates [13] or hybrid-level zone plates [14], were not considered.

Optimization of the zone plate fabrication process could be made, but the development of completely new fabrication methods was out of the scope of the thesis due to the time limitation. The setup was made specifically for measurements on hard X-ray objective zone plates – other types of optics, such as gratings, condensers, and refractive optics, were not considered in the setup design.

1.2 Societal, ethical and ecological aspects

The main idea behind the thesis was to be able to do efficiency measurements of FZPs in-lab instead of at a synchrotron. The quality of such measurements will not be the same as with the highly coherent and brilliant synchrotron light, but they will nevertheless give values for the efficiency of zone plates, speeding up the optimization of the fabrication process and reducing the need for travelling to a synchrotron. This can be presented as a substantial environmental argument in favour of building the setup. However, considering the amount of energy that a synchrotron uses, the environmental impact of the travels to and from a synchrotron is almost negligible. Nevertheless, saving beamtime for truly necessary measurements will in any case mean that the energy resources are used in an optimized way and only for the experiments that need them. The development of more efficient diffractive optics will also mean that samples can be measured faster and with a smaller radiation dose.

Most of the ethical problems in scientific studies arise when living organisms are involved. This master's thesis did not involve any living beings, which makes it simpler to motivate from an ethical point of view. One could however discuss whether building and running an enormous synchrotron, with its ground area requirements, potential dangers and radiation damage issues is really worth the results it produces. The fact that until now, 16 Nobel Prizes in physics, chemistry and medicine, including the 1962 prize for the discovery of the structure of DNA, have been awarded to studies related to X-ray research [3], makes it more forgivable and indicates the importance of X-ray radiation in a range of research fields. One can argue that synchrotron radiation sources are necessary for a continued scientific progress in the world. Advances in X-ray microscopy, used in a wide range of research applications, will most certainly have a positive impact as well.

Most X-ray optics can only be made inside a cleanroom, which with all of its equipment, chemicals, and generally large use of resources has a negative impact on the environment. One can, however, again use the argument about the improvement in technology that a cleanroom contributes to, making its maintenance a reasonable sacrifice. The positive aspect of doing processing in a carefully controlled environment with well-developed equipment and experienced users, should also be taken into account.

2

Theory

The topic of this thesis is the fabrication of single- and double-sided zone plates for transmission X-ray microscopy, and the testing of them in a setup based on a laboratory X-ray source. The required background knowledge on diffractive optics, X-ray production, radiation safety and X-ray microscopy is presented here.

2.1 Fresnel zone plates

In this section, the characteristics of Fresnel zone plates are presented together with a description of their fabrication, diffraction efficiency and issues that can arise when overlaying two zone plates in a double-sided structure.

2.1.1 Characteristics

Fresnel zone plates are used as focusing elements in a range of soft and hard X-ray imaging applications in synchrotrons all over the world. They are in their most common form circular gratings consisting of a series of concentric rings, or *zones*, with gradually decreasing widths towards the periphery. The series consists of alternating phase-shifting and transparent zones, spaced so that light which is transmitted through the zone plate interferes constructively at a wanted focal distance. The interference happens due to a relative phase- or amplitude difference induced in beams emerging from neighbouring zones [4, 15].

The focal length f of an FZP given its diameter d, outermost zone width dr and the wavelength of the incoming light λ can be calculated using the formula

$$f = \frac{d \cdot dr}{\lambda}, \tag{2.1}$$

derived from the condition that constructive interference of light from two neighbouring transparent zones occurs only when the difference in optical path length is equal to an integer number of wavelengths. The resolution of the zone plate when assuming a diffraction-limited optical system can be derived as

$$w = \frac{\lambda}{2 \cdot \mathrm{NA}} = \frac{\lambda}{2 \cdot \sin\theta} = \frac{\lambda}{2}\frac{2 \cdot dr}{\lambda} = dr \tag{2.2}$$

using that the numerical aperture is $\mathrm{NA} = \sin\theta$, with θ being the angle of the first-order diffracted light, and locally seeing the alternating zones of the FZP as a diffraction grating with a pitch of $p = 2 \cdot dr$. The grating equation subsequently

gives $\sin\theta = \frac{\lambda}{d}$ and the result is that the resolution is determined by the width of the outermost zone [15]. This is why zone plates for high-resolution imaging need to be fabricated with extremely narrow outermost zone widths.

The working distance of a ZP, relevant in the case when the illumination is at a finite distance from the structure, can be determined from the lens equation:

$$\frac{1}{g} + \frac{1}{b_1} = \frac{1}{f} \tag{2.3}$$

with b_1 being the working distance, f the focal length and g the distance between the source point and the zone plate.

Figure 2.1a schematically illustrates the focusing performed by a zone plate. Indicated is the zone plate radius $R = d/2$, the outermost zone width dr, the radius of the nth zone r_n, the focal length f and the path lengths of light emerging from two neighbouring zones. Figure 2.1b shows a scanning electron microscope (SEM) image of a real zone plate. The inset shows an enlarged view of the zones closest to the center. Visible are also some of the support structures, which are introduced in the design to stabilize the most narrow zones. The circular patterns covering the zone plate in the image are so-called Moiré fringes, a visual artifact which in this case arises from interference between the pixels of the camera in the microscope and the zone plate pattern. Moiré patterns are introduced further in Section 2.1.4.

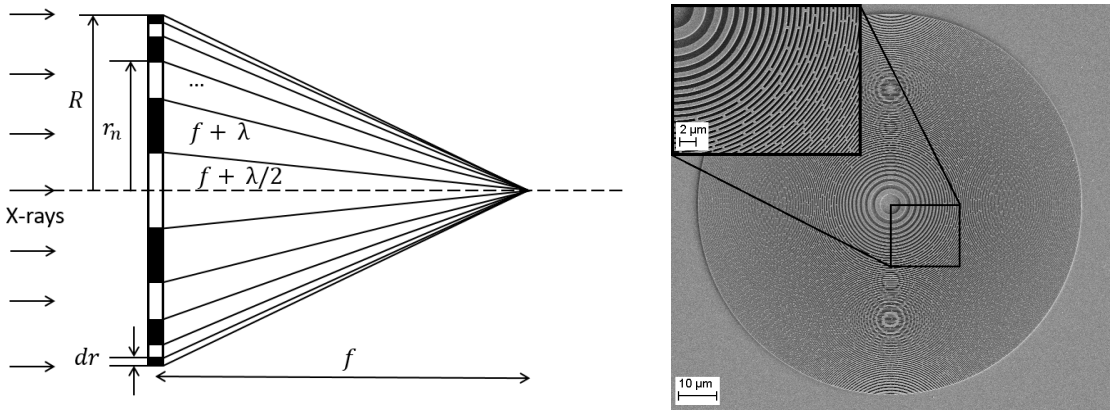

(a) Schematic of a zone plate **(b)** Real zone plate

Figure 2.1: (a) Focusing and geometry of a FZP. Adapted from [4]. (b) Scanning electron microscope (SEM) image of a FZP with 100 μm diameter and 50 nm outermost zone width. The inset shows a magnified view of the zones closest to the center.

2.1.2 Diffraction efficiency

The diffraction efficiency of a zone plate describes how large a fraction of the incoming photons is focused into a certain diffraction order. The strongest converging diffraction order is the first; this is the order which was measured in this thesis. A large part of the incoming light is diffracted into orders that only decrease the signal-to-noise ratio at the focal plane; the first-order diffraction efficiency is therefore an important figure of merit for describing the quality of the resulting image [16].

Figure 2.2 shows an illustration of the main diffraction orders present upon transmission of X-rays through a zone plate. An increased diffraction efficiency leads to shorter exposure times, which is crucial when dealing with problems such as thermal drifts, and consequently leads to a smaller radiation dose to samples [17]. Since the theoretical maximal resolution obtained with a zone plate relies on a high signal-to-noise ratio, a better diffraction efficiency indirectly improves the resolution as well.

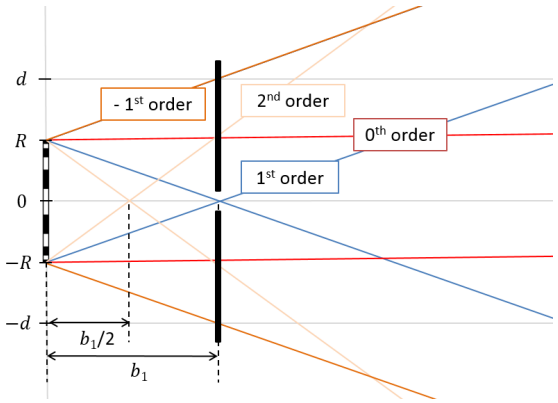

Figure 2.2: Schematic of the main diffraction orders present upon transmission of X-rays through a zone plate with diameter $d = 2R$. The zeroth order is the light which is transmitted through the zone plate without modulation. The first diffraction order is the one which is of interest in imaging applications; b_1 is the corresponding working distance. The second diffraction order has its focal plane at a distance equal to $b_1/2$. The black arrays symbolize a pinhole which blocks the unwanted diffraction orders.

The diffraction efficiency of a zone plate depends on the phase shift, attenuation and duty cycle produced by neighbouring zones and ideally reaches its maximum when the structure height introduces a phase shift of π [4]. One can derive the phase shift by looking at the transmission of X-rays, treated as electromagnetic waves, through an object described by a complex refractive index

$$n = 1 - \delta + i\beta, \tag{2.4}$$

and by further expressing a plane wave with amplitude E_0 and wave vector k travelling in the z direction in vacuum as

$$\Psi(z) = E_0 e^{ikz}, \tag{2.5}$$

which will change into

$$\Psi(z) = E_0 e^{inkz} = E_0 e^{i(1-\delta)kz} e^{-\beta kz} \tag{2.6}$$

upon transmission through a medium with refractive index n. Here, it becomes apparent that δkz is the phase shift during transmission a distance z through the medium and that $e^{-\beta kz}$ is an exponential decay factor attenuating the amplitude of the wave.

The derived relation for the phase shift can be used to determine the required structure height for a π-shift in a given material at a specified X-ray energy. Using energy-dependent values for δ found in [18], one can calculate that at 10 keV (one of the energies used at ANATOMIX) the required height for a π-shift in gold is 2.07 μm, in iridium 1.81 μm and in a light material such as aluminum as much as 11.34 μm, indicating the critical need for heavy metals when working with hard X-rays. Due to fabrication limitations such as collapsing, tilting and incomplete development of narrow structures, designs with widths less than about 100 nm which are higher than approximately a micrometer are difficult to achieve. The extreme aspect ratios are nevertheless needed in order to perform high-resolution, hard X-ray imaging with the zone plates. This is one of the main reasons as to why double-sided zone plates are fabricated in this project, since they give a way of doubling the aspect ratio using existing technology.

2.1.2.1 Diffraction efficiency of a transmission grating

In order to get a value for the maximum theoretical diffraction efficiency of a FZP, one can see it as a simple transmission grating with a thickness equal to the height of the zone plate structures. The diffraction efficiency η of a specific diffraction order m of a transmission grating (for $m \neq 0$) can then be expressed as

$$\eta = \left(\frac{\sin(Mm\pi)}{M\sin(m\pi)}\right)^2 \left(\frac{\sin((a/d)m\pi)}{m\pi}\right)^2 \left(1 + e^{-2kt\beta} - 2e^{-kt\beta}\cos kt\delta\right) \tag{2.7}$$

where M is the number of wires in the grating, a is the width of the grating opening, d is the grating spacing (a/d thus being the duty cycle of the grating), $k = 2\pi/\lambda = 2\pi \cdot E/hc$ is the photon wavenumber (with λ being the wavelength and E the photon energy), t the thickness of the grating, β the imaginary part of the refractive index and δ the decrement of the real part of the refractive index [19].

In the equation, the first factor corresponds to a normalized multiple-slit interference pattern which has maxima equal to 1 for integer values of m. Since the first order diffraction efficiency, $m = 1$, is what will be calculated here, this term will indeed be equal to 1 and is therefore from now on disregarded. The second term corresponds to a single-slit diffraction pattern from a slit with an opening of a/d, and the third term gives the interference between a wave coming through a slit opening and a wave going through a grating wire (with attenuation and phase shift as a consequence). The model from which the equation originates assumes that the grating wires have a rectangular cross-section. The expression is for the purposes of this thesis simplified as

$$\eta = \left(\frac{\sin(DC \cdot \pi)}{\pi}\right)^2 \cdot \left(1 + e^{-2kt\beta} - 2e^{-kt\beta}\cos kt\delta\right). \tag{2.8}$$

with the duty cycle DC defined as the ratio between the line width and the period.

Figure 2.3 describes how the first- order diffraction efficiency of a constant-duty cycle Ir zone plate varies with the structure height according to (2.8). It is clear that the harder the X-rays, the higher structures are required in order to focus the radiation efficiently.

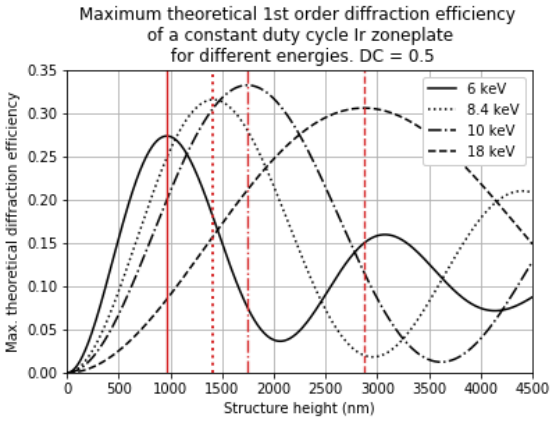

Figure 2.3: Maximum theoretical diffraction efficiency as a function of Ir zone plate structure height for energies which are relevant for the ANATOMIX beamline of Synchrotron SOLEIL. A constant-duty-cycle zone plate has been assumed. Red lines mark the structure heights which give the maximum efficiency.

2.1.3 Fabrication

FZPs are made using electron-beam lithography. As previously mentioned, a way of overcoming the aspect ratio limitations in the fabrication is to make double-sided FZPs [12], where zone plates are fabricated on two opposite sides of one membrane. The possible aspect ratio is in this way doubled.

An additional way of achieving both smaller line widths and higher aspect ratios is by a technique called line-doubling [20]. In this method, template structures are fabricated out of a low-atomic number material which has a very small effect on the transmission of X-rays. Subsequently, these structures are coated with a heavy metal by atomic layer deposition (ALD). The interaction with X-rays is then dominated by the metal deposited on the side walls on the template structures, which doubles the effective number of lines. The achievable line widths are due to this deposition method also not limited by the smallest achievable width of the template structures [21, 22]. Figure 2.4a shows the first step in fabricating such a double-sided, line-doubled zone plate and Figure 2.4b shows the finished structure.

Together, these two methods make it possible to fabricate FZPs with twice the aspect ratio compared to a what is possible for a standard single-sided FZP. However, one needs to reassure that the alignment between the two halves of the double-sided zone plates is within a fraction of the outermost zone width, since a larger misalignment strongly affects the diffraction efficiency. This is a strong motivation for the corresponding goal set in this thesis.

A previous study examined the optimal duty cycle for line-doubled zone plates made by ALD deposition of Ir on top of hydrogen silsesquioxane (HSQ) template structures, and showed that an HSQ duty cycle of 0.21 (0.22) and an Ir duty cycle of 0.33 (0.32) gives the highest performance, according to theoretical calculations (supporting experimental measurements) [22]. The work also took into account the dependency of the diffraction efficiency on the radius of the zone plate. Since the pitch of a zone plate changes with its radius and the thickness of the deposited Ir

layer does not, the duty cycle of Ir also changes with the radius. This is illustrated in Figure 2.4c. Taking this into consideration, it is of interest not only to be able to measure the absolute value of the diffraction efficiency, but also to be able to do it in a spatially resolved way. This motivates another goal of this thesis. The efficiencies shown in Figure 2.3 assume a constant duty cycle zone plate, which is not the case for the line-doubled structures fabricated in this thesis. Equation (2.8) will nevertheless be used in order to compare the theoretical efficiencies of different zone plates, even though these calculated values will never be reached.

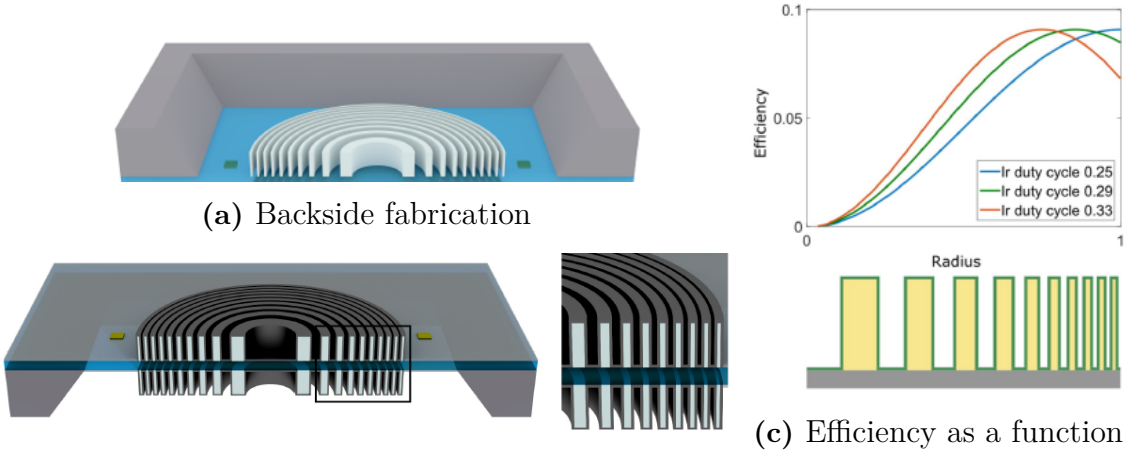

(a) Backside fabrication

(b) Finished structure

(c) Efficiency as a function of radius

Figure 2.4: (a) An illustration of the first step in the fabrication of a double-sided, line-doubled zone plate – the patterning on the backside of a membrane. (b) Schematic of a finished double-sided, line-doubled zone plate made on a silicon nitride membrane. Hydrogen silsesquioxane (HSQ, in light blue) is used as a template and Ir (in dark grey) is deposited on the template through ALD. Both images adapted from [12]. (c) Diffraction efficiency as a function of zone plate radius for a line-doubled zone plate for different Ir duty cycles. The diffraction efficiency goes to zero towards the center of the zone plate [23]. Image from [22].

2.1.4 Moiré fringes

Moiré fringes is a visual artifact originating from the interference in the overlay of ordered patterns. In the case of the image in Figure 2.1b the interference occurs between the pattern created by the zones of the zone plate and the regular pattern of the pixels in the SEM detector. The same type of pattern appears also as a result of overlaying two zone plates with each other, which is the case in the double-sided zone plates fabricated in this thesis.

For double-sided zone plates with an outermost zone width of 50 nm and a zone period of 100 nm, one dark and one bright Moiré fringe (one fringe period) will occur as soon as one zone plate is offset with 100 nm, i.e. one pitch, over the radius since the phase-shifting and the transparent zones will be shifted in a way where they are destructively interfering at some positions along the zone plate diameter and constructively at others. Moiré fringes can therefore be used as important indicators of misalignment between the two halves of a double-sided zone plate.

Figure 2.5 shows how different Moiré interference patterns can be simulated by the overlay of two simple zone plate sketches. Figures 2.5b and 2.5c show examples of linear offsets in different directions. In Figure 2.5d, one of the zone plates is not offset but simply smaller compared to the other – showing that well-aligned and concentric zone plates of different sizes also give rise to Moiré fringes. Since the offset between the zones is concentric, the resulting fringes are circular. In the same way, curved fringes are visible in Figure 2.5e, where one zone plate is not only scaled with respect to the other but also offset.

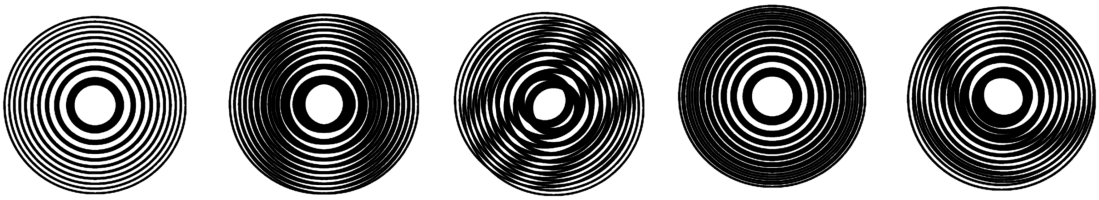

(a) A single zone plate | **(b)** Horizontal offset of $2dr$ | **(c)** Diagonal offset of $4dr$ | **(d)** ZPs of different size | **(e)** Different size and diagonal offset

Figure 2.5: Illustration of how Moiré fringes appear, made in (b)-(e) by overlaying two zone plates such as the one in (a).

2.2 X-rays – production and characteristics

There exist many kinds of X-ray sources, all of which are characterized by their brightness – also known as brilliance. The concept connects their photon flux, beam size, beam divergence and bandwidth,

$$\text{brilliance} = \frac{\text{photons/second}}{(\text{mrad})^2 \cdot (\text{mm}^2 \text{ source area}) \cdot (0.1\% \text{ bandwidth})}, \tag{2.9}$$

meaning that the unit translates into photon flux per unit source area and unit solid angle. Lab-based sources such as X-ray tubes produce both the least brilliant and the least coherent light compared to other types of X-ray source classes such as synchrotrons and free-electron lasers [3, 24], but present strong advantages in terms of operation and cost. Both X-ray tubes and synchrotrons will be introduced further in the following sections.

2.2.1 Synchrotrons

Synchrotrons belong to the most brilliant sources of X-rays, with extremely intense, parallel, monochromatic and narrow beams of X-rays. The brilliance produced is many orders of magnitude higher than the one from lab-based sources.

A schematic of a synchrotron and its main components is shown in Figure 2.6a. Simply explained, a synchrotron consists of a storage ring (typically, some hundreds of meters in circumference – Synchrotron SOLEIL has a circumference of 354 m) – and beamlines emerging tangentially from it. In the storage ring, high-energy

electrons circulate at highly relativistic velocities; due to the nature of their motion, synchrotron light is emitted which is then utilized in the beamlines.

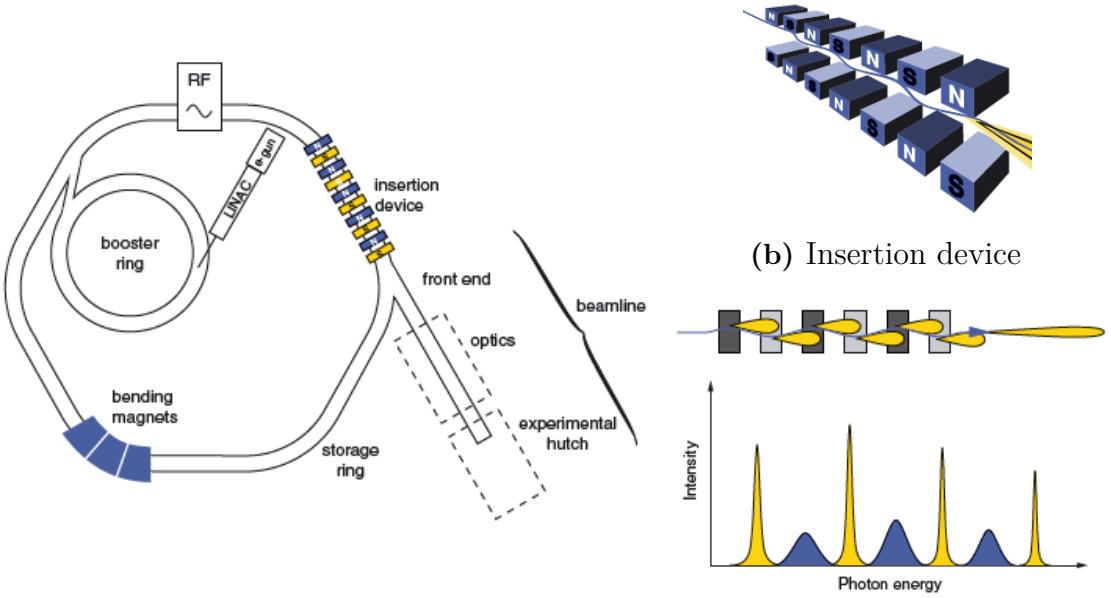

(a) Synchrotron **(b)** Insertion device **(c)** Undulator and its harmonics

Figure 2.6: (a) A schematic of a synchrotron and its main components. (b) Simplified sketch of an insertion device with its array of magnets creating magnetic fields in alternating directions. (c) Illustration of an undulator and the overlapping radiation lobes from the electrons performing a "slalom" motion, and the resulting energy spectrum with even (blue) and odd (yellow) harmonics [3].

The electrons, coming from e.g. a heated filament in an electron gun, are accelerated in a linear accelerator (linac in Figure 2.6a) to about 100 MeV before they are injected into the so-called booster ring where they are further accelerated, usually to the energy of the electrons in the storage ring. The storage ring electron energy is about a few GeV – at Synchrotron SOLEIL, it is 2.75 GeV. The electrons from the booster ring are regularly injected into the storage ring so that its current is maintained approximately constant. In the storage ring, there are arrays of magnets which keep the electrons on a closed path. The ring consists both of straight and bent sections; in the bent sections, bending magnets curve the path of the electrons, and the straight sections are used for so-called insertion devices which generate most of the radiation used in the beamlines. Due to the emission of synchrotron radiation, the electrons in the storage ring lose energy. This energy is replenished by a radio frequency (RF) supply, providing the necessary energy to the electrons as they pass through it and preventing the electrons from losing their circular path.

Insertion devices work by forcing the electrons in the storage ring to perform an oscillatory path in the plane of the ring, and consist of arrays of magnets with magnetic fields in alternating directions – see Figure 2.6b. There are two types of insertion devices, wigglers and undulators, distinguished by the degree to which they force the electrons to deviate from their straight path, with the latter type referring to a smaller deviation. The insertion device used at the ANATOMIX beamline

is an undulator. There, the radiation cones from electrons performing a "slalom" motion in the device overlap and interfere with each other. The field amplitudes are added vectorially, taking the phase difference in account, and the sum is squared in order to get the intensity of the radiation. The result is peaks at certain energies where the interference between the radiation cones is constructive, giving so-called undulator *harmonics*. The spectrum of an undulator in other words consists of regularly separated narrow bands of radiation, as illustrated in Figure 2.6c. Specific harmonics can be isolated by using a monochromator, typically put into the optics hutch of the beamline. A beamline also contains a front end and an experimental hutch – the former, among other things, isolates the beamline vacuum from the storage ring vacuum, blocks the radiation when the optics- or experimental hutch has to be accessed, and can filter out the low-energy tail of the radiation spectrum which can damage optical components. In the optics hutch the beam is focused and monochromatized, and the actual experiments employing the synchrotron radiation are performed in the experimental hutch. For beamlines such as the ANATOMIX beamline, the hutches are shielded with lead-lined concrete walls in order to protect users from both X-rays, gamma rays and high-energy neutrons produced in the storage rings [3].

2.2.2 X-ray tubes

An X-ray tube, simply described, consists of an anode, a cathode and a high-voltage source. A low-voltage current, known as the filament current, is sent through a filament in the cathode, causing thermionic emission of electrons. These electrons are subsequently accelerated towards the anode by the high potential difference provided by the source, resulting in a so-called tube current. Interaction between the electrons with the target then produces X-rays which are directed into a beam using collimators. Only a small fraction of the kinetic energy of the electrons is converted into X-rays; most of it dissipates as heat.

Out of the X-rays that are produced, the most are so-called bremsstrahlung radiation. Bremsstrahlung is produced when electrons pass nuclei of the target material, subsequently change their paths and therefore give up energy in the form of X-rays. The closer to the nuclei, the higher the energy of the X-rays produced, meaning that the highest X-ray energies are produced from electrons colliding directly with nuclei, giving away all of their kinetic energy. This maximum energy is given by the maximum acceleration the source can provide and is set by the user. So is the filament current, which effectively determines the tube current by giving the number of electrons emitted from the cathode and thus the number of electrons that are accelerated towards the anode.

The rest of the X-rays that are produced are known as characteristic X-rays. These appear when the energy of the accelerated electrons is high enough to eject inner shell electrons in the target material. An outer shell electron subsequently fills the vacancy and an X-ray is emitted which has an energy equal to the difference in the discrete orbital binding energies. See Figures 2.7a and 2.7b, which show the X-ray spectrum of tungsten and the electron transitions corresponding to characteristic X-rays. The name characteristic comes from the fact that these energy differences

are characteristic of the atomic number of the target. The characteristic X-rays give peaks at discrete energy values in the otherwise continuous X-ray spectrum given by the bremsstrahlung. Table 2.1 presents the exact energy values for the characteristic lines of tungsten. In a general X-ray tube up to 20% of the radiation can consist of characteristic X-rays, with the rest being given by bremsstrahlung.

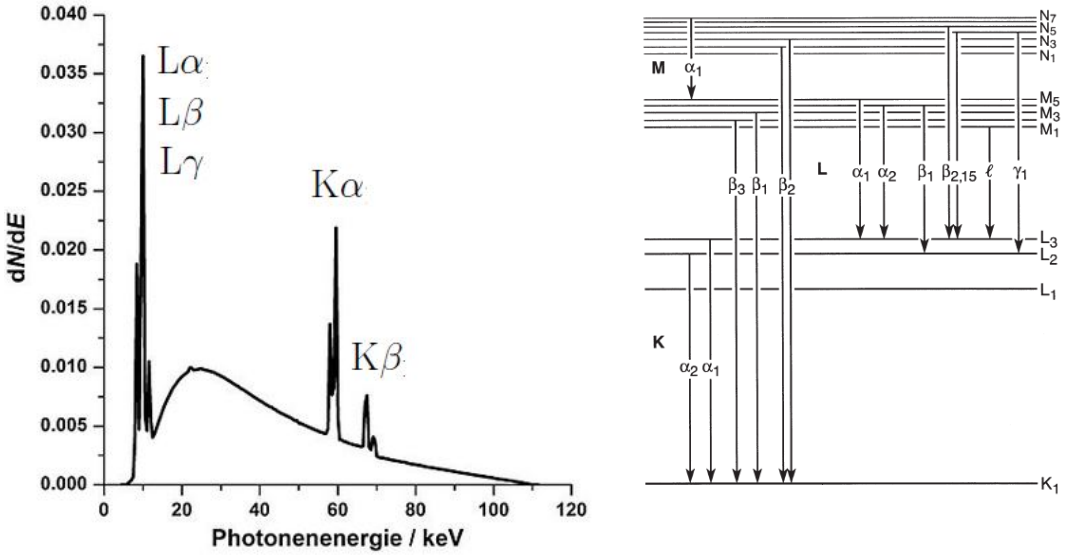

(a) Tungsten spectrum **(b)** Transitions and emission lines

Figure 2.7: (a) X-ray energy spectrum of an X-ray tube with a tungsten anode operated at 110 kV, showing X-ray intensity as a function of energy. The continuous spectrum is given by bremsstrahlung and the peaks correspond to characteristic X-rays. Adapted from [25]. (b) Transitions between the shells in an atom, giving characteristic emission lines in the X-ray spectrum [26].

Line	$L\alpha_1$	$L\alpha_2$	$L\beta_1$	$L\beta_2$	$L\gamma_1$	$M\alpha_1$
Energy (keV)	8.398	8.335	9.672	9.962	11.286	1.775
Relative intensity (%)	100	11	67	21	13	100

(a) L and M emission lines

Line	$K\alpha_1$	$K\alpha_2$	$K\beta_1$	$K\beta_2$	$K\beta_3$
Energy (keV)	59.318	57.982	67.244	69.067	66.951
Relative intensity (%)	100	58	22	8	11

(b) K emission lines

Table 2.1: Tungsten emission lines, with corresponding energies and relative intensities [26].

Another important characteristic of an X-ray tube is the effective size of the focal spot, since it determines the achievable spatial resolution in imaging. The effective focal spot size is determined by the actual spot size, in turn given by the electron beam and target design [27]. For high-resolution imaging so-called microfocus

X-ray tubes are used, with focal spot sizes typically in the order of a few or tens of micrometers.

The X-ray tube used in this project, a Hamamatsu L10101 Microfocus X-ray tube [28], has a tungsten target with a spectrum as the one shown in Figure 2.7a. The focal spot size can be tuned between 5-30 μm and the tube can be operated at tube voltages between 40 and 100 kV and tube currents between 10 and 200 μA.

2.2.3 Radiation safety

X-rays are known to increase the risk of cancer and are classed as carcinogens by the World Health Organization's Agency for Research on Cancer [29]. Their biological effects are classified as either deterministic or stochastic, with the former appearing as for example skin injuries and hair loss and the latter being the induction of cancer. Deterministic effects occur at a certain threshold dose and can be reliably predicted; stochastic effects occur with a probability that increases with dose. For deterministic effects, the threshold dose can be between 2-5 Gy[1] for effects such as hair loss and sterility and up to 20-40 Gy for irreversible skin damages. It is believed that the stochastic effects, which occur randomly and have a long latent period, do not have a radiation dose threshold and are cumulative, meaning that more and longer exposures increase the risk. The stochastic effects depend on the type of irradiation, on the tissue being irradiated and the age and sex of the person – studies have shown that the younger the person, the higher the risk, and that women have about twice the risk compared to men exposed to the same dose [31].

Most studies presenting radiation damage of patients do so with regards to medical examinations using techniques such as computed tomography (CT). In such cases, the tube voltage and current can be adjusted depending on the part of the patient that is being scanned, and radiation damage is there very relevant due to the direct exposure of the tissue of the patient. In this thesis, the X-ray tube parameters will not be changed, and direct exposure to radiation will be avoided due to a range of precautionary measures.

One of the main safety measures is an excessive lead shielding around the X-ray tube – the whole setup is enclosed in a hutch to which the door needs to be closed in order for X-ray emission to begin. If the door is opened during emission, there are two independent built-in interlock circuits in the X-ray tube which independently from each other can turn off the power to the high voltage section and stop the tube from emitting X-rays. There is also a built-in overload protection circuit which detects an excessive X-ray tube voltage and current [28]. In addition, other security measures are taken: to prevent accidental exposure to X-rays in case of failure of the interlock circuits, the emission of X-rays is always turned off using the X-ray tube control software before opening the door of the hutch.

[1] 1 Gy (1 Gray) is an SI unit of absorbed dose and is defined as the absorption of one joule of energy in the form of ionizing radiation per kilogram of matter [30].

2.3 Transmission X-ray Microscopy

A full-field imaging X-ray microscope, or a transmission X-ray microscope (TXM), can be seen as the X-ray equivalent of a visible light transmission microscope. TXMs are well suited for high-resolution morphological studies, studies of dynamic events and microtomography. A typical TXM setup consists of a condenser optical element, an objective lens (usually a FZP), in some cases phase rings, and a pixel detector [2], see Figure 2.8a. The condenser illuminates the sample, and the objective lens generates a magnified image of the sample onto the detector. One can additionally have an order-sorting aperture downstream[2] from and a central stop up- or downstream from the condenser, in order to prevent zeroth order radiation from the condenser from reaching the sample, and to prevent first order radiation from the condenser from reaching the detector through the zeroth order of the objective lens [32]. Removing the contribution of the zeroth order of the condenser is crucial, especially for hard X-rays, since it is much higher than the signal from the zone plate. If the specimen is rotated around an axis perpendicular to the optical path, tomographic imaging can be done, giving three-dimensional, highly resolved information on the sample. Figure 2.8b shows a slice through such a tomography made at the ANATOMIX beamline of Synchrotron SOLEIL.

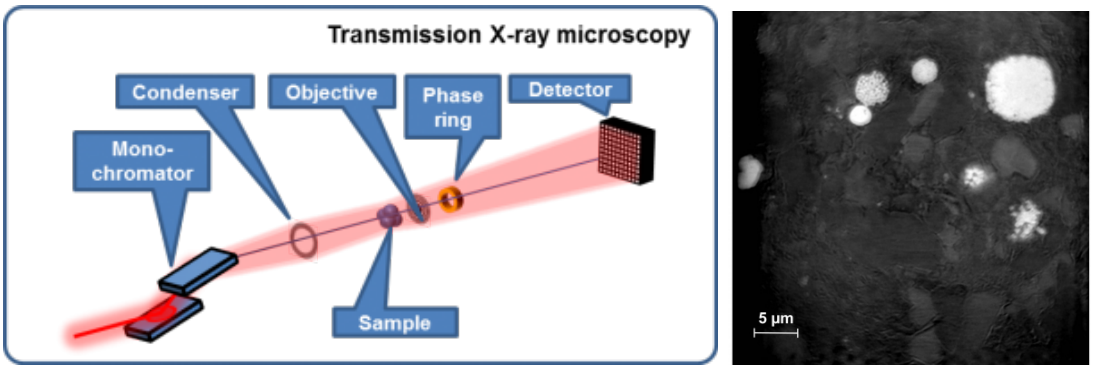

(a) TXM setup **(b)** TXM image

Figure 2.8: (a) Schematic of a typical setup used for TXM. (b) Sagittal (longitudinal) slice of a local tomography on a shale-rock sample with pyrite inclusions (light gray), made at the ANATOMIX beamline of Synchrotron SOLEIL. Both images from [7].

At ANATOMIX, two imaging modes - absorption contrast and Zernike phase contrast [33, 34, 35] - will be employed, with resolutions down to 100 nm [7]. Zernike phase contrast is a technique for visualizing samples which are weakly absorbing, for example biological samples which mainly consist of low-Z (low-atomic-number) elements which are almost transparent to X-rays. The technique is based on the interference contrast that occurs upon phase-shifting the focused, unscattered photons by $\pi/2$ with respect to the photons scattered by the sample [2, 36]. The phase-shifting is performed by phase rings placed in the back focal plane of the objective zone plate.

[2]The source point is seen as the origin of the stream; putting something downstream therefore means putting it further away from the source, and putting it upstream means putting it closer to the source.

3
Methods

This chapter describes the FZP fabrication, the design of the X-ray-tube-based setup, the simulation and measurement of the X-ray tube spectrum, the zone plate efficiency determination, and the measurement of misalignment in double-sided zone plates.

3.1 Fresnel zone plate fabrication

Double-sided, line-doubled fabrication consists of two subsequent, very similar fabrication schemes: first, single-sided zone plates are fabricated on the backside of a Si_3N_4 (silicon nitride) membrane as it is illustrated in Figure 2.4a and are subsequently covered with Ir. Then, the chip is turned around and the fabrication process is repeated on the frontside of the membrane. The only difference in the processing of the frontside is the extra alignment step which is needed in order to align the frontside structure to the backside zone plate. The finished double-sided zone plate looks like the one in Figure 2.4b. The design parameters used in this thesis, suitable for the intended application at the ANATOMIX beamline, were a zone plate diameter of 100 μm, an outermost zone width of 50 nm, and HSQ and Ir duty cycles as the optimal values found by Marschall *et al* [22], see Section 2.1.3. Membranes either 3 $\times$ 3 mm and 4.8 $\times$ 4.8 mm in size were used.

The zone plate fabrication on one side can be described as follows: the membrane is first argon ion milled and then etched using oxygen plasma in order to increase the adhesion for the subsequently deposited resist. The resist, undiluted HSQ FOx-16, is spin coated at 1 000 rpm during 60 seconds; the low angular rotation speed is used in order to obtain as thick a layer as possible. At this speed the thickness of the deposited layer varies substantially over the membrane. Patterning is performed using a Raith EBPG 5000+ electron beam system with an acceleration voltage of 100 kV, beam current of 4 nA and dose of 15 000 μC/cm^2. Around each zone plate, a set of four alignment markers is patterned, which is used for the frontside alignment step. The structures are developed using the developer AZ A351 in a 1:3 mixture with water during 15 minutes. For so-called hot development the dose is increased to 27 000 μC/cm^2, the beam current decreased to 2.5 nA, and the development is done during 90 seconds in the same developer solution but heated to 50 °C. After the development, a critical point drying step in an Automated Critical Point Dryer Leica EM CPD300 is performed in order to prevent capillary forces from making the most narrow structures collapse. Finally, Ir is deposited on top of the resist structures by plasma-enhanced atomic layer deposition in a Picosun R200 ALD tool. 1290 cycles are done, giving an Ir thickness of approximately 55 nm. One cycle consists of three

pulses with 0.8 s of the precursor iridium acetylacetonate (Ir(acac)3) and one pulse with 3 s of the reactant oxygen plasma (with inductively coupled plasma power of 2000 W and a gas flow of 50 sccm). The deposition is done at a temperature of 370 °C. The mentioned processes are repeated for the frontside, but as mentioned there is an additional alignment step in the electron beam patterning.

The fabricated zone plates were imaged in a Zeiss Supra VP-55 scanning electron microscope (SEM) in order to control the structure quality, measure the HSQ- and Ir duty cycles and determine the structure heights. The HSQ template structures were imaged using an acceleration voltage of 3 keV and the Ir-coated structures using a voltage of 10 keV. For all images an aperture of 7.5 μm was used.

A zone plate patterned in HSQ on the backside of a membrane is shown in Figure 3.1, where 3.1a shows an overview with the four alignment markers, 3.1b a closer view of the zone plate and 3.1c an enlarged image of the outermost zones where a duty cycle measurement can be made. The apparent width of the structures depends a lot on the image acquisition parameters of the SEM; the measurement is therefore seen as approximate. The same three cases for an Ir-coated zone plate are shown in Figure 3.2.

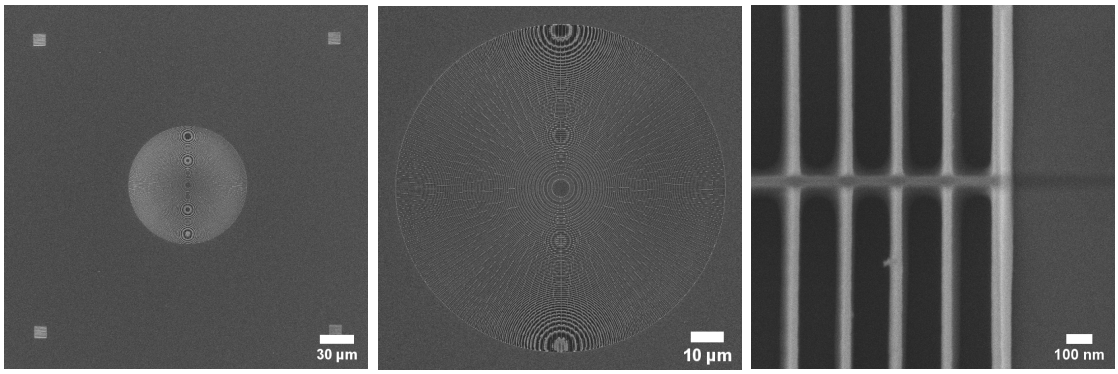

(a) Zone plate in HSQ with markers **(b)** Zone plate in HSQ **(c)** Outermost zones in HSQ

Figure 3.1: An HSQ zone plate patterned on the backside of a Si_3N_4 membrane.

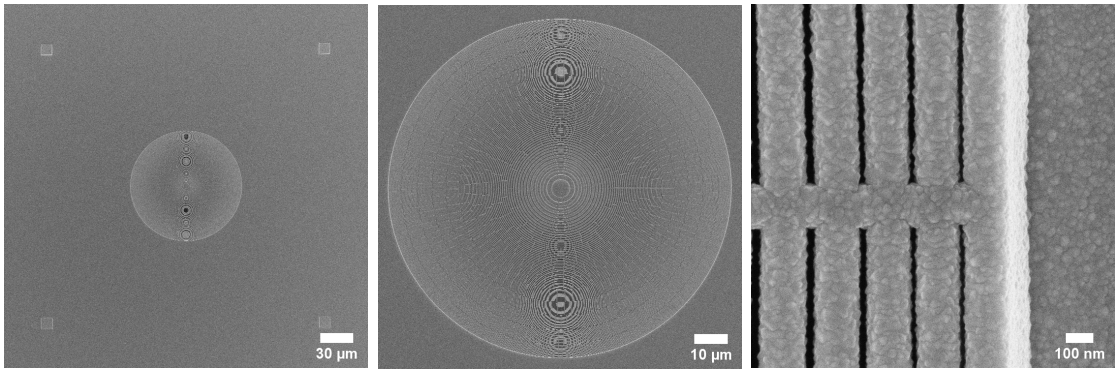

(a) Ir-coated zone plate with markers **(b)** Ir-coated zone plate **(c)** Ir-coated outermost zones

Figure 3.2: An Ir-covered zone plate on the backside of a Si_3N_4 membrane.

Figure 3.3a shows the same type of zone plate but patterned on the frontside. The three cross-like symbols around the zone plate show the marker search performed by the electron beam system during the alignment to the backside zone plate. Figure 3.3b and 3.3c show a zone plate imaged under a 45° tilt angle, where the structure height can be measured. The actual heights are obtained after compensating for this angle.

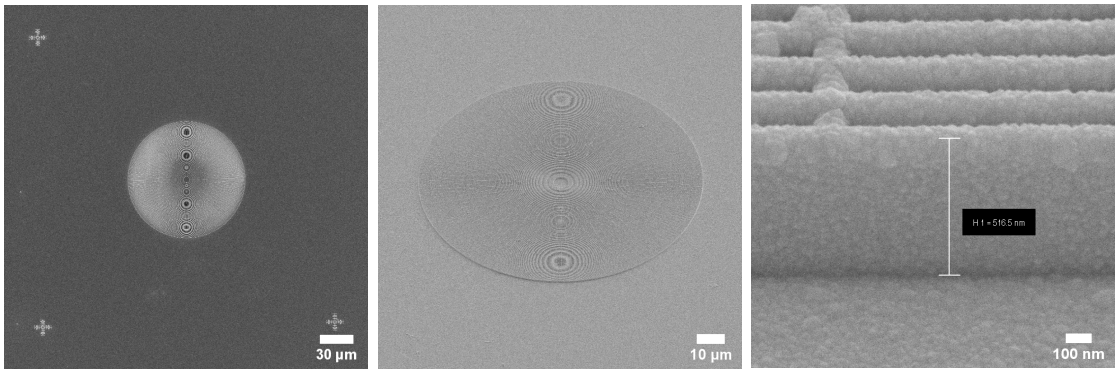

(a) Zone plate in HSQ after frontside patterning

(b) Ir-coated zone plate, tilted view

(c) Height measurement on Ir-coated zone plate in tilted view

Figure 3.3: (a) A frontside zone plate made in HSQ. The cross-like features indicate the marker search done by the electron beam lithography system. (b) A zone plate under 45° tilt angle. (c) A closer look at the zone plate in (b) where the structure height is measured.

3.2 Design and construction of X-ray-tube-based setup

This section motivates the design choices that were made for the X-ray-tube setup and presents the alignment of its components.

3.2.1 Previous X-ray-tube-based setup

An initial setup, built by members of the *X-ray Optics and Applications* group, could measure the relative diffraction efficiency of single- and double-sided zone plates and thus relied on absolute measurements performed for calibration at a synchrotron. The setup consisted of a copper anode X-ray tube, a motorized stage which could move the zone plate chip to be measured in a plane perpendicular to the optical axis, and a PCO pco.edge 4.2 CMOS camera [37] coupled to a scintillator screen detecting the diffracted light. The PCO camera was placed at a distance equal to the working distance of the zone plate, meaning that the first diffraction order of the zone plate was focused onto it. See Figure 3.4a for a schematic of this setup.

Since the PCO camera was put into the focal plane of the zone plate, the resulting images showed a projection of the source spot and gave no information about how well different parts of the zone plate were performing. Due to the large losses associated

with the scintillation step, moving the camera further downstream was not possible. Another issue was that the light from the X-ray tube was filtered only by a nickel (Ni) filter, meaning that a wide range of energies was reaching the camera and making it impossible to give absolute values for the diffraction efficiency. In order to get absolute values, at least one zone plate out of a set with identical dimensions needed to be measured at a synchrotron using a known energy. Without such a reference measurement, one could only compare zone plates with each other and not give an absolute value for their efficiencies.

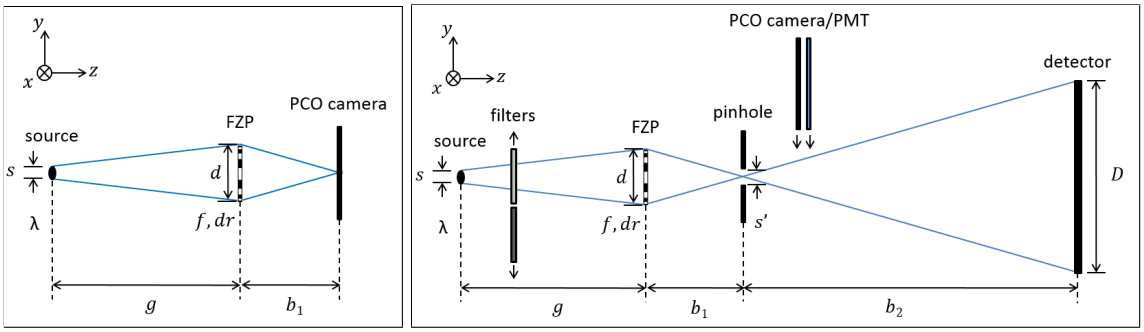

(a) Schematic of old setup **(b)** Schematic of new setup

Figure 3.4: (a) Schematic of the old setup. The source-to-zone-plate distance g, focal length f, working distance b_1, source size s, X-ray wavelength λ, zone plate diameter d and outermost zone width dr is indicated. (b) Schematic of the new setup. Filters, a pinhole and a photomultiplier tube (PMT) have been added. In addition to the variables in (a), the pinhole-to-detector distance b_2, pinhole size s', pinhole exit angle α and size of image D on the detector is indicated. The arrows next to the filters, PCO and PMT do not correspond to the chosen axes but are just illustrating that the mentioned components can be easily moved in and out of the beam.

3.2.2 New X-ray-tube-based setup

In the new setup, a Hamamatsu L10101 microfocus tungsten anode tube was used. A pinhole was placed at the zone plate focus position and the PCO camera was moved back to a distance approximately two working distances away from the pinhole, to be used only for alignment purposes. For the purpose of alignment, but mainly for the diffraction efficiency measurements, a Hamamatsu Photon Counting Head 10682-210 [38] (from now on called PMT) coupled with a scintillator was included on the same motorized stage as the PCO, making it possible to easily switch between the two. A MÖNCH03 detector [39] – from now on called just the Mönch – was put further downstream from the source and was used for the imaging. The new setup is illustrated in Figure 3.4b.

The Mönch detector is a direct-conversion, hybrid Si pixel detector which removes the need for an intermediate scintillation step and visible light optics, utilizing more of the diffracted photons and making it possible to put the detector further away from the source. Due to the high absorption of photons in air, an effective detection of photons is crucial. Figure 3.5 shows the drastic decrease in transmission for hard X-ray photons of energies up to about 12 keV for different air paths. Another

advantage of the Mönch is that it has a readout noise which is close to zero, giving a much lower noise on weak signals compared to the PCO camera.

As illustrated in Figure 3.4b, putting the detector away from the focal plane of the zone plate enables spatial mapping of the diffraction efficiency of the FZP, since an enlarged image of the diffraction pattern hits the detector. The distance to the source, approximately 1.3 m, was chosen as a compromise between having more photons impinging on the detector (enabling shorter acquisition times) and obtaining larger zone plate images. A feature of the Mönch which gives even better spatial resolution is that it possesses pixels with a charge-sharing ability – the center of impact of a photon can be determined with sub-pixel resolution by looking at the charge distribution between pixels, and the pixel size can be interpolated from the initial value of 25 μm down to 1 μm [40]. This feature was not used in this thesis, since the initial spatial resolution was sufficient for all intended purposes.

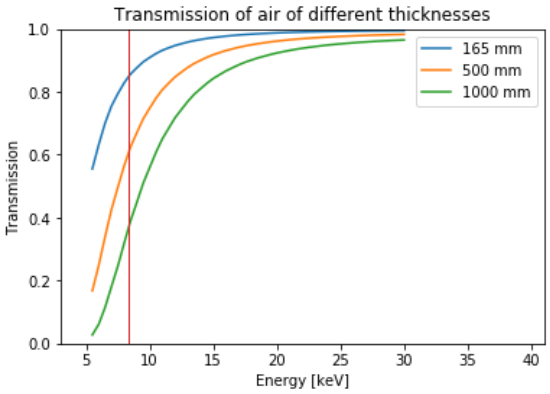

Figure 3.5: The transmission of air as a function of energy for different path lengths. The red line marks the main L_α emission line of tungsten. The transmission decreases to as low as 40% when moving 1 000 mm away from the source.

3.2.2.1 Choice of pinhole

In order to be able to obtain an enlarged image of the zone plate on the detector, and in order to measure the first-order diffraction efficiency, a pinhole is needed in the first order focal plane of the zone plate. This prevents unwanted diffraction orders from reaching the detector and enables truthful imaging and efficiency calculations. As seen in Figure 2.2, the zeroth diffraction order still passes through the pinhole and will appear as a bright spot in the center of the eventual image that is acquired. In order to lose as little information as possible in this image, the pinhole therefore needs to be rather small. In addition, the higher the ratio of the zone plate diameter to the pinhole diameter, the better the signal-to-noise ratio in the measurements. On the other hand, it is crucial that the pinhole is larger than the projection of the source spot made by the zone plate, which is in the order of a few micrometers – otherwise flux and information is lost. A larger pinhole is also easier to align.

As a compromise between these factors, a 10 μm pinhole was chosen in this thesis. Other pinhole sizes – 5 μm, 20 μm, 30 μm, and 50 μm – were mounted at the same holder to allow for quick changes when needed for other possible zone plate characteristics, and the effect of these pinholes on the X-ray tube spectrum was

simulated. A 100 μm pinhole, which has no order-sorting capabilities for a zone plate of the same diameter, was included for measurements of the intensity impinging on the zone plate and mounted on the same holder as the zone plates. Since its diameter matched the zone plates measured in this thesis and since the distance to the source was the same, it could be directly used to record the incoming flux.

3.2.2.2 Alignment of components

The X-ray tube was positioned already at the start of the thesis; all other components were aligned to the height of its beam using an alignment laser. The optical axis was defined by the X-ray source point and the center of the field of view of the PCO camera; the axes of translation x, y and z were defined as indicated in Figures 3.4.

In order to simplify the movement of components, some of their axes of movement were motorized using stepper motors from Kohzu, Newport and Owis. All of them were implemented and controlled in the UNIX-based X-ray diffraction software *spec* [41], where scripts for automated scans and component movements were written. The source and detector were fixed once mounted; the filters, PCO and PMT were motorized in x in order to be easily moved in and out of the beam; the pinhole holder was motorized in x and y in order to be able to choose different pinholes, and the zone plate holder was motorized in x, y, z in order to position the samples along and transverse to the optical axis, and additionally around the rotational axes $rotx$ and $roty$ (defined as rotation around x and y, respectively) in order to be able to tilt the zone plates. For proper use of the rotation functionality, it had to be guaranteed that the zone plates were positioned in the rotation center of both rotation stages, which was why an additional manual z stage was added on top of the rotation stages. The alignment of a zone plate into the center of rotation was made only once by using a mesh mounted on the same holder and recording the movement of a central feature on the mesh as a function of rotation angle for both stages. This was repeated at several distances along the optical axis, defined by the manual z stage, and the obtained values were interpolated to find the position of zero movement, corresponding to the rotation centre of both stages.

The PMT was used for alignment of the zone plates and pinholes. The process of aligning a zone plate and pinhole *transverse to* the optical axis before a measurement was defined as follows:

1. Find the wanted ZP using the PCO camera
2. Move the wanted pinhole to the same spot in the field of view
3. Move the PCO camera out of the beam and move in the PMT
4. Scan the ZP in x, and move it to the position which gives the maximum number of counts on the PMT
5. Scan the ZP in y, and move it to the position which gives the maximum number of counts on the PMT

This method, with a preliminary alignment using the PCO camera and a subsequent precise alignment using the PMT, was used for all zone plate measurements. The subsequent measurement of the absolute diffraction efficiency is described in Section 3.4.2. In order to find the optimal relative position of the source, zone plate and pinhole *along* the optical axis, the same type of scan was made but at different

positions of the zone plate stage along the optical axis, with the pinhole and source positions being fixed. The position with the maximum number of photon counts was then used for the diffraction efficiency measurements.

3.2.2.3 Choice of filters

In this thesis, the peaks of interest in the spectrum of the tungsten source were the $L_{\alpha 1,2}$ peaks. These peaks have an energy of 8.335 and 8.398 keV, see Table 2.1a, and are almost never distinguishable from each other. In order to make absolute measurements of the zone plate diffraction efficiency, a narrow-band tube spectrum is needed, meaning that these peaks need to be isolated from the rest of the spectrum.

One can suppress photons of certain energies by using a filter of a material which has its absorption edge (electron binding energy) at a suitable energy. By using a set of two filters, one can isolate an energy range from two sides in a spectrum. The monochromatization is then made differentially – each measurement is made once with each filter and the results are subtracted, giving the photon counts of energies only from the narrow "transmission window" between the filters' absorption edges. Chen *et al* [42] filtered out the $L_{\alpha 1,2}$ peaks of tungsten by using a cobalt (Co) and a copper (Cu) filter, with absorption edges at 7.709 keV and 8.979 keV, respectively [26]. Here, in order to monochromatize the spectrum even better, a Ni and a Cu filter was used instead – Ni has its absorption edge at 8.333 keV, yielding almost half the bandwidth of 0.646 keV of Chen *et al* and still including the peak of interest.

Figure 3.6 illustrates how the wanted L_α tungsten peaks fit into the transmission window between the absorption edges of the two filter materials. Different filter thicknesses and their effect on the spectrum were simulated but the set of 12.00 μm Cu and 12.85 μm Ni was used for the diffraction efficiency measurements. Figure 3.6b motivates the slightly different filter thicknesses – by adjusting the Ni thickness to 12.85 μm and therefore matching the filter transmissions outside of the wanted energy window, the contribution of photons of unwanted energies is minimized.

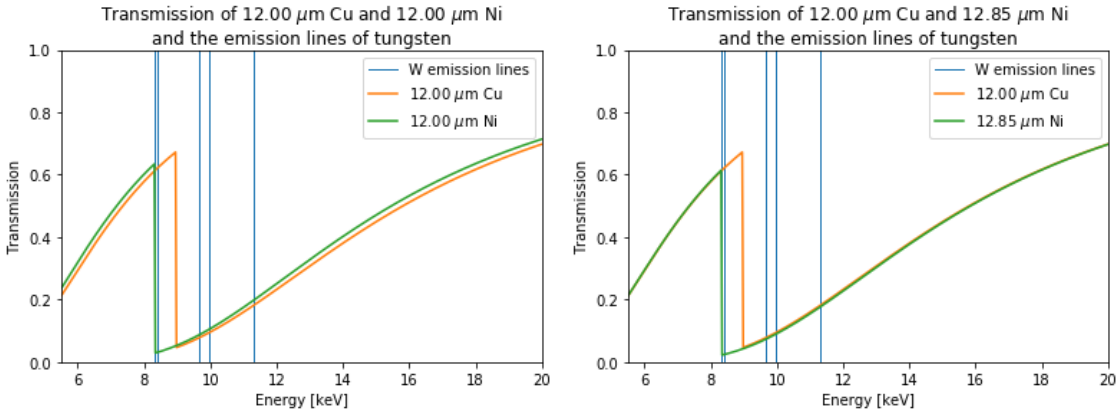

(a) 12.00 μm Cu and 12.00 μm Ni **(b)** 12.00 μm Cu and 12.85 μm Ni

Figure 3.6: A comparison between the transmission of Cu and Ni for two different Ni thicknesses, together with the emission lines of tungsten. Adjusting the thickness of the Ni filter to 12.85 μm as in (b) gives a clear match in the transmissions.

A simulation of the result from a differential measurement of the tungsten spectrum with the two filters is illustrated in Figure 3.7, where a clear isolation of the wanted peak can be seen.

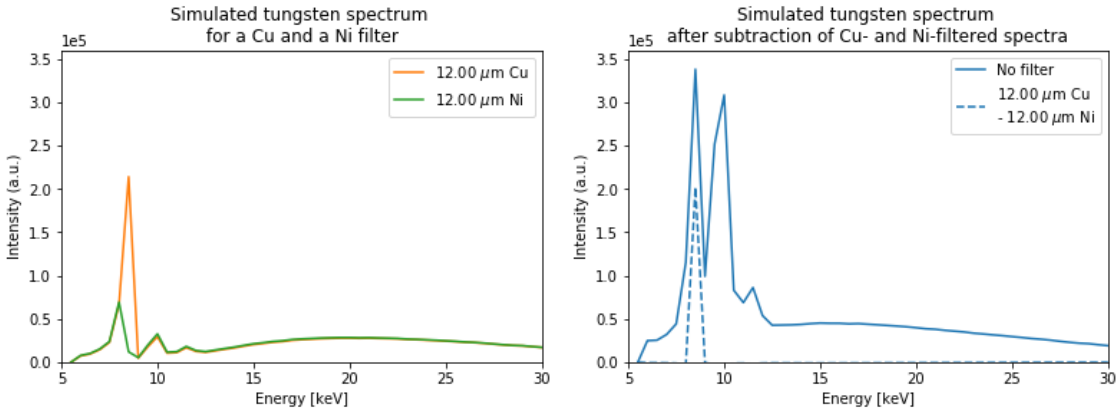

(a) Cu- and Ni-filtered tungsten spectrum

(b) Result after subtracting the two spectra

Figure 3.7: A simulation of the effect of the chosen filters on the tungsten spectrum. (a) shows the spectra resulting from filtering the tungsten spectrum with the different filters and (b) shows the result after subtracting the Ni-filtered spectrum from the Cu-filtered spectrum (dashed), compared to the initial tungsten spectrum (solid). The L_α peak is clearly isolated.

3.3 Simulation and measurement of X-ray tube spectrum

The X-ray tube spectrum was simulated for different filters and distances from the source using emission data for tungsten from a web-based software from Siemens Healthcare [43] and transmission data for air, Cu and Ni from The Center for X-Ray Optics (CXRO) [18]. The simulations were written in Python. Since an X-ray tube acceleration voltage of 40 kV was used in the diffraction efficiency measurements, providing X-ray photons with energies up to 40 keV, the spectra of interest were up to 40 kV. However, due to CXRO providing data only up to a photon energy of 30 keV, the simulations were performed only up to this energy. Air data for atmospheric pressure and 22 °C were used. The measurements of the actual X-ray tube spectra were made using an X-123CdTe X-ray spectrometer from Amptek [44] at 40 kV tube voltage and 150 μA and 10 μA tube current, with the latter used at closer distances to the source due to saturation issues. For the energy calibration of the acquired spectra, done using the DPPMCA Display & Acquisition Software [45], the current was further decreased to 5 μA. All of the spectra were measured without a pinhole.

In addition to the mentioned simulations, the effect of pinholes of different sizes on the X-ray tube spectrum was simulated. It was assumed that the pinhole frames have zero transmission for all X-ray energies, meaning that the pinholes can cut off a beam completely. For a finite pinhole size, there is a range of energies where the ”cone” of X-rays focused by the zone plate is completely transmitted. Correspondingly,

as seen in Figure 3.8a, contributions of "cones" of off-focus energies will be cut by the pinhole, reducing the contributing area of the zone plate. This results in a band-pass function which relies on the dependency of the efficiency of a line-doubled zone plate on its radius. Figure 3.8b shows the efficiency profile that was assumed in this case, differing slightly from the real profile shown in Figure 2.4c.

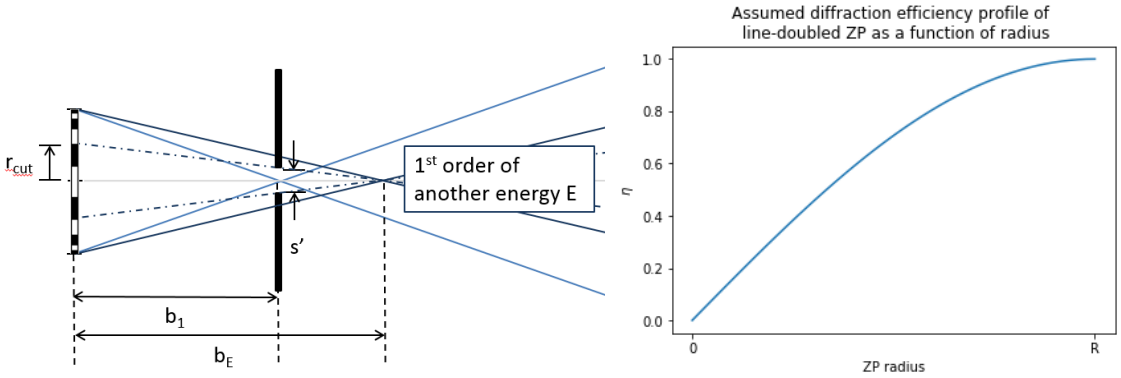

(a) Pinhole cutting the beam **(b)** ZP efficiency profile

Figure 3.8: (a) Illustrates the effect of the pinhole on an energy outside of the bandwidth: the corresponding cone of X-rays (dark blue) gets cut off by the pinhole and only a part of the zone plate with the radius r_{cut} (dashed) contributes to the image. (b) The zone plate efficiency profile which was used in the simulations.

The working distance $b_E(E)$ for X-rays of a certain energy E can be calculated from equations (2.1) and (2.3), and the radius r_{cut} of the remaining contributing part of the ZP after the "cone cutting" of a pinhole of size s' can be derived from simple geometrical considerations in Figure 3.8a as

$$r_{cut}(E) = \frac{s' \cdot b_E(E)}{2 \cdot |b_E(E) - b_1|}, \tag{3.1}$$

where the energy dependence of b_E gives the energy dependence of r_{cut}, which can be used for the simulations. Using the efficiency profile illustrated in Figure 3.8b for a zone plate of radius R, the intensity I going through the pinhole as a function of r_{cut} (and therefore of energy) can be derived as:

$$I(r_{cut}) = -4Rr_{cut} \cdot \cos\left(r_{cut} \cdot \frac{\pi/2}{R}\right) + \frac{8R^2}{\pi} \cdot \sin\left(r_{cut} \cdot \frac{\pi/2}{R}\right) \tag{3.2}$$

The full derivation can be seen in Appendix A. The results of the pinhole-related simulations are illustrated in Figure 4.5.

3.4 Measurement and spatial mapping of diffraction efficiency

In order to determine the diffraction efficiency of a zone plate, one needs to analyze the number of counts diffracted into the zone plate's first order and compare them

with the number of photons impinging on the zone plate. The ratio between these two numbers is the first-order diffraction efficiency. Two different methods were initially considered for this efficiency determination – determining the efficiency from the images collected with the Mönch, and determining it from the number of photons counted by the PMT. However, due to issues presented below, the Mönch was disregarded in this aspect and was used only for the spatial mapping of the diffraction efficiency.

For all measurements, a tube voltage of 40 kV and tube current of 150 μA was used. All measurements were first done with a 12.00 μm Cu filter, then with a 12.85 μm Ni filter, and the resulting counts were subtracted in order to get the counts within the wanted energy interval, with an approximate X-ray energy of 8.4 keV. Before measuring a new zone plate, an alignment as described in Section 3.2.2.2 was performed.

3.4.1 Diffraction efficiency measurement and mapping with the Mönch

This section presents the methods for measuring and mapping the zone plate diffraction efficiency with the Mönch, and explains why it was later used only for the efficiency mapping.

3.4.1.1 Mönch diffraction efficiency mapping

The cone of diffracted light from a zone plate was imaged with the Mönch using the maximum possible exposure time of 1 ms and an acquisition period of 6 ms per frame, recording 100 000 frames per image. The acquisition period is the time needed for the Mönch to analyze the photon data and deliver an image. This time was reduced from 30 ms per frame through the use of a region of interest, reducing the total recording time for an image from 52 minutes to 12 minutes.

3.4.1.2 Mönch diffraction efficiency measurement and why it was disregarded

In order to determine the diffraction efficiency of a zone plate from images collected by the Mönch, two additional images were recorded: one with the 100 μm pinhole in the beam instead of the zone plate, to count the incoming photons, and one with only the 10 μm pinhole in the beam, to count the zeroth-order photons passing straight through the pinhole. After subtracting the Ni-filtered image from the Cu-filtered image for each set of images recorded, the 10 μm-pinhole image was subtracted from the zone plate image. In order for the subtraction operation to be valid, it was assumed that the zone plates have zero diffraction efficiency in the central region corresponding to the area of the pinhole, which is a good approximation for line-doubled zone plates (see Figure 2.4c). The first-order diffraction efficiency was subsequently determined by dividing the number of counts in the resulting image with the number of counts in the reference image made with the 100 μm pinhole. In this type of measurements, a flat- and a dark field correction is usually performed,

correcting for inhomogeneities in the beam and errors in the detector chip, but in these measurements the dark field correction was done automatically by the Mönch and the flat field was considered not to be needed. See Figure 3.9.

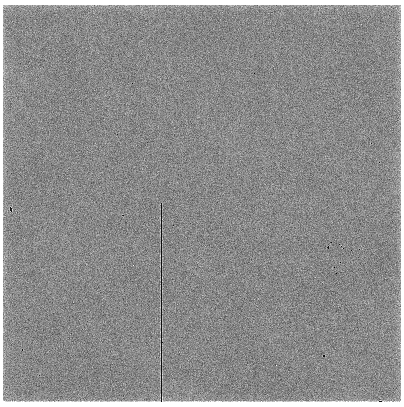

Figure 3.9: Flat field taken with the Mönch detector, filtered with 12 μm Cu, at 15 000 frames and 1 ms exposure time per frame. The full field of view of the detector is visible and the beam appears to be homogeneous, indicating that no flat field correction has to be done in the imaging. The black line is an array of dead pixels.

The efficiencies determined in this way using the Mönch differed considerably from the efficiencies determined using the PMT. The raw data was therefore analyzed with regards to photon energy, revealing spectra reaching energies far above the tube voltage of 40 kV, see Figure 3.10a. This was a clear sign of photon pileup, indicating that the photon flux was too high for the detector to be able to count each photon separately and leading to the detector recording several photons as one with a summed-up energy. Measurements were repeated at the lowest possible X-ray tube current, 10 μA, with the same problems.

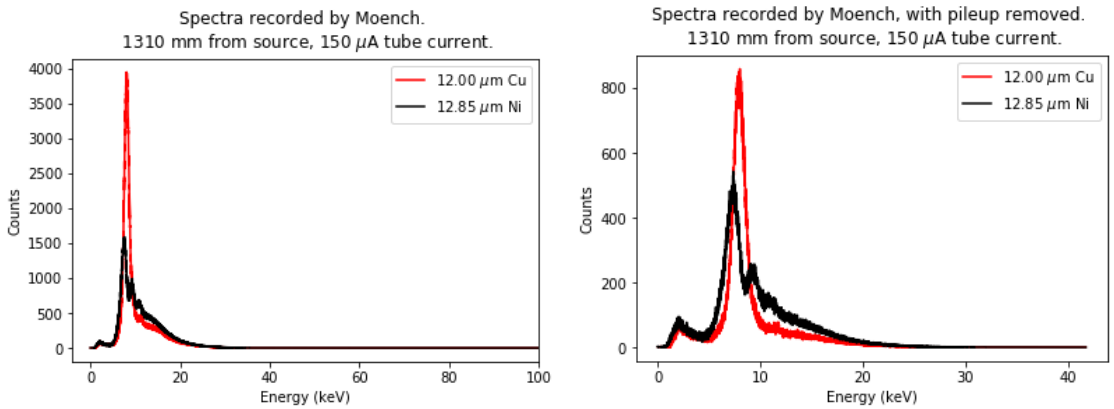

(a) Before pileup removal **(b)** After pileup removal

Figure 3.10: Photon energies recorded by the Mönch, (a) before and (b) after pileup removal. All spectra have been normalized to the approximate thickness of the Si chip in the detector, 300 μm. The curves in (a) have been cut at a certain energy for illustration purposes; in reality, the spectra go up to 800 keV.

An algorithm was subsequently used to remove the piled-up photons from the raw data, resulting in spectra with photon energies within the plausible range, see Figure 3.10b. The result however showed a clear mismatch of the curves for the two different filters, and also of the positions of the L_α peaks. Measurements of the same spectra with a spectrometer showed that the spectra overlapped very well and that the peak position was as expected, see Figure 4.9b, indicating an issue with the pileup removal. It was indeed reported that the pileup removal of the Mönch is energy-dependent, removing more photons from the intense peaks compared to the less intense peaks and bremsstrahlung. Since the efficiency measurements in this thesis relied on the energy-dependent characteristics of the filters, the diffraction efficiency measurements with the Mönch were disregarded. The Mönch was nevertheless crucial for the diffraction efficiency mapping.

3.4.2 Diffraction efficiency measurement with the PMT

The diffraction efficiencies were determined using the PMT by scanning the ZP in x and y over a range covering $\pm$ the zone plate diameter in order to count the number of photons diffracted into the different diffraction orders. Since the detector area of the PMT – which is about 3 mm in diameter – is much larger than the pinhole, it did not have to be moved during the scans but could simply detect the photons emerging from the pinhole which was used to sample the beam. Figure 3.11 shows an explanation of the expected results.

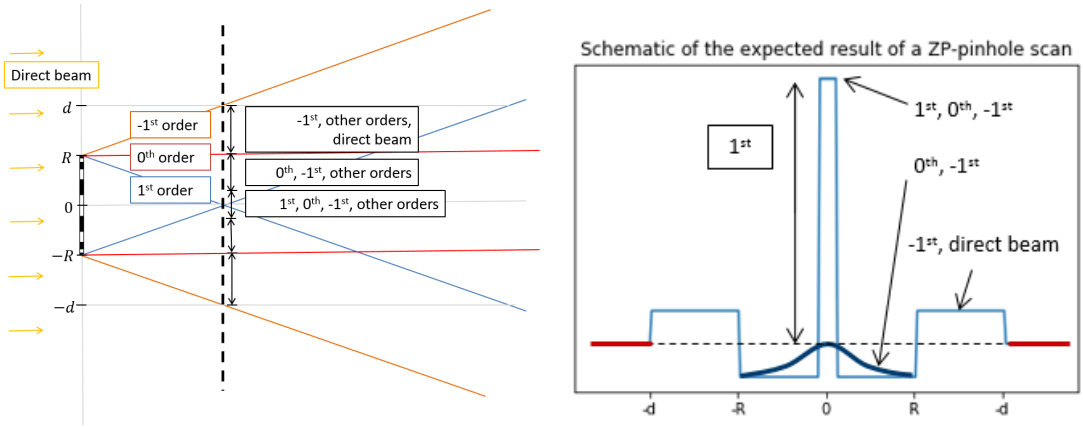

(a) Diffraction orders during the scan **(b)** Simplified scan result

Figure 3.11: An explanation of the result from a scan across the diffraction orders of a zone plate with diameter $d = 2R$. (a) shows a schematic of the different diffraction orders. The dashed line shows the plane in which the pinhole is put; by scanning the ZP, the number of photons in the different orders can be counted by the PMT positioned after the pinhole. (b) presents a simplified graph of the expected results, with the diffraction order contributions indicated. The red lines indicate the points used to approximate the zeroth-order counts. The actual result has rather rounded plateaus and peaks due to the convolution of the shape of the pinhole (with well-defined edges but also a recess where higher-energy photons can be transmitted) and the source spot (which is assumed to be Gaussian).

For a zone plate with constant efficiency along its radius, the number of photons diffracted into the first order can be obtained simply by subtracting the counts in the zeroth order (extracted from the plateaus in the region of $0 \pm R$) from the peak value at 0. The zone plates fabricated in this thesis are however line-doubled and designed to be the least effective in the middle see Figure 2.4c, meaning that the counts in the zeroth order increase towards the center. Assuming that the zeroth order is at its maximum value in the ZP center, the zeroth order counts at that point will correspond simply to what is transmitted through the zone plate without being diffracted. This can be approximated by the number of photons transmitted through the membrane, indicated in red in Figure 3.11b, since the absorption in the center of line-doubled FZPs (where the structures mostly consist of low-Z HSQ) can be assumed to be negligible. Subtracting this value from the peak value therefore gave a better estimate of the number of photons diffracted into the first order N_{first}. The reference value N_0' was obtained by counting the number of photons coming through a 100 μm pinhole with the zone plate moved out of the beam. The absolute diffraction efficiency was obtained by dividing these two values, $\eta = N_{first}/N_0'$.

An example of a complete diffraction efficiency measurement is shown in Figure 3.12. Data has been acquired with a step size of 1 μm and the counts at each point have been recorded during 10 seconds to minimize the effect of noise. The data points marked in green are the ones to approximate the zeroth order value at the coordinate of the peak. Subtracting the average of the green data point counts from the counts in the peak yields the first order counts; the first order efficiency is then calculated by dividing this number with the average of the counts in the reference scan in Figure 3.12b.

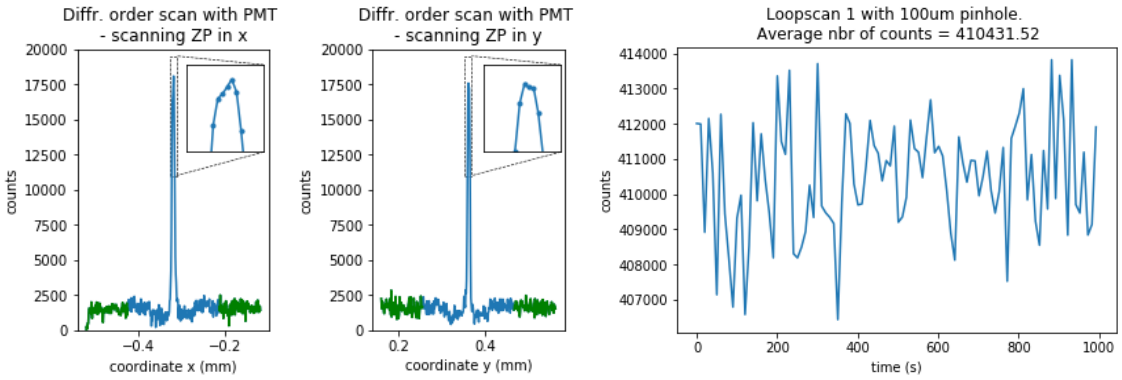

(a) Scan of ZP in x and y **(b)** Reference measurement

Figure 3.12: Illustration of the measurements done for the determination of the absolute diffraction efficiency using the PMT. (a) shows the results of the scans when moving a ZP in x and y, while recording the number of photons coming from it through the pinhole. Points marked in green are the ones whose average is subtracted from the peak value in order to get the number of photons diffracted into the first order. The insets show enlarged images of the peaks. (b) shows the reference scan measured without any zone plate in the beam, where the average number of counts is used to determine the incoming intensity. Both (a) and (b) show the results after subtraction of the counts recorded with the Cu- and the Ni-filter.

The insets in Figure 3.12a show a closer look at the peaks. As mentioned in Section 3.2.2.1, one of the criteria for the choice of the pinhole diameter was that the projection of the source spot size had to fit inside it, and this is proven here since a plateau of the expected size can be seen. 3-4 data points are visible in each plateau; for the source-zone plate distance of 128 mm, an assumed source spot size of 10 μm and a zone plate working distance of 46 mm an expected projection of the source spot which is 3.6 μm in diameter can be calculated from simple geometrical optics.

3.4.2.1 Errors

As in all experimental measurements, the diffraction efficiency values will contain certain errors. The absolute errors obtained in the efficiency measurements in this thesis vary between 0.1% and 0.4%, on average being about 0.2% which in relative values corresponded to an error of about 7%. This can be seen as a reasonable value, considering how the measurements are made. The errors ϵ_x and ϵ_y for the diffraction order scans in x and y and the total error ϵ_{tot} are calculated with a standard error propagation formula

$$\epsilon_{x,y} = \frac{\sqrt{\sigma_{max}^2 + \sigma_{zeroth}^2 + (max - zeroth)^2 \cdot (\sigma_{ref}/ref)^2}}{ref}$$

$$\epsilon_{tot} = \frac{\epsilon_x^2 + \epsilon_y^2}{2}$$

where σ_{max}, σ_{zeroth}, and σ_{ref} are the standard deviations for the peak value, the zeroth order counts, and the reference.

The standard deviation for the zeroth order is taken from the set of measurements made on zone plates from the same chip, the standard deviation for the reference from three identical measurements with the 100 μm pinhole, and the standard deviation in the first order from the counts from five coordinates around the center of the scan peak, chosen to account for a placement error occurring in the alignment of the zone plate to the pinhole. At first the standard deviation in the peak value was assumed to be equal to shot noise, but this did not account for the variations in efficiency obtained when repeating an efficiency measurement for a certain zone plate. An example of repetitions on zone plate iiB3 from sample VY181119a gave the following efficiencies: 6.07%, 6.27%, 6.22%, 6.09%, 6.31%, 6.21%, 6.27%, 6.30%, 6.26%, 6.08%, yielding a standard deviation in the values of 0.09%. Repeating the same measurement on zone plates A3, B5, C4 and D4 yielded standard deviations of up to 0.25% (however, based on fewer samples). The fluctuations in the source flux and the shot noise in the detection also did not account for the large variations, see Figure 3.13a, where the shot noise and the standard deviation are of the same order of magnitude.

The conclusion was that a systematic error probably came from the alignment of the zone plate to the pinhole, and this was included by taking the five maximum values in the peak into account in the error calculation. Due to shot noise in the number of counts in the peak, slightly different coordinates could be chosen as optimal in the alignment – see Figure 3.12a where the maximum value is not in the center of the peak. Since the step size in the diffraction order measurement is 1 μm,

the placement difference can be several microns between different measurements. A further contributing factor could be the positioning error of the motorized stages which move the zone plate between and during measurements, but this was assumed to be smaller in comparison. Other sources of errors could be a slightly different pinhole size than expected, inaccuracy in the positioning of the zone plate and pinhole *along* the optical axis, and the actual size of the focused source spot, dependent on the actual (here just approximated) source spot size.

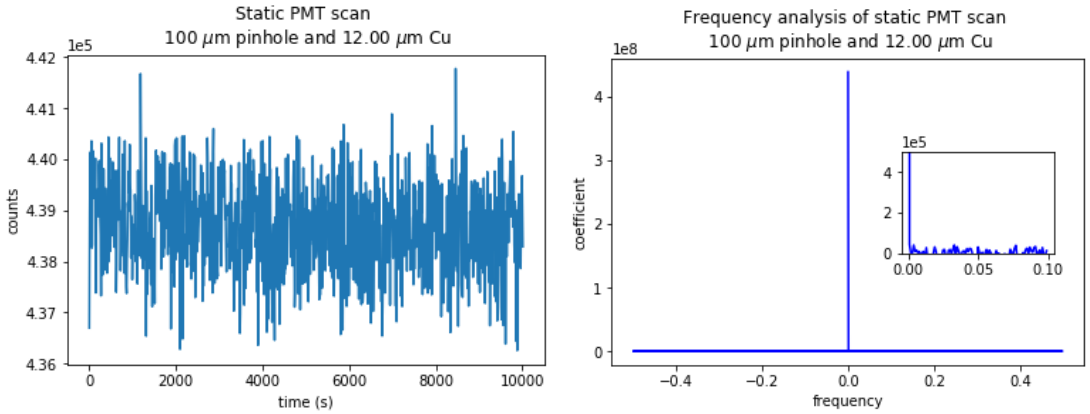

(a) Long scan of source flux **(b)** Frequency analysis

Figure 3.13: An analysis of the fluctuations in the detection of the flux from the source. (a) shows a long static scan made with the PMT, having a 100 μm pinhole and the 12 μm Cu filter in the beam. The occurrence of different frequencies is shown in (b), with an inset emphasizing the fact that no specific frequencies can be read out.

3.4.3 Diffraction efficiency measurement and mapping at the ANATOMIX beamline of Synchrotron SOLEIL

In order to confirm that the measurements done with the X-ray-tube-based setup were reasonable, the diffraction efficiency and mapping measurements were done also at the ANATOMIX beamline of Synchrotron SOLEIL. The measurements were performed with an approximate X-ray energy of 10 keV, with a setup similar to the one used for the diffraction efficiencies in this thesis, but with a PCO camera detection system and an image-based diffraction efficiency determination.

3.5 Measurement of misalignment in double-sided Fresnel zone plates

A displacement of the frontside zone plate with respect to the backside zone plate in a double-sided structure can be described as in Figure 3.14. One zone of each of the two zone plate halves is illustrated, misaligned with an offset of l_{off}; the height of the frontside zone plate is h_{front}, the height of the backside zone plate h_{back}, and the thickness of the silicon nitride membrane on which the zone plates are fabricated

t_{membr}. In a perfectly aligned double-sided zone plate, there would be no offset l_{off} and the two zones would be positioned right below each other, with their respective centers of mass aligned and with the total structure height contributing to the phase shift of the structure. In the misaligned case illustrated in Figure 3.14, only a part of the zones is contributing, decreasing the total diffraction efficiency of the zone plate. One can increase the efficiency by aligning the centers of mass of the front and back zones by tilting the whole structure. The better the centers of mass are aligned, the more of the zones contributes to the phase shifting function of the structures and the higher the diffraction efficiency. A maximum in the efficiency should be reached for a tilting angle α for which the centers of mass are perfectly aligned.

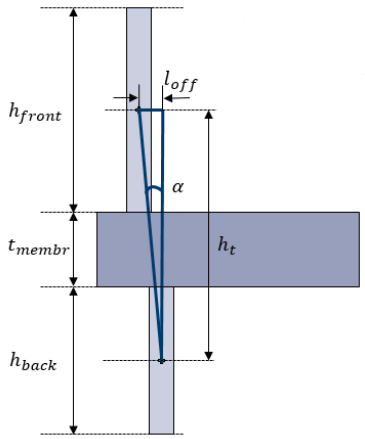

Figure 3.14: Schematic of a slightly misaligned double-sided zone plate. Illustrated is a zone of the frontside zone plate, the silicon nitride membrane, and the same zone of the backside zone plate which is offset from the front by a distance l_{off}. The tilt angle needed to compensate for the misalignment is α.

The tilting, or rotation, should be done around an axis which is perpendicular to both the membrane and the zones of the zone plate, which in our case corresponds to tilting around the axes x and y as they were defined in Figure 3.4. Knowing the height of the structure on the frontside and on the backside and the thickness of the membrane, and assuming perpendicular structure sidewalls, one can then calculate the offset l_{off}:

$$h_t = h_{front}/2 + t_{membr} + h_{back}/2 \tag{3.3}$$

$$l_{off} = h_t \tan\alpha. \tag{3.4}$$

4

Results and discussion

The following sections present the built X-ray tube setup, the simulated and measured X-ray tube spectra, and the results from the diffraction efficiency and misalignment measurements.

4.1 X-ray-tube-based setup

The finalized setup and its main parts is shown in Figure 4.1. The Mönch detector is out of the field of view and is instead shown in Figure 4.2b.

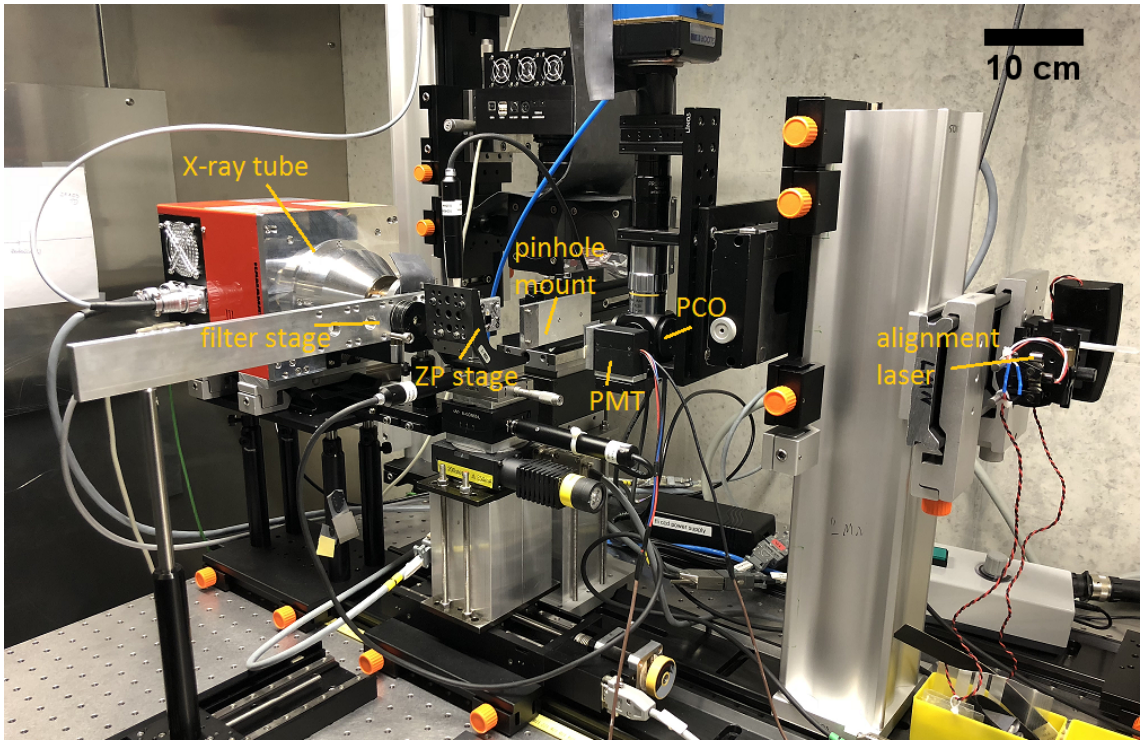

Figure 4.1: The final X-ray tube based setup. Highlighted in the image is the X-ray tube, filter stage, zone plate stage, pinhole stage, PMT, PCO camera and alignment laser. The Mönch detector is out of the field of view.

Figure 4.2a shows a closer view on what happens to the X-ray beam after emerging from the source, with the path through a filter, zone plate, and pinhole indicated. A 0.3 mm thick tantalum shielding was added to the backside of both the zone plate-

and pinhole holder to prevent high-energy photons from reaching the detector by passing through the aluminum mounts.

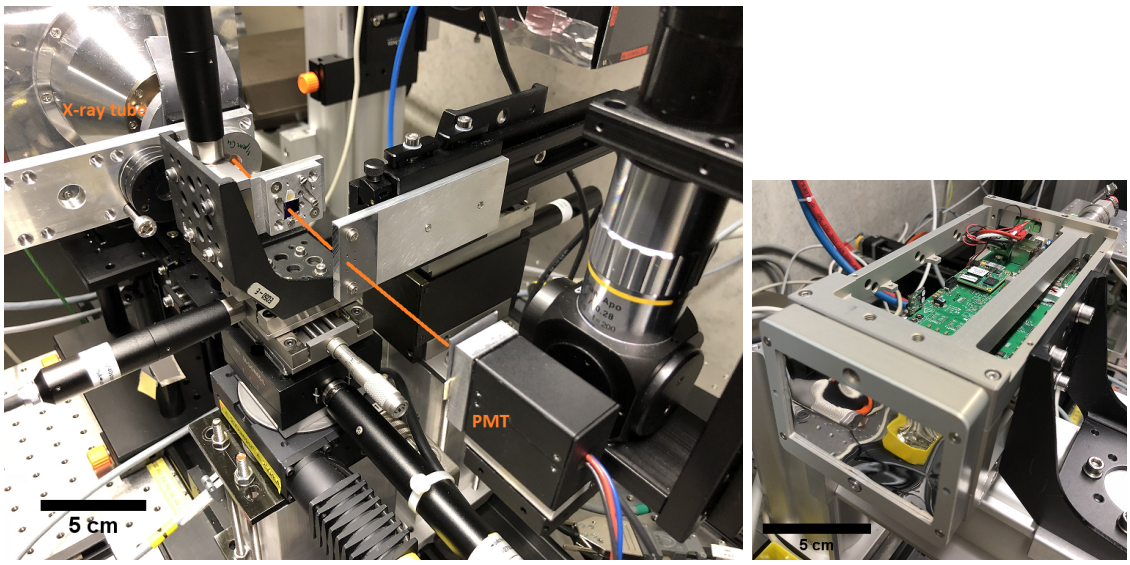

(a) The optical path **(b)** Mönch detector

Figure 4.2: Setup details. (a) A close-up on the optical path. X-rays emerging from the X-ray tube pass through a filter, go through a zone plate, enter a pinhole and then pass further to the PMT, PCO or the Mönch. (c) The Mönch detector in its casing. The front of the detector is covered by a reflective window shielding it from visible light.

4.2 X-ray tube spectra

The appearance of the X-ray spectrum with different filters and pinhole sizes was first simulated and then confirmed through spectrometer measurements; the results are presented in this section. The energy scale in the figures is kept identical throughout the simulations and measurements in order to make a comparison between them easier, even though the measurements have energies up to 40 keV and the simulations consist of data only up to 30 keV.

4.2.1 Simulated spectra

Figure 4.3 shows the simulated spectra for 12 μm Cu and Ni filters at different distances from the source. The three peaks in the unfiltered spectra contain, from left to right, the $L_{\alpha 1,2}$, $L_{\beta 1,2}$ and $L_{\gamma 1}$ peaks, respectively. Due to the low energy resolution of 0.5 keV in the input data, the separate sub-peaks cannot be distinguished. The distance of 165 mm was chosen due to it being the shortest distance at which the spectrum could be measured with the spectrometer; the other two distances were chosen to show the effect of the longer air path on the X-ray photons. The spectra were simulated for equally thick Cu- and Ni filters; the slightly adjusted Ni thickness used for the diffraction efficiency measurements would not have affected the simulations

notably. A 150 nm thick Be window in front of the X-ray tube was not accounted for in the simulations due to its transmission being higher than 95% for the energies of interest, meaning that it would not significantly affect the spectra.

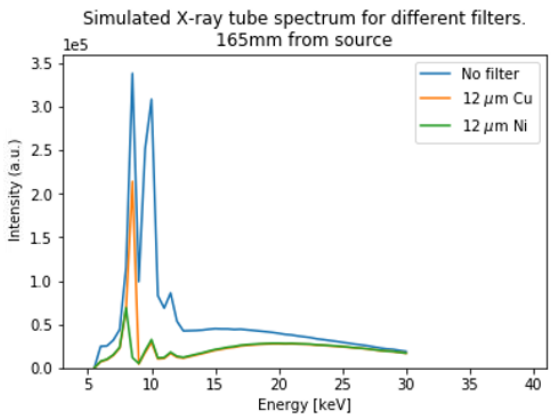

(a) 165 mm from source

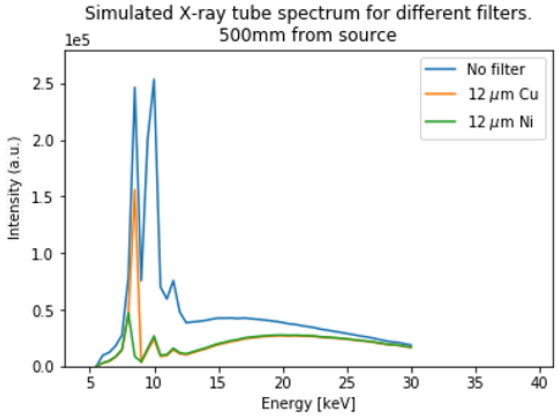

(b) 500 mm from source

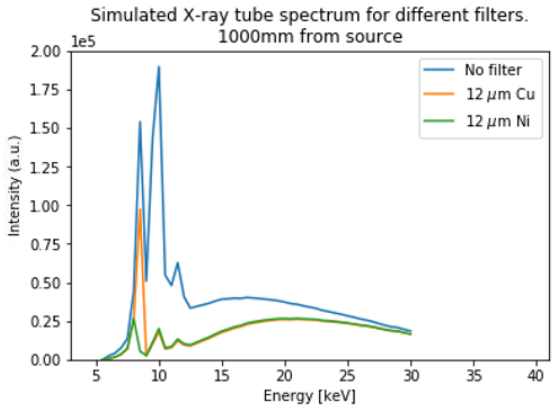

(c) 1000 mm from source

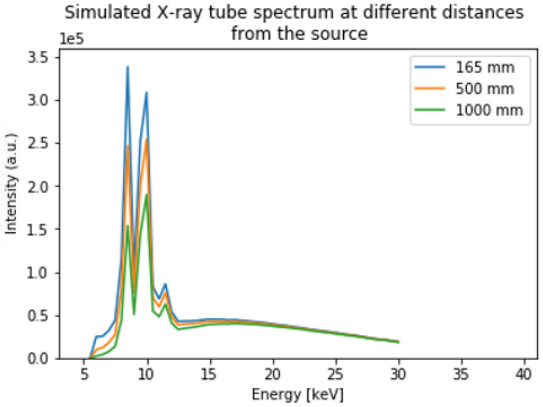

(d) No filter, at different distances from the source

Figure 4.3: X-ray tube spectra, unfiltered (blue), filtered with 12.00 μm Cu (orange) and filtered with 12.00 μm Ni (green), simulated at different distances from the source point. (a)-(c) show increasing distances. Notice the decreasing number of counts. (d) shows the unfiltered spectrum at different distances from the source.

The effect of the filters on the spectrum is the same for all the distances, as expected. Figure 4.3d shows the unfiltered spectrum at different distances from the source and confirms that the absorption of X-ray photons in air affects the number of counts significantly. It is the reason both behind the fact that the bremsstrahlung-shoulder in the very beginning of the spectrum is lower for larger distances from the source, and behind the relative decrease in height of the first peak in the spectrum, since the air absorption is higher for lower energy photons. See Figure 3.5.

Figure 4.4 shows the comparison between filter-subtracted spectra for different filter thicknesses. The curves for the different filter thicknesses cannot be distinguished, indicating that the number of counts in the subtracted spectrum does not differ

substantially between the different filter thicknesses. In all cases, the wanted $L_{\alpha 1,2}$ peak is clearly isolated, but at the cost of a decrease in counts.

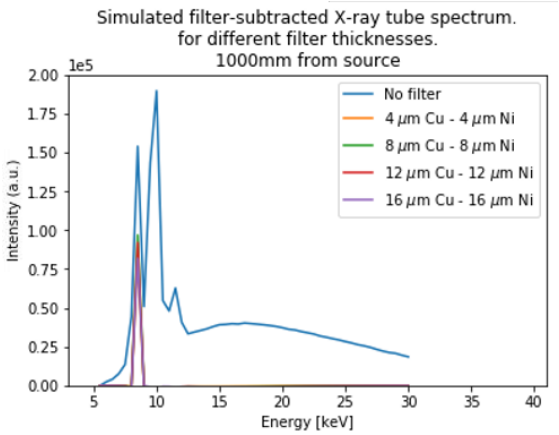

Figure 4.4: The result of subtracting the spectra for Cu and Ni for different thicknesses of the filters, at 1000 mm from the source.

Figure 4.5 shows the effect of a pinhole on the spectrum of the X-ray tube. In Figure 4.5a, the ”cutting” effect of pinholes of three different diameters is illustrated. The remaining radius on the zone plate is never smaller than the radius of the pinhole. Due to the already mentioned low energy resolution of the spectrum, the plateau in the spectrum – corresponding to the bandwidth of energies that is let through the pinhole unaffected – is not defined for the 5 μm pinhole, which has a bandwidth including only one of the energy values in the input data. In Figure 4.5b, the corresponding intensity emerging after the pinhole ”cutting” is shown. The zone plate efficiency profile shown in Figure 3.8b was assumed. The values are normalized with respect to the values which pass through the pinhole unaffected. The plateau for energies within the bandwidth is not defined for the 5 μm pinhole for the same reason as in Figure 4.5a. The non-zero values for the intensity even for the highest energies is explained by the fact that all energies can pass through the pinhole in the zeroth order.

Figure 4.5c shows a comparison between the effects of pinholes of different sizes on the X-ray tube spectrum, confirming that small pinholes cut the spectrum more than large pinholes, and Figure 4.5d shows a comparison between the effect of a 10 μm pinhole and the 12 μm filter-subtracted spectrum introduced in Figure 4.4. It is apparent that the filtered spectrum falls into the acceptance of the pinhole, which is a requirement for the setup measurements to function as expected. The 5 μm pinhole, when comparing with Figure 4.5d, would start cutting the peak, giving non-reproducible results depending on its relative alignment to the zone plate. The larger pinholes, however, with a larger acceptance, would work well with these filter settings.

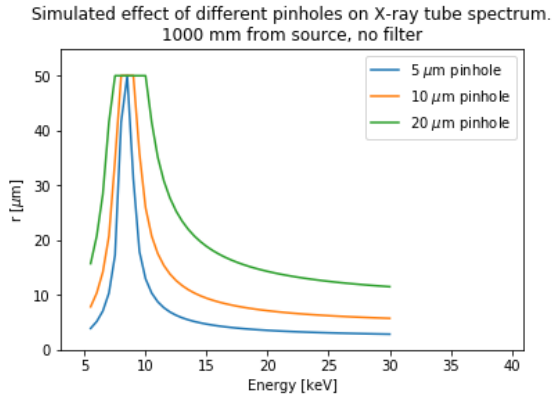

(a) Remaining radius of contributing part of zone plate

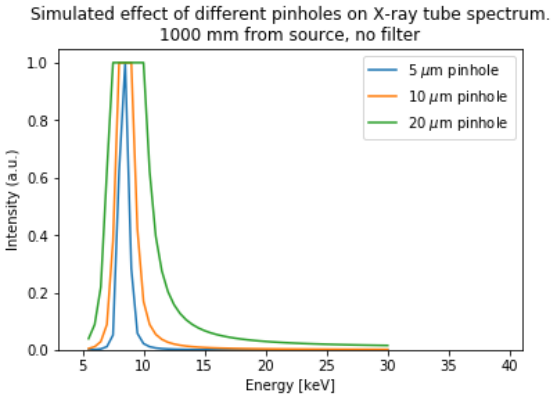

(b) Corresponding intensity

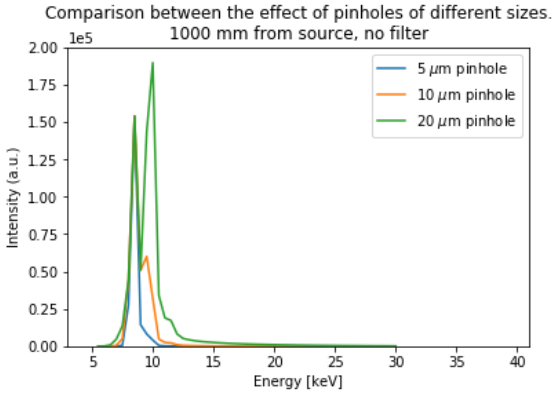

(c) Effect of pinholes of different sizes

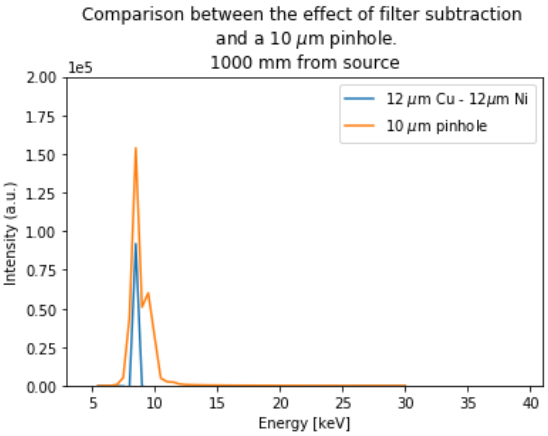

(d) Filter-subtracted vs. pinhole-cut spectrum

Figure 4.5: Characteristics appearing due to the use of a pinhole. (a) The FZP radius which is still contributing after the pinhole cutting as a function of energy. (b) The resulting intensity coming through the pinhole, taking into account the dependence of the zone plate diffraction efficiency on the radius. (c) The effect of pinholes of different sizes on the X-ray tube spectrum. (d) Comparison between the effect of a 10 μm pinhole and the subtraction of 12 μm Cu- and Ni filters on the spectrum.

4.2.2 Measured spectra

Figure 4.6 shows the result of a scan made to determine the best relative position of the source, ZP and pinhole along the optical axis. The average of the maxima of the fits was determined to be at 117.17 mm from the source, and this is where the zone plates were put for the diffraction efficiency measurements. With the pinhole being another 47.83 mm away, this gives a value for the focal length f equal to 34.0 mm. Inserting the characteristics of the zone plates (100 μm diameter, 50 nm outermost zone width) and an X-ray energy of 8.4 keV into equation (2.1) gives a value of $f = 33.8$ mm, which means that the measurement corresponded well to what

was expected. The measurement also showed that this type of scan is a valid way of optimizing the relative position of the zone plates and pinholes. It will be feasible even for zone plates with different dimensions – by knowing the approximate working distance of a zone plate with given dimensions, one can use this type of scan to put the zone plate at its optimal position along the optical axis, not relying on manual placements or measurements. One can assume that the method will be valid even for zone plates with completely unknown characteristics if the scan range along the optical axis is long enough, which is a big advantage.

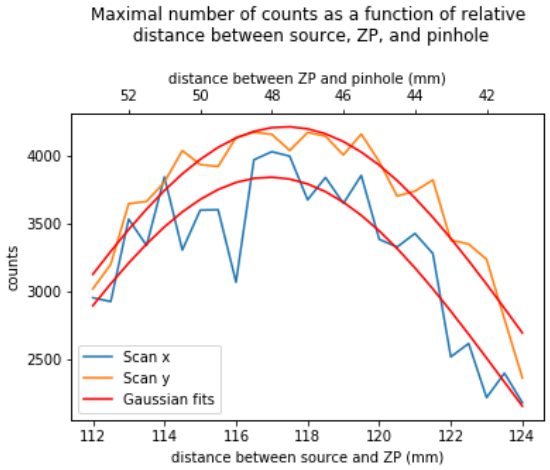

Figure 4.6: Measured maximum number of counts as a function of the distance from the source to the zone plate and the distance from the zone plate to the pinhole. The scanning at each point along the optical axis has been made both in x (blue) and in y (orange). Gaussian fits have been done in order to find the optimal position.

Figure 4.7, to be compared with Figure 4.3, shows the measured spectrum for the chosen filters at different distances from the source. The comparison between the simulated and the measured spectra shows that the simulations closely reproduce the measured results. In 4.7d one can see the clear trend of decreasing counts when moving away from the source, with an approximate ratio of 4 between the maximum number of counts at 1000 mm and at 500 mm, corresponding well to the fact that the number of counts should decrease with the square of the distance from the source. This trend cannot be seen in the simulations, since the difference in solid angle taken up by the measuring device was not taken into account. The less defined peaks at 165 mm from the source arise due to saturation of the spectrometer.

Figure 4.8, to be compared with Figure 4.4, shows the unfiltered tungsten spectrum and filter-subtracted spectra for different filter thicknesses. Just as in the simulations, the subtraction of filter data leads to a drastically reduced number of counts. This is the price that needs to be payed for the highly improved monochromaticity of the beam. Another conclusion confirming the simulations is that the number of counts left after the filter subtraction does not change substantially with filter thickness. This, together with the result shown in Figure 4.5d where it is confirmed that the filtered spectrum falls into the acceptance of the pinhole, concludes that a combination of 12.00 μm filters and a 10 μm pinhole works well for the measurements.

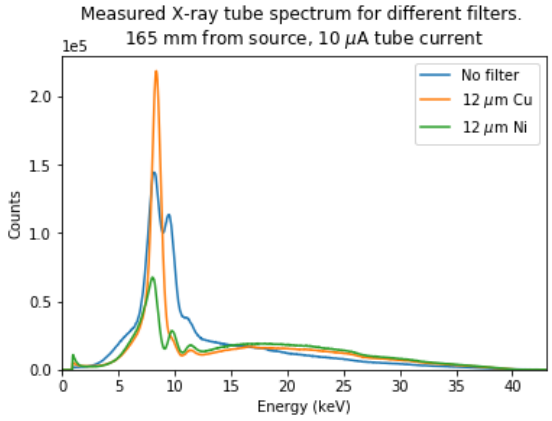

(a) 165 mm from source, 10 μA tube current

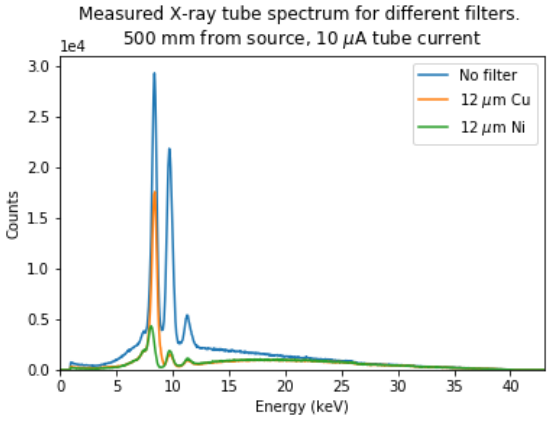

(b) 500 mm from source, 10 μA tube current

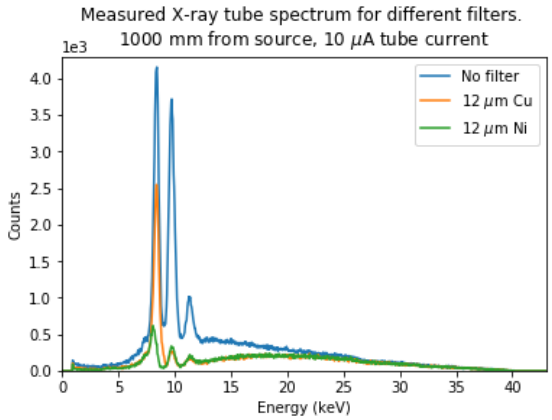

(c) 1000 mm from source, 10 μA tube current

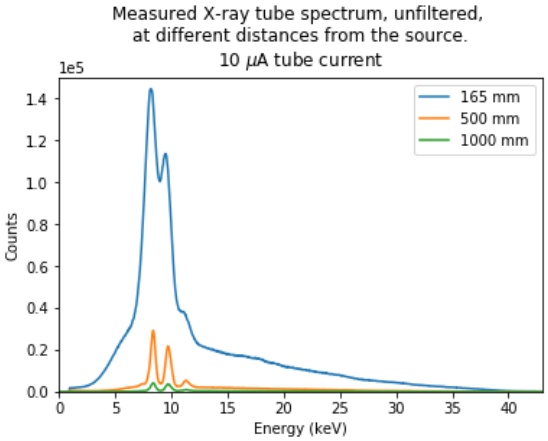

(d) No filter, at different distances from the source, 10 μA tube current

Figure 4.7: X-ray tube spectra, unfiltered (blue), filtered with 12 μm Cu (orange) and filtered with 12 μm Ni (green), measured at different distances from the source. (a), (b) and (c) show increasing distances. Notice the decreasing number of counts. (d) shows the unfiltered spectrum at different distances from the source.

In order to match the transmission of the two filters better, a 12.85 μm Ni filter was used instead of a 12.00 μm one as mentioned in Section 3.2.2.3. A comparison between the spectra for the different filter thicknesses is shown in Figure 4.9, measured at the detector position. One can see that a slightly thicker Ni filter makes the spectra agree slightly better for energies higher than the $L_{\alpha 1,2}$ peak, and makes the differential measurements more reliable.

To summarize: with the exception for some small differences, the measured and simulated spectra correlate very well. The measured spectra have much finer sampling in energy compared to the simulations and therefore reflect the real X-ray tube spectrum better, but the simulations are nevertheless useful in the design of the X-ray tube setup.

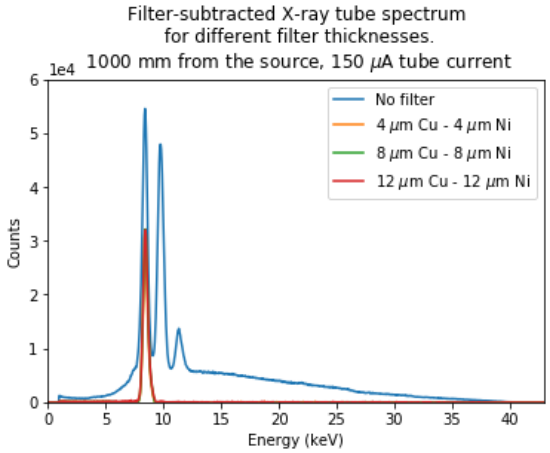

Figure 4.8: The measured result of subtracting the spectra for Cu and Ni for different filter thicknesses. No difference in the resulting counts is visible.

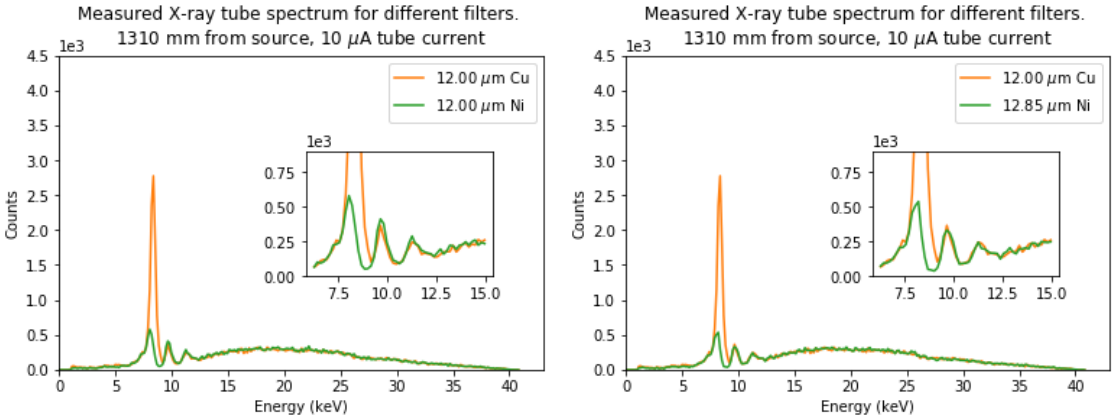

(a) 12.00 μm Cu and 12.00 μm Ni **(b)** 12.00 μm Cu and 12.85 μm Ni

Figure 4.9: Cu- and Ni-filtered spectra for different Ni filter thicknesses. The agreement of the curves for energies higher than approximately 9 keV is better in (b); this is the combination used for the diffraction efficiency measurements.

4.3 Single-sided Fresnel zone plates

In the course of this master's thesis work, a number of chips with single-sided zone plates with different characteristics were fabricated and subsequently measured in the X-ray-tube-based setup. Out of these, some chips were used to make double-sided zone plates and were measured again. Some zone plate chips were measured only as double-sided structures. Only the two chips where the zone plates were measured both as single-sided and double-sided will be presented here; the complete set of results can be seen in Appendix B.

A general layout of the zone plate distribution on one chip membrane is shown in Figure 4.10. An asymmetric layout was chosen in order to easily identify the zone plates for the efficiency measurements. HSQ- and Ir duty cycles according to the

optimal values mentioned in Section 2.1.3 were aimed for in the fabrication; the resulting duty cycles were within 10% of the design values.

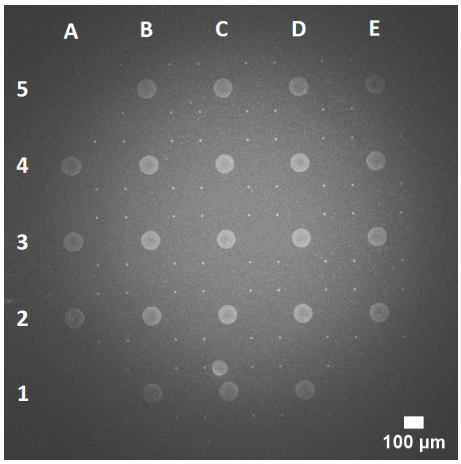

Figure 4.10: SEM image giving an overview of the zone plate- and marker layout and labelling on the membrane. Four alignment markers are visible around every zone plate. The feature slightly above zone plate C1 is no zone plate but an HSQ residue.

All of the diffraction efficiency measurements mentioned in this section were made with the zone plates and pinhole placed according to the distances obtained from Figure 4.6. The detector was placed at a distance of 1310 mm downstream from the source, corresponding to a distance of 1135 mm from the pinhole . The diffraction efficiency maps have, unless stated otherwise, been normalized to a scale from 0 to 50 photon counts. The zone plate diameters on the maps correspond to approximately 100 pixels.

4.3.1 Sample VY180821a ”no mark”

Table 4.1 shows the diffraction efficiency maps made of the sample VY180821a ”no mark” by the Mönch detector. Table 4.2 shows the characteristics of the zone plates on the chip: in (a) are the heights, used to calculate the maximum theoretical diffraction efficiencies in (b), and in (c) are the PMT-measured absolute diffraction efficiencies in percent. The tables are colour-coded in order to make the comparison between zone plates on this and on other chips easier, and to better show trends in heights and efficiencies. As mentioned in Section 3.1, the low angular rotation speed used in the HSQ spin coating leads to inhomogeneous zone plate heights over the membrane, which is apparent from the broad range of heights presented in Table 4.2a.

All of the diffraction efficiency maps in Table 4.1 are darker in the middle, confirming what is expected for the line-doubled design of the zone plate where the efficiency goes to zero towards the center. The bright spot in the center of every zone plate is the zeroth order going through the 10 μm pinhole. The zone plate maps in the lower middle half of the array are brighter than the others, indicating a higher diffraction efficiency, confirmed also by the measured efficiencies presented in Table 4.2c.

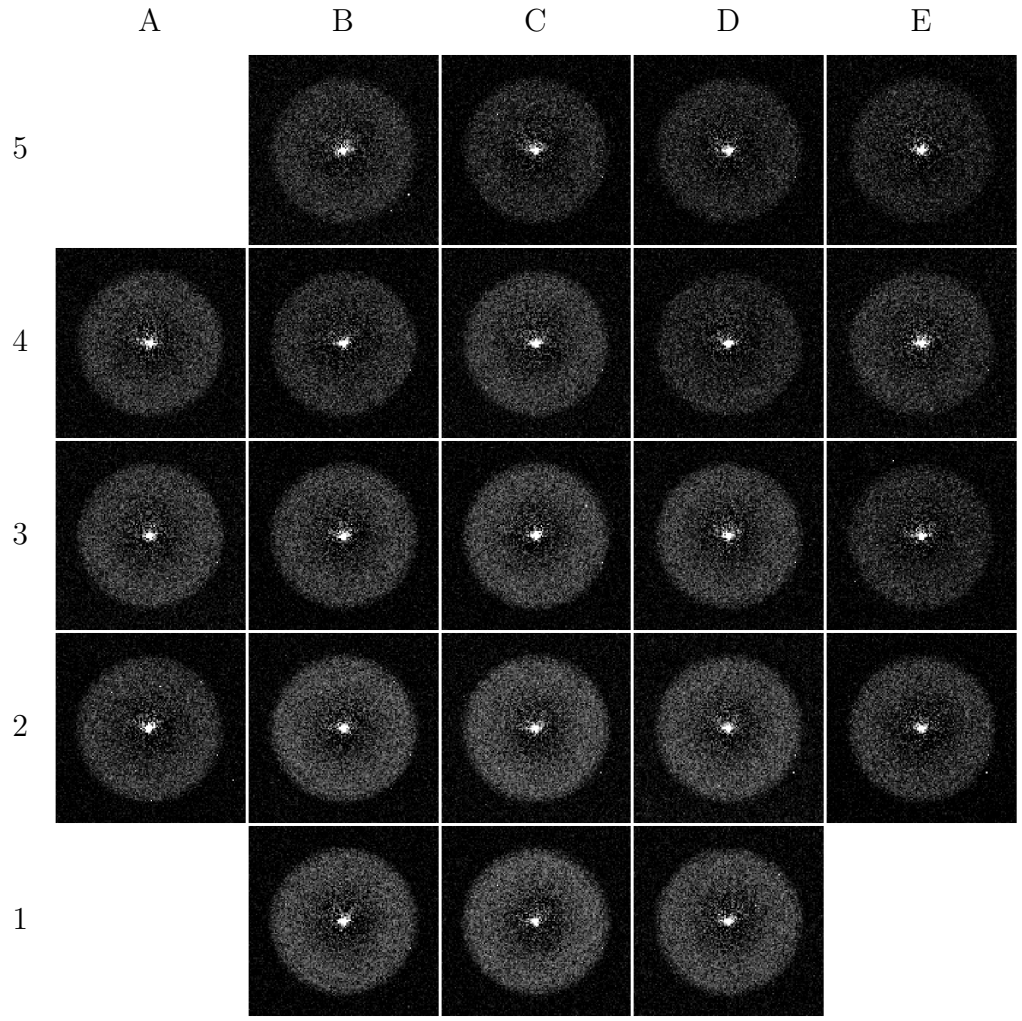

Table 4.1: Mönch diffraction efficiency maps of sample VY180821a "no mark".

	A	B	C	D	E
5		0.56	0.57	0.54	0.53
4	0.62	0.67	0.65	0.64	0.63
3	0.66	0.72	0.73	0.70	0.65
2	0.71	0.77	0.78	0.73	0.69
1		0.80	0.80	0.77	

(a) ZP heights in μm.

	A	B	C	D	E
5		11.5	11.9	10.9	10.5
4	13.4	15.2	14.4	14.1	13.9
3	15.0	16.9	17.3	16.2	14.4
2	16.6	18.7	18.9	17.5	16.0
1		19.6	19.8	18.9	

(b) Corresponding max. theoretical diffraction efficiencies in percent.

	A	B	C	D	E
5		2.5	2.5	2.5	2.1
4	3.1	3.1	3.3	2.7	2.6
3	3.5	3.8	4.0	3.7	3.0
2	3.7	4.5	4.3	3.9	3.6
1		4.5	4.8	4.3	

(c) Measured ZP efficiencies in percent.

Table 4.2: ZP characteristics: VY180821a "no mark".

When comparing Tables 4.2a and 4.2b one can see that the higher the zone plate, the higher the maximum theoretical diffraction efficiency, just as expected for heights in this range. This is easily motivated by the graph in Figure 2.3, where the heights in question all are on the leftmost, increasing, part of the efficiency curve for 8.4 keV. When on the other hand comparing Table 4.2b with Table 4.2c, one sees that the measured efficiencies are noticeably smaller than the theoretical ones. The calculation uses equation (2.8) and assumes a constant duty cycle of 0.5, something which is not true in the case of line-doubled zone plates, since the Ir duty cycle changes over the extent of the zone plate. Also, the efficiency formula assumes completely transparent zones between the phase-shifting zones, which is not completely true for the HSQ structures which have a small but finite absorption. Finally, it is hard to develop narrow, close-standing structures such as the outer zone plate zones in a way that the sidewalls are completely straight. The width of the HSQ lines usually increases towards the membrane, which can lead to the joining of neighbouring zones towards the periphery of the zone plate where they are standing more closely. This means that the actual height contributing to the phase difference between the phase-shifting and transparent zones usually is smaller than the one measured in the SEM. All these reasons makes it impossible to reach the theoretical maximum diffraction efficiency even with an ideal line-doubled zone plate. The theoretical efficiencies are instead used simply to get an idea of what zone plates should be better than others, and as can be seen in 4.2c, the trends in the measured efficiencies follow the trends in the theoretical efficiencies very well.

4.3.2 Sample VY181015a ”mark”

Sample VY181015a ”mark” was made using hot development, a method chosen to try to achieve straighter sidewalls in the HSQ structures [46, 47]. The diffraction efficiency maps of the zone plates on this chip are shown in Table 4.3 and the corresponding characteristics in Table 4.4. The trends seen in the zone plate heights and theoretical maximum diffraction efficiencies are reproduced in the measured efficiencies. The efficiencies are however all lower than the ones measured for sample VY180821a ”no mark”, and the efficiency maps are also much less bright. This can be explained by Figure 4.11b which shows a SEM image of zone plate C3, representative of the zone plates on the chip. The structure quality itself seems to be good, but there are Ir-covered resist residues all over the structures, most probably arising due to incomplete rinsing after the development. The image can be compared with Figure 4.11a, showing a very clean zone plate from sample VY180821a ”no mark”.

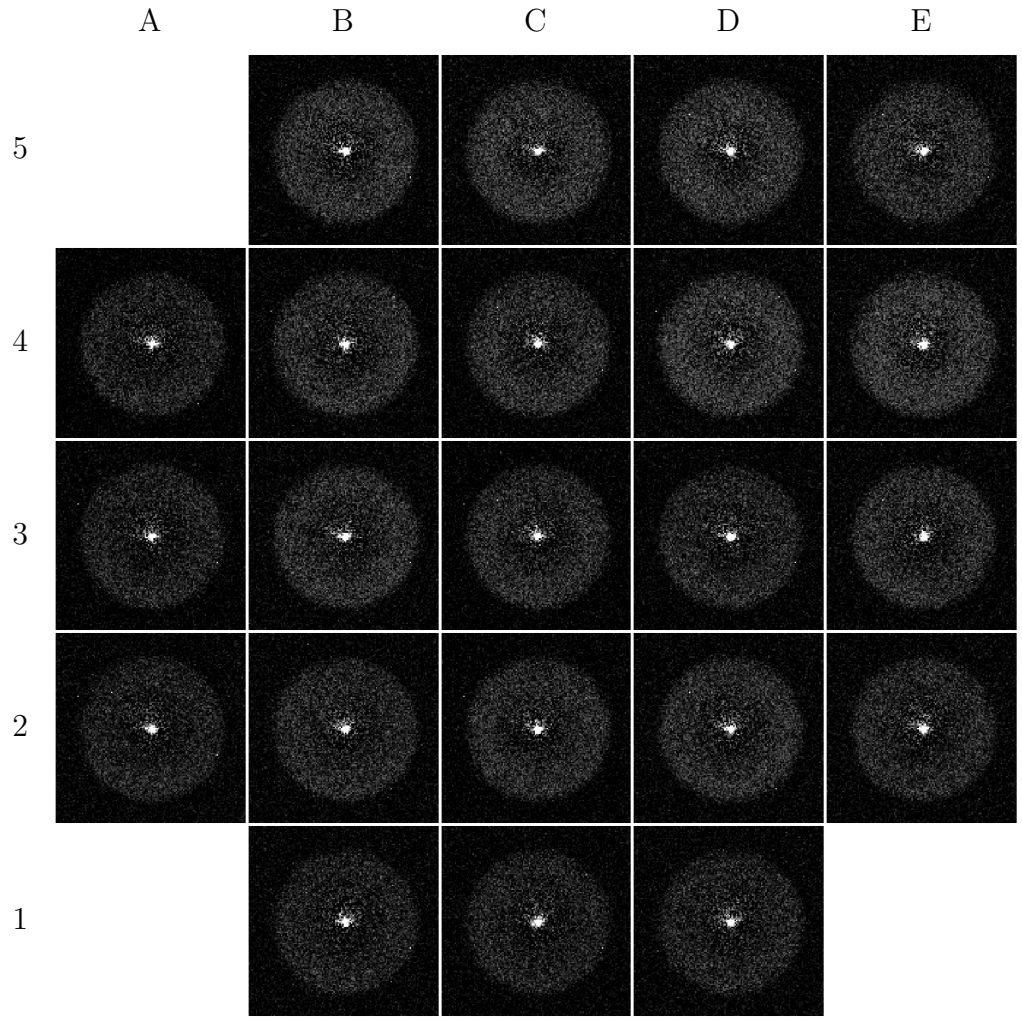

Table 4.3: Mönch diffraction efficiency maps of sample VY181015a "mark".

	A	B	C	D	E
5		0.76	0.72	0.83	0.80
4	0.65	0.69	0.78	0.79	0.79
3	0.54	0.65	0.69	0.70	0.65
2	0.51	0.60	0.66	0.63	0.60
1		0.53	0.54	0.57	

(a) ZP heights in μm.

	A	B	C	D	E
5		18.5	16.9	20.6	19.8
4	14.6	16.0	19.2	19.5	19.4
3	10.8	14.5	15.9	16.2	14.7
2	9.8	12.9	15.0	13.8	12.9
1		10.5	10.8	12.0	

(b) Corresponding max. theoretical diffraction efficiencies in percent.

	A	B	C	D	E
5		3.1	3.2	3.3	2.9
4	2.7	3.0	3.1	3.5	3.4
3	2.3	2.8	2.9	2.7	2.8
2	2.0	2.5	2.9	2.7	2.3
1		2.1	2.1	2.2	

(c) Measured ZP efficiencies in percent.

Table 4.4: ZP characteristics: VY181015a "mark"

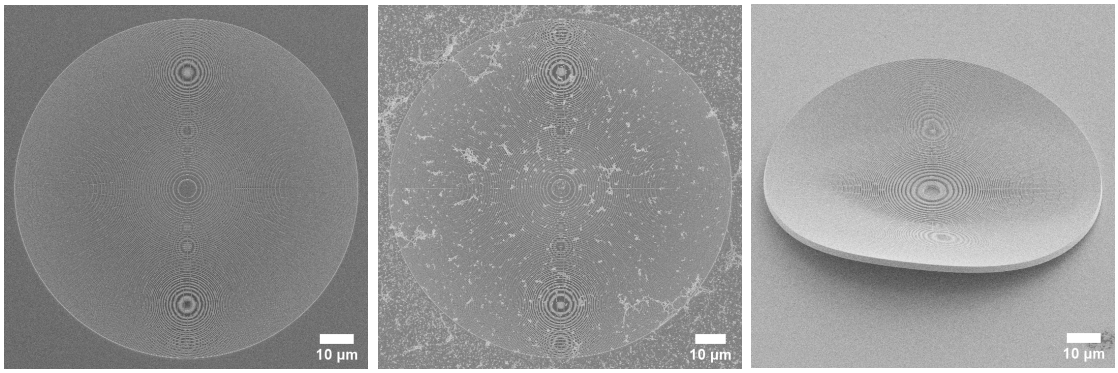

(a) ZP D5 on sample VY180821a "no mark"

(b) ZP C3 on sample VY181015a "mark"

(c) ZP A2, frontside of sample VY180821a "no mark"

Figure 4.11: SEM images illustrating (a) good structure quality, (b) good structure quality but with problematic resist residues and (c) zone plate delamination.

4.4 Double-sided Fresnel zone plates

The zone plates on the samples VY180821a "no mark" and VY181015a "mark" were made double-sided and measured once more in the X-ray-tube-based setup. The same zone plate layout was used on the frontside as in Figure 4.10, giving two single-sided and twenty-one double-sided zone plates on the resulting samples due to the flipping of the chip after the backside fabrication. The results are presented below.

4.4.1 Sample VY180821a "no mark" – double-sided

Table 4.5 shows the results from imaging sample VY180821a "no mark" with double-sided zone plates in the X-ray-tube-based setup. Almost all zone plates show curved Moiré fringes, indicating not only misalignment but also a difference in size between the front- and backside zone plates, see Section 2.1.4. The zone plates A5 and E5 are single-sided and naturally do not show any Moiré patterns. The features in the map of zone plate A2 are explained by the delamination of the structure, shown in Figure 4.11c – this is quite usual for zone plates of such extreme heights. The same problem can be seen in zone plate B4. That these issues are visible in the diffraction efficiency maps is expected but nevertheless important.

The heights in Table 4.6a are reaching numbers which are far past the optimal height for the X-ray energy of 8.4 keV (see Figure 2.3). This explains why some of the theoretical maximum diffraction efficiencies in Table 4.6b are even lower than for the corresponding single-sided zone plates.

The average measured efficiencies in Table 4.6c are around 4%, not much higher than the efficiencies in Table 4.2c for the corresponding single-sided zone plates. For the extremely high zone plates such as A4, A3 and A2 this is no surprise, since they are too high to be efficient at this X-ray energy. But for zone plates such as C5 with a reasonable height, with a theoretical efficiency which is around double of the corresponding single-sided zone plate theoretical efficiency, the measured efficiency is lower than expected. The reason is clearly indicated by the strong Moiré patterns –

the only case in which the efficiency is about the double of what was measured for the single-sided structure is the comparatively well-aligned zone plate D5.

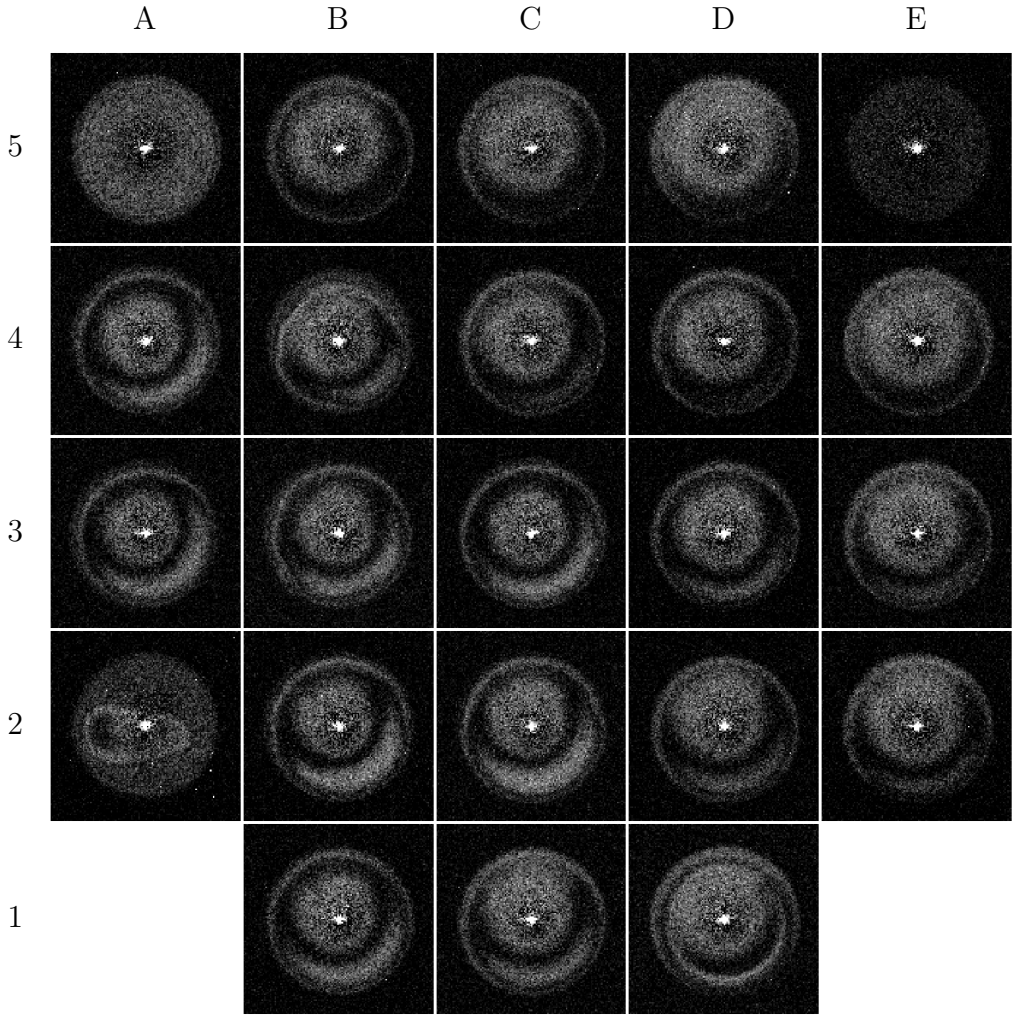

Table 4.5: Mönch diffraction efficiency maps of sample VY180821a "no mark", double-sided.

	A	B	C	D	E
5	1.62	2.13	1.96	1.85	0.53
4	2.57	2.80	2.33	2.19	2.04
3	2.88	2.65	2.58	2.36	2.16
2	3.31	2.65	2.54	2.30	2.13
1		2.48	2.33	2.16	

(a) ZP heights in μm.

	A	B	C	D	E
5	30.0	17.7	22.5	25.6	10.5
4	5.8	2.4	11.6	15.8	20.4
3	2.0	4.3	5.7	10.9	16.5
2	4.8	4.3	6.4	12.6	17.5
1		7.7	11.6	16.8	

(b) Corresponding max. theoretical diffraction efficiencies in percent.

	A	B	C	D	E
5	5.3	4.3	4.3	5.2	2.1
4	3.9	4.1	4.0	4.0	4.7
3	3.8	3.9	3.9	4.0	4.3
2	3.9	4.5	4.5	4.1	4.4
1		4.1	4.3	4.8	

(c) Measured ZP efficiencies in percent.

Table 4.6: ZP characteristics: VY180821a "no mark", double-sided.

In some cases, the measured efficiency is higher than the theoretical maximum efficiency. This again has to do with the strong misalignments in the double-sided structures, leading to only a part of the measured total height contributing to the diffraction, giving a slightly better efficiency than expected for the total, "too high" structure.

Almost all of the zone plate efficiency maps show a concentric circle close to the periphery, which when following the Moiré fringes indicates an inversion of the fringe pattern. This might indicate a large tilting of the outer zones in one of the zone plate halves – this would correspond well to a size difference between the two zone plate halves in the outer parts of the double-sided structures.

4.4.2 Sample VY181015a "mark" – double-sided

Table 4.7 shows the diffraction efficiency maps of sample VY181015a "mark". The sample was made through hot development on both the back- and the frontside. Zone plates A5 and E5 are single-sided. Due to the large amount of residues on the backside structures, see Figure 4.11b, the marker search for the frontside zone plates was very poor. This lead to bad alignment between the front- and backside structures which can clearly be seen in the efficiency maps. Due to the residues left in the backside fabrication, the frontside was flushed with 30% more water in the development in order to prevent the same issues. The resulting structures had no resist residues.

All diffraction efficiency maps for this sample seem less bright than the ones in Table 4.5 made of the sample VY180821a "no mark", indicating a lower efficiency. This is confirmed by the measured efficiencies in Table 4.8c. This might be seen as an indicator that hot development as it is done in this thesis does not give better results compared to a standard development procedure at room temperature.

Just as for sample VY180821a "no mark", comparing the efficiencies of the double-sided zone plates on VY181015a "mark" with the ones measured for the single-sided zone plates on the same chip yields that they are almost equal, even though the theoretical efficiencies for the double-sided structures are in most cases much higher. This, together with the clear alignment- and scaling issues visible through the Moiré fringes, indicates large issues in the fabrication.

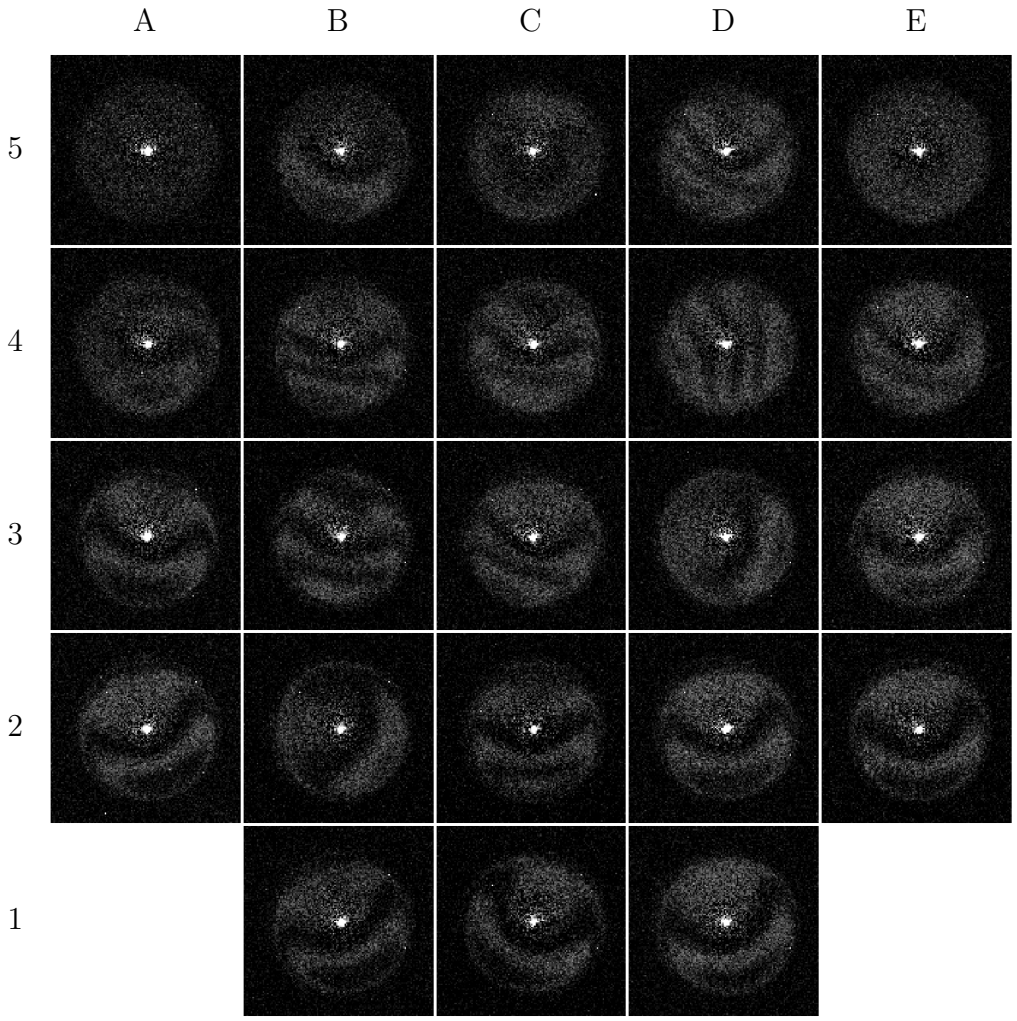

Table 4.7: Mönch diffraction efficiency maps of sample VY181015a "mark", double-sided.

	A	B	C	D	E
5	1.29	2.14	2.12	2.21	0.80
4	2.41	2.06	2.19	2.20	2.18
3	1.89	2.02	2.11	2.10	2.04
2	1.83	1.95	2.05	2.02	1.96
1		1.85	1.89	1.90	

(a) ZP heights in μm.

	A	B	C	D	E
5	31.0	17.2	17.8	15.0	19.8
4	9.5	19.8	15.7	15.5	16.1
3	24.5	20.7	18.2	18.5	20.3
2	26.0	22.9	20.0	20.8	22.6
1		25.4	24.5	24.2	

(b) Corresponding max. theoretical diffraction efficiencies in percent.

	A	B	C	D	E
5	1.9	2.3	2.4	3.0	3.0
4	2.4	2.6	2.8	3.0	3.1
3	2.4	2.7	2.9	2.8	3.0
2	2.6	2.5	2.7	2.8	2.9
1		2.4	2.6	2.8	

(c) Measured ZP efficiencies in percent.

Table 4.8: ZP characteristics: VY181015a "mark", double-sided.

4.4.3 Sample FK180131a – double-sided

Sample FK180131a was fabricated by Frieder Koch, another member of the *X-ray Optics and Applications group*; the fabrication parameters were the same as the ones presented in this thesis. The results are presented in Tables 4.9 and 4.10.

In this sample, the total structure heights on the back and frontside are lower than on the two samples presented in the previous sections. The alignment seems to be good for several of the zone plates, and the corresponding efficiencies in Table 4.10c are quite high. There are nevertheless several zone plates, positioned in the right part of the chip, which have strong concentric Moiré fringes. These fringes suggest that the alignment is good but that there is a substantial size difference, corresponding to about 50 nm (one zone width), between the zone plates on the two sides of the membrane. Zone plates E5 and A5 are single-sided which is why they show no Moiré fringe patterns. The fact that the alignment seems to be very good for some zone plates on this chip compared to the samples VY180821a "no mark" and VY181015a "mark" indicates that the problems might be structure height-related. A further investigation is described in Section 4.4.5.

One can conclude that the measurements with the X-ray-tube-based setup provide important insights into not only the efficiency of different parts of double- and single-sided zone plates, but also into fabrication- and alignment issues.

4.4.4 Comparison with measurements at the ANATOMIX beamline of Synchrotron SOLEIL

In order to confirm the reliability of the efficiency measurements at the X-ray tube, Frieder Koch performed measurements of the zone plate diffraction efficiency on sample FK180131a at the ANATOMIX beamline of SOLEIL. The approximate X-ray energy was 10 keV. The results can be seen in Tables 4.11 and 4.12. The pixel size of the detector was 9 μm and the diameter of the zone plates on the images corresponds to approximately 570 pixels. The presented diffraction efficiency maps have all been normalized to a scale from 0 to 3400 photon counts. The ANATOMIX images are in other words two orders of magnitude brighter than the Mönch images, easily explained by the much higher flux at the synchrotron compared to the X-ray tube. Correspondingly, the pictures are much better resolved and one can even see regular concentric patterns reflecting the support structures patterned between the zone plate zones.

When comparing the X-ray tube images in Table 4.9 with the images from ANATOMIX, one can clearly conclude that the information given by the former corresponds to what can be read out from the latter. This is a very important result, showing that the X-ray tube setup can be used for diffraction efficiency mapping, giving the same results that would have been obtained at a synchrotron. Of course, the resolution in the images is not as high and the integration time needed to make such images is longer – two times [10]minutes compared to only 2 seconds for the measurements at the beamline – but the information obtained is essentially the same. This serves as a great characterization method in the continuous process of developing this type of optics. By adding another 10 minutes per image at the X-ray

tube, the image quality and therefore the similarity increased, as can be seen in Figure 4.12.

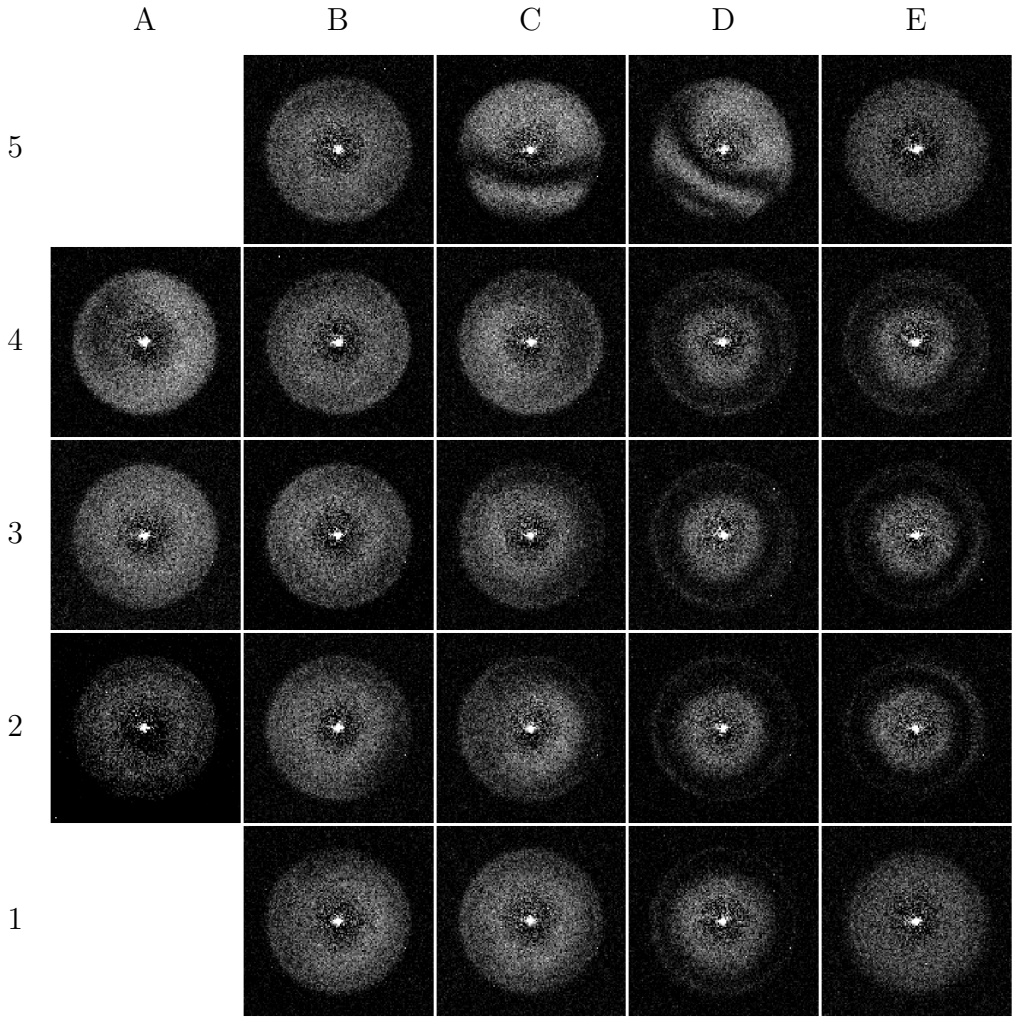

Table 4.9: Mönch diffraction efficiency maps of sample FK180131a, double-sided.

	A	B	C	D	E
5		1.38	1.24	1.81	1.47
4	1.37	1.54	1.58	1.99	2.12
3	1.28	1.53	1.65	2.12	2.12
2	1.30	1.49	1.62	2.13	2.09
1		1.66	1.76	2.12	1.10

(a) ZP heights in μm.

	A	B	C	D	E
5		31.5	30.5	26.5	31.4
4	31.5	31.0	30.6	21.8	17.8
3	30.9	31.1	29.7	17.8	17.8
2	31.1	31.3	30.0	17.6	18.7
1		29.5	27.6	17.8	28.2

(b) Corresponding max. theoretical diffraction efficiencies in percent.

	A	B	C	D	E
5		5.2	6.1	5.3	4.4
4	6.7	5.6	5.2	3.0	2.8
3	5.8	5.9	4.4	2.7	2.5
2	5.7	5.0	4.3	2.7	2.6
1		5.2	5.1	3.3	4.0

(c) Measured ZP efficiencies in percent.

Table 4.10: ZP characteristics: FK180131a, double-sided.

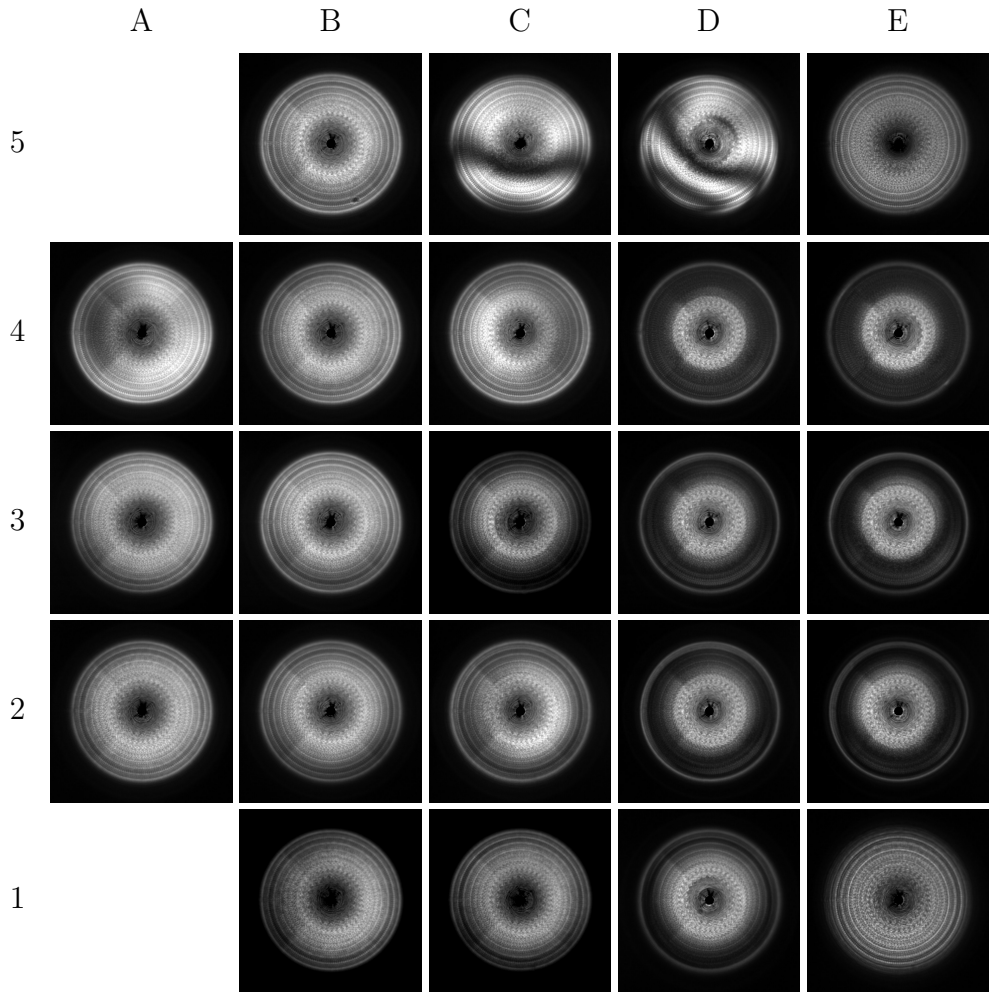

Table 4.11: Diffraction efficiency maps of sample FK180131a, double-sided, measured at the ANATOMIX beamline of Synchrotron SOLEIL.

	A	B	C	D	E
5		9.4	9.5	8.5	6.6
4	10.0	9.1	9.2	5.3	5.0
3	9.0	9.2	7.2	5.1	4.7
2	8.7	7.9	7.8	5.1	4.5
1		8.5	8.2	5.6	6.6

Table 4.12: ZP diffraction efficiencies of sample FK180131a, double-sided, measured at the ANATOMIX beamline of Synchrotron SOLEIL.

The efficiency values measured at ANATOMIX are all higher than the ones measured with the X-ray tube-setup. An explanation could be that for these zone plate heights, the efficiencies should also be higher for this higher X-ray energy, from looking at the corresponding two curves in Figure 2.3. But this explanation applies only to the zone plates higher than approximately 1500 nm, which is only a fraction of the zone plates measured.

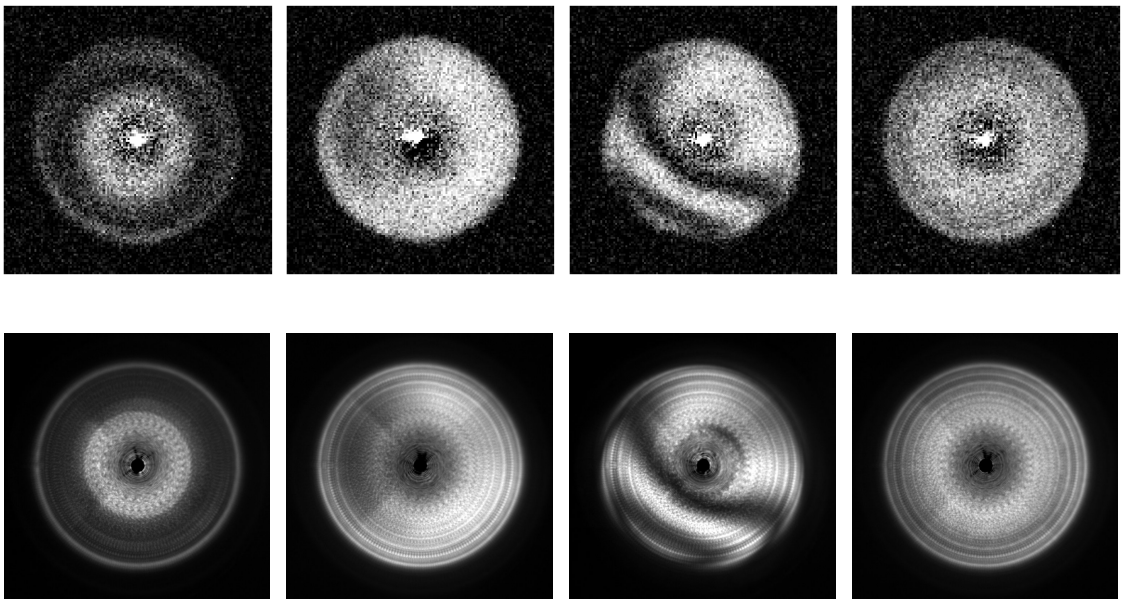

(a) D4 **(b)** A4 **(c)** D5 **(d)** B4

Figure 4.12: A comparison between the diffraction efficiency maps recorded with the Mönch at the X-ray tube setup (top row) and at the ANATOMIX beamline of Synchrotron SOLEIL (bottom row) for four zone plates from sample FK180131a. In the ANATOMIX images, the zeroth-order photons going through the pinhole have been subtracted from the image, which is why there is a bright spot in the center of the Mönch images but not in the ANATOMIX images.

There are several other possible reasons for the difference in measured efficiencies. First of all, the efficiencies were determined in different ways. At ANATOMIX, the photon detection was made with a scintillator-coupled PCO camera and the efficiency determination was image-based, just as what was initially intended with the Mönch detector. In this thesis the efficiencies were in the end determined using a PMT. However, even if an efficiency determination would have been possible with the Mönch, it would still have yielded some differences due to it being a direct-conversion detector. The PCO camera, which used for alignment in this thesis, could not have been used for diffraction efficiency measurements due to the low flux from the X-ray tube and low detection yield of the scintillator-coupled system.

Another possible reason for the different efficiencies are the differences in the sources. At a synchrotron, the source is far away from the focusing zone plate, leading to a diffraction-limited spot size, while at the X-ray tube with the very small distances involved, the spot size is limited by the source size. This generally leads to a much larger spot size. The smaller source and parallel illumination used at a synchrotron beamline also contributes to the higher spot quality used in the measurements. Furthermore, the monochromaticity at a beamline is much higher than at the X-ray tube, where a broad part of the X-ray spectrum of the anode material emerges from the source even when it is filtered. Finally, the measurements were done at different X-ray energies which makes a comparison difficult even with a theoretical knowledge of how the zone plate efficiency depends on the energy. Ideally, the measurements at ANATOMIX should have been done at the same X-ray

energy of 8.4 keV as the X-ray tube, but this was not possible at the time of the measurements.

A final factor to consider is that the incoming illumination at ANATOMIX was most probably underestimated. For the diffraction efficiency maps of the zone plates an integration time of 2 seconds was used, while for the reference image where the incoming flux recorded, the integration time had to be decreased to 5 ms due to the high flux otherwise saturating the detector. The resulting counts were proportionally increased for the calculation of the efficiency, but the more reliable way would have been to use the exact same integration for the zone plate images and for the reference. To conclude, it is difficult to say why the efficiencies measured at SOLEIL were higher than the ones measured at the X-ray tube, but it is clear that the values should not be compared directly due to the large differences in sources, energies, and efficiency measurement methods.

4.4.5 Investigation of Moiré fringe origins

The strong Moiré fringes visible for all of the fabricated double-sided zone plates indicate an issue with the alignment. Questions that appear are where the origin for the issues lies, if it is mainly in the alignment step or if it also has to do with the fabrication, and if these problems can be precompensated by changing something in the fabrication. These issues need to be solved, because with them the efficiency in general does not increase when making single-sided zone plates double-sided, meaning that it might simply not be worth the effort of making the two-step fabrication.

In samples VY180821a "no mark" and VY181015a "mark", there are strong Moiré fringes for all of the zone plates. The results for sample FK180131a show a much better alignment, and have a clear division between zone plates with almost no issues and zone plates with concentric Moiré fringes. Since the fabrication was the same for all of the samples (with exception for sample VY181015a "mark" which was made through hot development), the existence of these different cases suggests that the origin might be in the heights of the zone plates – a factor that is different for every single zone plate even when using the same fabrication parameters. The total heights of the double-sided structures have already been presented for the three samples; Table 4.13, 4.14 and 4.15 now show a comparison between the zone plate heights on the back- and on the frontside.

The backside heights are similar for all three samples, all ranging between approximately 0.4 μm and 0.8 μm with most of the zone plates being around 0.6-0.7 μm. The frontside heights, however, differ: sample VY180821a "no mark" presents heights up to more than 2 μm, sample VY181015a "mark" more moderate heights around 1.4 μm, and sample FK180131a even lower heights down to 0.7 μm. Remembering that the alignment was in general much better (with fewer Moiré fringes) on sample FK180131a, this is an indicator that lower heights seem to give better results compared to higher structures. Another strong indicator for the same conclusion is that the zone plates in the two rightmost columns on sample FK180131a are much higher than the rest of the zone plates on that chip, and are the exact zone plates that have scaling issues. The misalignment issues of the zone plate C5, which does not have very high frontside structures, can be explained by the same theory since

it has a large difference in height between the back- and the frontside just as the zone plates in columns D and E. That the alignment- and scaling issues are stronger in VY180821a ”no mark” and VY181015a ”mark” might then be explained by the much higher frontside heights that those samples have compared to the backside.

	A	B	C	D	E
5		0.56	0.57	0.54	0.53
4	0.62	0.67	0.65	0.64	0.63
3	0.66	0.72	0.73	0.70	0.65
2	0.71	0.77	0.78	0.73	0.69
1		0.80	0.80	0.77	

(a) ZP heights in μm, on backside

	A	B	C	D	E
5	1.62	1.56	1.39	1.30	
4	1.95	2.14	1.69	1.55	1.40
3	2.22	1.93	1.85	1.66	1.52
2	2.60	1.88	1.76	1.56	1.44
1		1.68	1.53	1.38	

(b) ZP heights in μm, on frontside

Table 4.13: ZP heights on back- and frontside: VY180821a ”no mark”, double-sided.

	A	B	C	D	E
5		0.76	0.72	0.83	0.80
4	0.65	0.69	0.78	0.79	0.79
3	0.54	0.65	0.69	0.70	0.65
2	0.51	0.60	0.66	0.63	0.60
1		0.53	0.54	0.57	

(a) ZP heights in μm, on backside

	A	B	C	D	E
5	1.29	1.38	1.40	1.39	
4	1.76	1.37	1.41	1.40	1.39
3	1.35	1.38	1.42	1.40	1.39
2	1.32	1.35	1.39	1.39	1.36
1		1.32	1.35	1.33	

(b) ZP heights in μm, on frontside

Table 4.14: ZP heights on back- and frontside: VY181015a ”mark”, double-sided.

	A	B	C	D	E
5		0.50	0.37	0.49	
4	0.50	0.60	0.57	0.60	0.52
3	0.48	0.61	0.65	0.64	0.60
2	0.60	0.67	0.71	0.72	0.70
1		0.73	0.79	0.82	

(a) ZP heights in μm, on backside

	A	B	C	D	E
5		0.88	0.88	1.32	1.47
4	0.87	0.94	1.01	1.39	1.60
3	0.80	0.92	1.00	1.49	1.52
2	0.71	0.82	0.92	1.41	1.40
1		0.92	0.98	1.31	1.10

(b) ZP heights in μm, on frontside

Table 4.15: ZP heights on back- and frontside: FK180131a, double-sided.

4.4.5.1 Design of Moiré test patterns

The trend where more Moiré fringes appear for a larger height difference between the zone plates on the frontside and the ones on the backside was investigated further by the fabrication and measurement of two test samples with similar backside zone plate heights and different frontside heights: sample VY181113a with very high frontside structures compared to the backside, and sample VY181113b with frontside structures of heights close to the backside heights. The back- and frontside heights of the two samples are presented in Tables 4.16 and 4.17.

	ii			i		
	A	B	C	A	B	C
3	0.59	0.59	0.60	0.60	0.57	0.54
2	0.56	0.57	0.58	0.56	0.57	0.54
1	0.56	0.58	0.55	0.54	0.56	0.54

	iv			iii		
	A	B	C	A	B	C
3	0.53	0.53	0.54	0.54	0.54	0.52
2	0.50	0.50	0.51	0.53	0.51	0.51
1	0.45	0.45	0.45	0.44	0.45	0.45

(a) ZP heights in μm, on backside.

	ii			i		
	A	B	C	A	B	C
3	1.42	1.06	1.06	1.02	1.35	1.55
2	1.48	1.28	1.21	1.23	1.57	1.59
1	1.33	0.94	0.94	0.93	1.41	1.33

	iv			iii		
	A	B	C	A	B	C
3	1.29	0.90	0.91	0.91	1.18	1.04
2	1.26	0.89	0.89	0.89	1.15	1.02
1	1.72	1.35	1.35	1.38	1.53	1.18

(b) ZP heights in μm, on frontside.

Table 4.16: ZP heights on back- and frontside: VY181113a "mark", double-sided – first Moiré test.

	ii			i		
	A	B	C	A	B	C
3	0.45	0.44	0.44	0.43	0.44	0.44
2	0.48	0.49	0.48	0.47	0.49	0.50
1	0.50	0.50	0.50	0.50	0.51	0.51

	iv			iii		
	A	B	C	A	B	C
3	0.52	0.53	0.54	0.54	0.54	0.54
2	0.52	0.55	0.54	0.55	0.55	0.54
1	0.55	0.56	0.56	0.57	0.57	0.57

(a) ZP heights in μm, on backside.

	ii			i		
	A	B	C	A	B	C
3	0.75	0.75	0.78	0.81	0.81	0.80
2	0.73	0.74	0.76	0.76	0.76	0.76
1	0.75	0.74	0.76	0.74	0.75	0.76

	iv			iii		
	A	B	C	A	B	C
3	0.69	0.70	0.74	0.76	0.74	0.75
2	0.94		0.69	0.74	0.74	0.75
1	0.67	0.77	0.72	0.75	0.76	0.76

(b) ZP heights in μm, on frontside.

Table 4.17: ZP heights on back- and frontside: VY181113b "no mark", double-sided – second Moiré test. The frontside exposure of zone plate ivB2 failed due to a residue on the membrane, which is why no frontside height is given.

The backside HSQ spin coating was done at 2500 rpm for both samples; a high angular rotation speed was chosen to get a more homogeneous HSQ layer thickness and less variations in the zone plate heights. For sample VY181113a the spin coating on the frontside was done at 1500 rpm; for sample VY181113b at 2500 rpm.

In the test samples, a way of compensating the offsets and scaling issues appearing during the fabrication was investigated. On each chip, several zone plate arrays were patterned where each array consisted of different combinations of offsets and zone plate sizes. All of the backside zone plates were fabricated with a diameter of 100 μm and equally spaced positions within the arrays. The frontside zone plates were fabricated with a diameter either equal to or 0.5% smaller or larger compared to the backside zone plates, and with offsets to the backside zone plates of either 0 nm, 100 nm or 200 nm, made in both the x- and the y direction. The latter two offsets were chosen to correspond to offsets of one and two pitches, respectively. The results are presented below.

4.4.5.2 Results

Tables 4.18 and 4.19 show the results from and characteristics of sample VY181113a with a *large* height difference between the front- and backside. What can be seen is that the best cases, with the least amount of Moiré fringes, are actually the cases A2 in all four arrays, corresponding to no intentional offsets or scalings. Out of the mentioned four cases, however, only iiiA4 presents a good alignment with a corresponding high diffraction efficiency. For the other three cases the alignment issues seem to be more or less random, showing the difficulty in guaranteeing a good alignment.

The many fringes appearing for the different offsets indicate that the offsets are too large to compensate for the misalignments appearing in the fabrication. The number of fringes increase with the offset, which is expected. The direction in which they increase is coinciding with the diagonal along which the offsets were made, which is also expected. By counting the number of Moiré fringes in arrays in column A – in array ii, there are two in A3, one in A2 in the opposite direction, and three in A1 in the same direction as A2, and seeing that this trend is repeated in all of the four arrays, one can conclude that out of the three cases, no size difference between the back- and frontside zone plate as in A2 works the best, but that that the optimal case would be between the cases A2 and A3, with the backside being 0.2% larger than the frontside (determined through a simple interpolation of the number of fringes). Another test sample could have been made, testing different scalings of the frontside zone plate to find the optimal case, but was not done due to the time limitation.

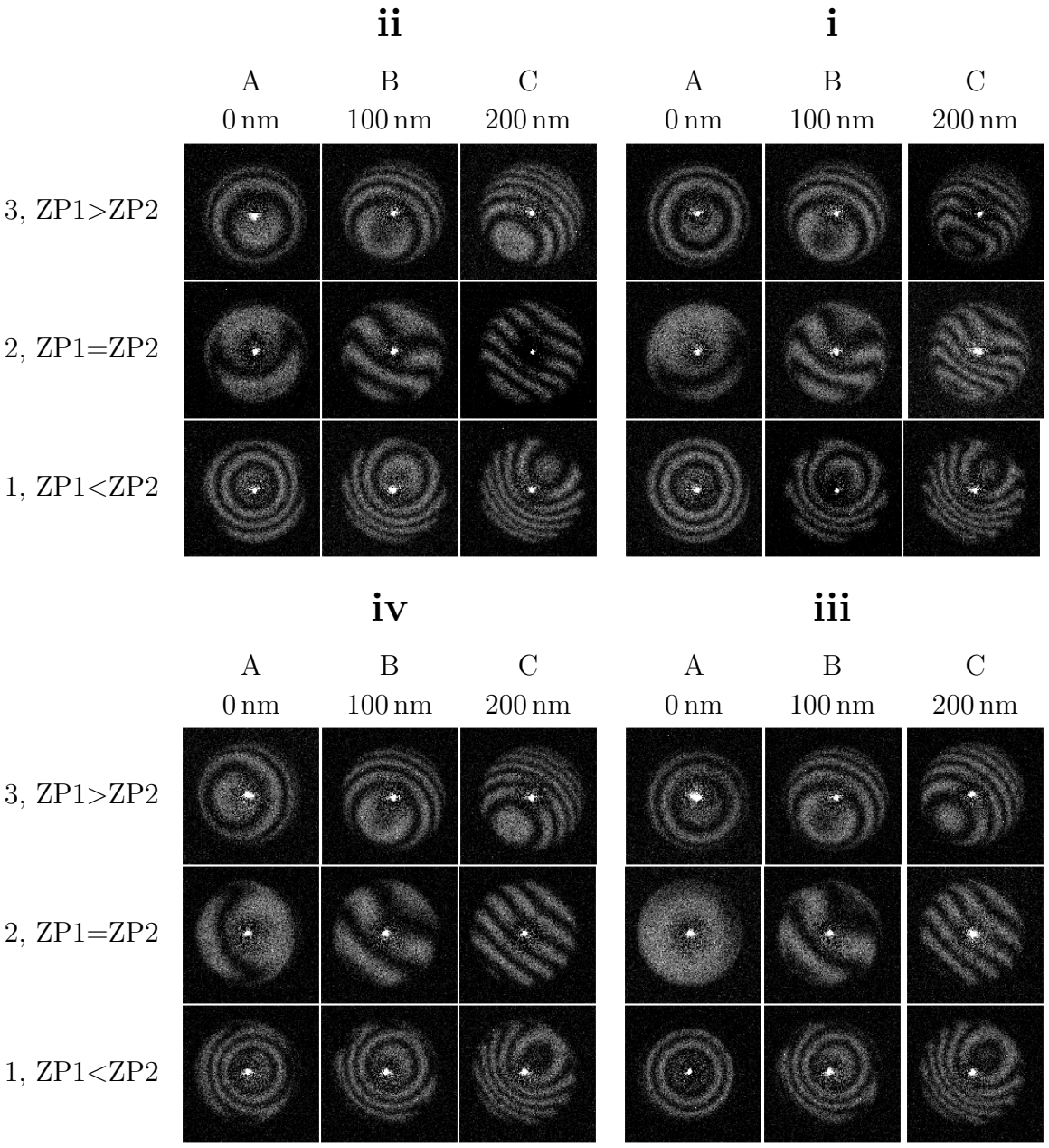

Table 4.18: Mönch diffraction efficiency maps of sample VY181113a, double-sided – Moiré test with a large height difference between the front- and the backside zone plates. The distances indicate the offsets made along both the x and y direction.

	ii			i		
	A	B	C	A	B	C
3	2.01	1.65	1.65	1.62	1.91	2.09
2	2.05	1.85	1.79	1.78	2.14	2.14
1	1.89	1.52	1.50	1.47	1.97	1.87

	iv			iii		
	A	B	C	A	B	C
3	1.82	1.42	1.45	1.45	1.72	1.57
2	1.76	1.39	1.40	1.41	1.66	1.53
1	2.18	1.80	1.80	1.82	1.98	1.63

(a) ZP heights in μm.

	ii			i		
	A	B	C	A	B	C
3	21.0	29.6	29.6	30.1	23.9	18.8
2	20.1	25.5	27.1	27.1	17.4	17.4
1	24.5	31.1	31.3	31.4	22.2	25.2

	iv			iii		
	A	B	C	A	B	C
3	26.4	31.5	31.5	31.5	28.5	30.7
2	27.7	31.5	31.5	31.5	29.5	31.0
1	16.2	26.9	26.7	26.3	22.0	29.9

(b) Corresponding max. theoretical diffraction efficiencies in percent.

	ii			i		
	A	B	C	A	B	C
3	3.9	4.3	4.3	4.0	4.2	3.4
2	4.6	4.1	4.2	4.7	3.9	3.8
1	4.2	4.2	4.0	4.3	4.1	3.7

	iv			iii		
	A	B	C	A	B	C
3	3.7	4.3	4.1	3.5	4.0	3.9
2	4.7	3.9	4.0	5.9	3.8	3.9
1	3.8	3.9	3.9	3.5	3.8	4.1

(c) Measured ZP efficiencies in percent.

Table 4.19: ZP characteristics: VY181113a "mark", double-sided – Moiré test with a large height difference between the front- and the backside zone plates.

Tables 4.20 and 4.21 show the results from sample VY181113b with a *small* height difference between the front- and backside. The alignment is in general much better than for sample VY181113a – there are several zone plates with good alignment (all corresponding to cases with no predefined offset or scaling), the Moiré fringes for the cases with no zone plate size difference are straight (row 2 in all of the arrays), and in all of the arrays except for iv the cases where only a size difference is made (column A) the Moiré fringes are concentric, just as would be expected for a perfect alignment and differently sized zone plates. The cases with both scalings and offsets in lines 1 and 3 also follow the expected trends well, with a clear Moiré fringe direction corresponding to the direction in which the offsets were made. The fact that A1 and A3 have the exact same Moiré patterns means that they are symmetric around A2 in terms of scaling, meaning that for these structure heights the best size difference between the back- and frontside zone plate to aim for is no size difference at all.

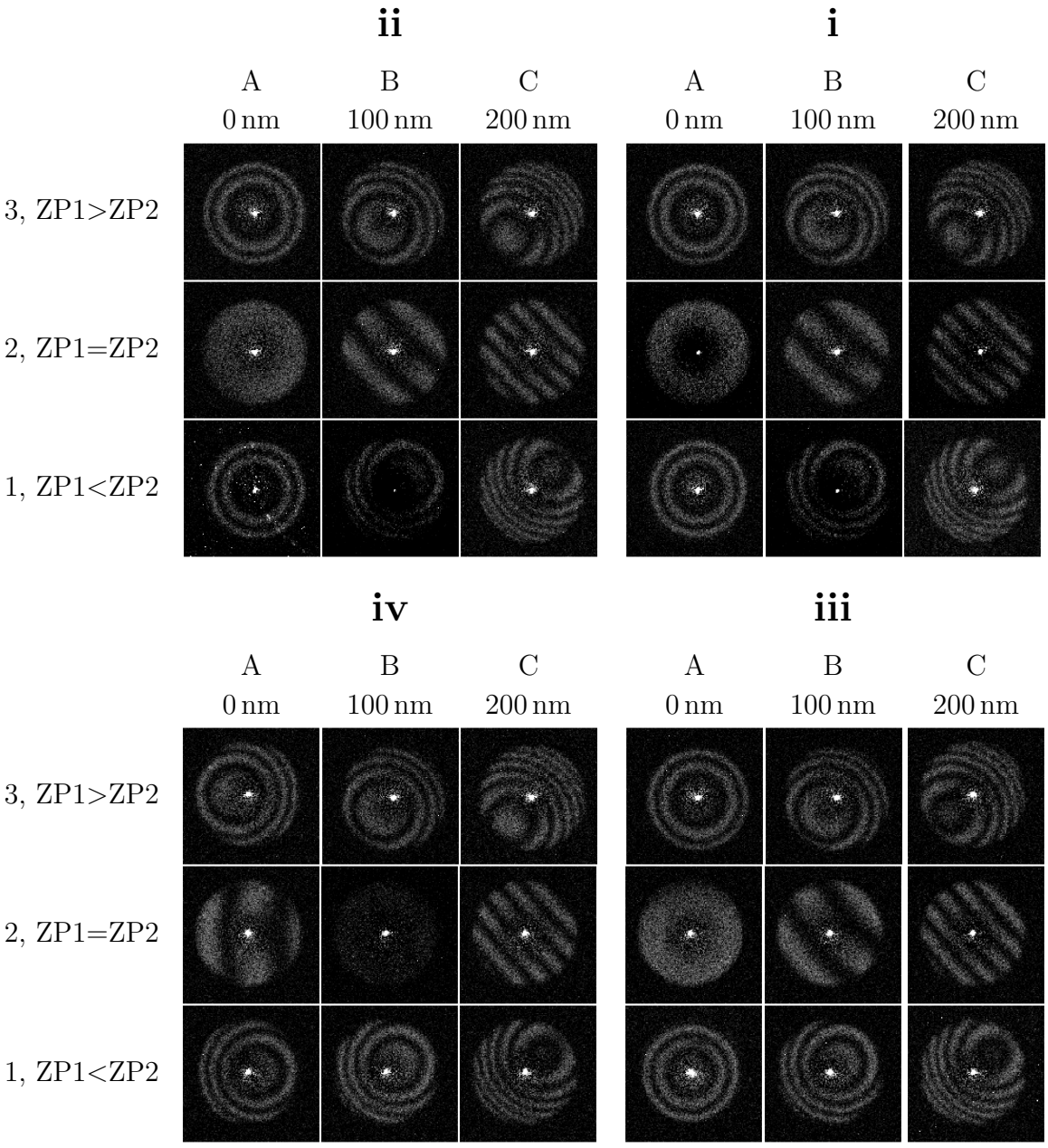

Table 4.20: Mönch diffraction efficiency maps of sample VY181113b, double-sided – Moiré test with a small height difference between the front- and the backside zone plates. The distances indicate the offsets made along both the x and y direction.

	ii			i		
	A	B	C	A	B	C
3	1.20	1.20	1.22	1.24	1.25	1.23
2	1.22	1.23	1.24	1.23	1.25	1.26
1	1.25	1.24	1.26	1.24	1.26	1.27

	iv			iii		
	A	B	C	A	B	C
3	1.21	1.23	1.28	1.29	1.28	1.28
2	1.46	0.55	1.24	1.30	1.29	1.29
1	1.22	1.33	1.29	1.32	1.32	1.33

(a) ZP heights in μm.

	ii			i		
	A	B	C	A	B	C
3	30.0	29.9	30.2	30.5	30.6	30.4
2	30.2	30.3	30.5	30.3	30.6	30.7
1	30.5	30.5	30.7	30.4	30.7	30.8

	iv			iii		
	A	B	C	A	B	C
3	30.1	30.3	30.9	31.0	30.9	30.9
2	31.4	11.2	30.4	31.0	31.0	31.0
1	30.2	31.3	31.0	31.2	31.2	31.3

(b) Corresponding max. theoretical diffraction efficiencies in percent.

	ii			i		
	A	B	C	A	B	C
3	2.6	2.8	2.8	2.7	2.7	2.7
2	4.2	2.8	2.7	4.6	2.8	2.8
1	2.9	2.9	2.7	2.7	3.1	2.6

	iv			iii		
	A	B	C	A	B	C
3	2.8	3.0	3.0	2.7	2.8	2.8
2	3.2	1.6	2.9	4.5	3.2	3.0
1	2.6	3.3	2.8	3.1	3.2	3.3

(c) Measured ZP efficiencies in percent.

Table 4.21: ZP characteristics: VY181113b "no mark", double-sided – Moiré test with a small height difference between the front- and the backside zone plates.

The measured efficiencies for this sample are in general lower than the ones measured for sample VY181113a, which is not surprising with regards to the slightly lower total structure heights. In this sample it was however easier to guarantee a good alignment, meaning that the overall efficiency over the chip would be similar when comparing the best cases from the two chips.

What can be concluded from this study is that it is clearly more difficult to guarantee a good alignment between the halves of a double-sided zone plate when the structure heights on the frontside are much higher than on the backside. When that is the case, one has to find ways to compensate for the scaling- and offset issues appearing, which is difficult since for every zone plate these typically vary. What is better to aim for in the nearest future, until these problems are solved, is a lower structure height on both sides.

The origins of these issues can be several. What is known is that the electron beam system rescales, offsets and rotates the pattern it makes on the frontside according to what distances and angles it measures between the three backside markers used for the alignment. The rotational degree of freedom is not an issue in our case of rotationally symmetric structures, but the fact that there are three markers overdetermines the problem and gives one scaling factor in x and one in y, in some cases probably leading even to slightly oval zone plates on the frontside. Depending on where the markers are found compared to what is expected by the system, there is also an offset, clearly seen in the efficiency maps of the zone plates made in this thesis. By checking the log files from the exposures, one can see that the distances found between the alignment markers before each frontside exposure is in general always smaller than expected from the programmed pattern, leading to the frontside zone plates being scaled down. Since the best case on the sample with a large height difference was found to be when the backside zone plate is made slightly larger than the frontside, this indicates that the distance between the backside alignment markers shrinks (possibly due to the tension in the membrane generated by the structures), and the frontside zone plate is made smaller than intended. The shrinking could occur in the HSQ structures after the development, but also during the deposition of Ir.

The alignment- and scaling issues need to be investigated further – this was not done in this thesis due to lack of time. The studies made here have however given important pieces of information – they have identified a problem which was not known before, and shown that for now the issues can be minimized by fabricating structures of lower, similar heights on both sides of the membranes.

4.4.6 Measurement of misalignment

A test pattern was designed to measure the misalignment between double-sided zone plate halves. Using the obtained knowledge that lower zone plate heights on both sides of the membrane lead to better alignment and fewer Moire fringes, a chip was made where a high angular rotation speed of 2500 rpm was used on both the backside and the frontside. Intentional offsets of 0 nm, 25 nm and 50 nm were made along two perpendicular directions in the plane of the zone plates to on the one hand try to compensate for the misalignment occurring in the fabrication process and on the other to make measurable misalignments for the tilting tests. In the resulting pattern, the offsets differed slightly from the design but were in the same order of magnitude, still being useful for the measurements. Table 4.22 shows an array on this test sample and Tables 4.23 and 4.24 its characteristics. Four out of the zone plates on this array were chosen for the misalignment measurements.

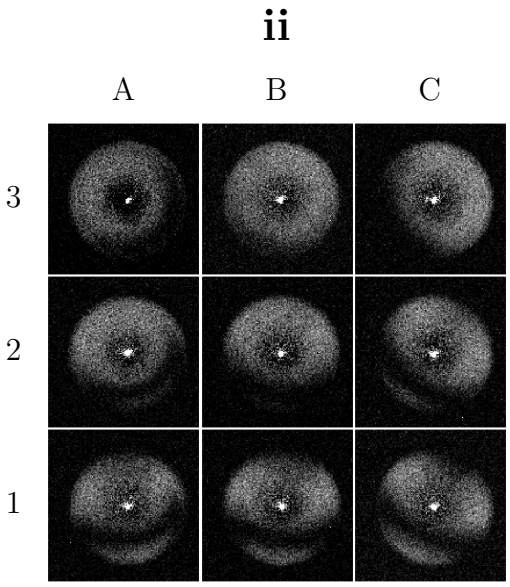

Table 4.22: Sample VY181119a – test sample for misalignment measurements. The zone plates iiA3, iiB3, iiC3 and iiC1 were chosen for the measurements.

ii

	A	B	C
3	1.52	1.42	1.43
2	1.50	1.43	1.41
1	1.42	1.40	1.39

(a) ZP heights in μm.

ii

	A	B	C
3	31.1	31.5	31.5
2	31.2	31.5	31.5
1	31.5	31.5	31.5

(b) Corresponding max. theoretical diffraction efficiencies in percent.

ii

	A	B	C
3	5.2	6.3	5.7
2	5.2	5.3	5.0
1	4.7	4.6	4.5

(c) Measured ZP efficiencies in percent.

Table 4.23: ZP characteristics: VY181119a, double-sided – test sample for misalignment measurements.

ii

	A	B	C
3	0.67	0.65	0.65
2	0.65	0.64	0.63
1	0.62	0.64	0.63

(a) ZP heights in μm, on backside.

ii

	A	B	C
3	0.86	0.78	0.78
2	0.86	0.79	0.77
1	0.80	0.76	0.76

(b) ZP heights in μm, on frontside.

Table 4.24: ZP heights on back- and frontside: sample VY181119a, double-sided – test sample for misalignment measurements.

In order to determine the misalignment in the double-sided zone plates along the x-direction, they were first rotated around the y-axis. An angle range of $-3°$ to $3°$ was chosen according to predictions made from the Moiré patterns visible in the

diffraction efficiency maps at no rotation and inserting known zone plate heights into (3.3) and (3.4). The resulting images are presented in Table 4.25; the corresponding efficiencies are plotted together with their uncertainties in Figure 4.13.

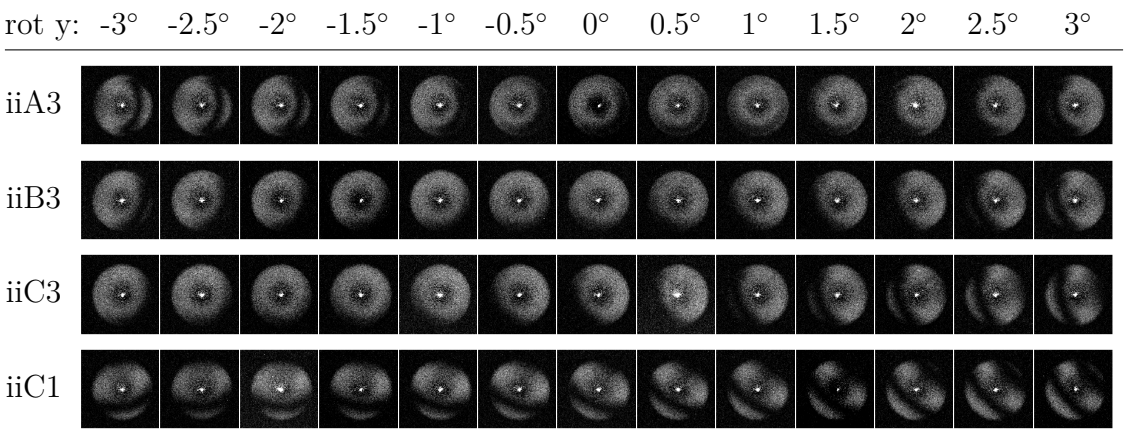

Table 4.25: Mönch diffraction efficiency maps recorded at different rotation angles around y.

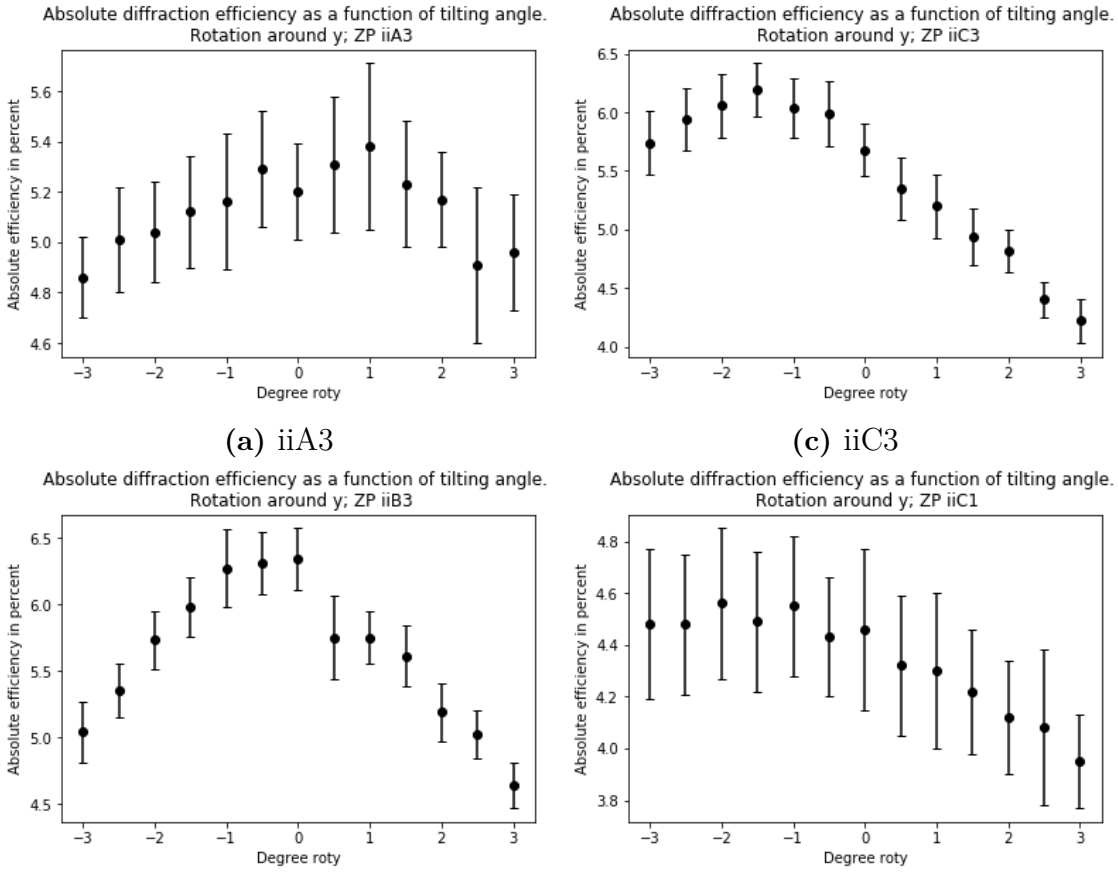

(a) iiA3 **(c)** iiC3

(b) iiB3 **(d)** iiC1

Figure 4.13: Absolute diffraction efficiencies as a function of tilting angle around y for four different zone plates. A maximum can be found in all curves, indicating an optimal tilting angle.

One can clearly see how the Moiré fringes slowly appear or disappear depending on what direction and how much a zone plate is rotated. For each zone plate there is an angle for which the fringes are visible the least, and a comparison with the efficiency curves in Figure 4.13 shows that the same angle also gives the best diffraction efficiency. Using the best tilting angle around y, the measured height of the zone plates and equations (3.3) and (3.4), one can easily calculate the offsets in the x-direction:

$$\text{iiA3 : rot y} = 1^\circ \longrightarrow l_{off,x} = 17.7\,\text{nm} \tag{4.1}$$
$$\text{iiB3 : rot y} = -0.5^\circ \longrightarrow l_{off,x} = -8.4\,\text{nm} \tag{4.2}$$
$$\text{iiC3 : rot y} = -1.5^\circ \longrightarrow l_{off,x} = -25.3\,\text{nm} \tag{4.3}$$
$$\text{iiC1 : rot y} = -2^\circ \longrightarrow l_{off,x} = -33.1\,\text{nm}. \tag{4.4}$$

In order to determine the offset along y, one instead needs to tilt the zone plates around the x-axis. Using the angles found to be the best in the tilting around y, the same four zone plates were therefore tilted in the other direction in a similar angle range. The results are presented in Table 4.26 and Figure 4.14. Just as for the other tilting direction, one can calculate the offsets:

$$\text{iiA3 : rot x} = -0.5^\circ \longrightarrow l_{off,y} = -8.8\,\text{nm} \tag{4.5}$$
$$\text{iiB3 : rot x} = -1^\circ \longrightarrow l_{off,y} = -16.8\,\text{nm} \tag{4.6}$$
$$\text{iiC3 : rot x} = -1^\circ \longrightarrow l_{off,y} = -16.8\,\text{nm} \tag{4.7}$$
$$\text{iiC1 : rot x} = -4^\circ \longrightarrow l_{off,y} = -66.2\,\text{nm}. \tag{4.8}$$

The calculated offsets in x and y correspond well to what one would expect from the images made without any tilt, presented in Table 4.22: zone plates iiA3 and iiC3, with approximately half a black fringe in x, are both offset about half a zone, i.e. 25 nm, in that direction, while zone plate iiB3 has even smaller offsets in both directions, which was also predictable from the already well-aligned initial state. Zone plate iiC1 shows almost a full fringe period in the y direction and has a reasonably large offset in the same direction. The sign of all of the offsets also corresponds well to what was expected from the initial states.

The offsets have been calculated assuming that the zone plates have been mounted perfectly perpendicular to the optical axis, i.e. that there was no initial inclination in the $roty = 0^\circ$ position. It has also been assumed that the height of a zone plate is constant over its range, using the approximate values measured in the SEM, and also that the structures are developed all the way to the membrane. With all of these factors, the calculated offsets are more of an approximation, but as mentioned they correspond well with what was expected.

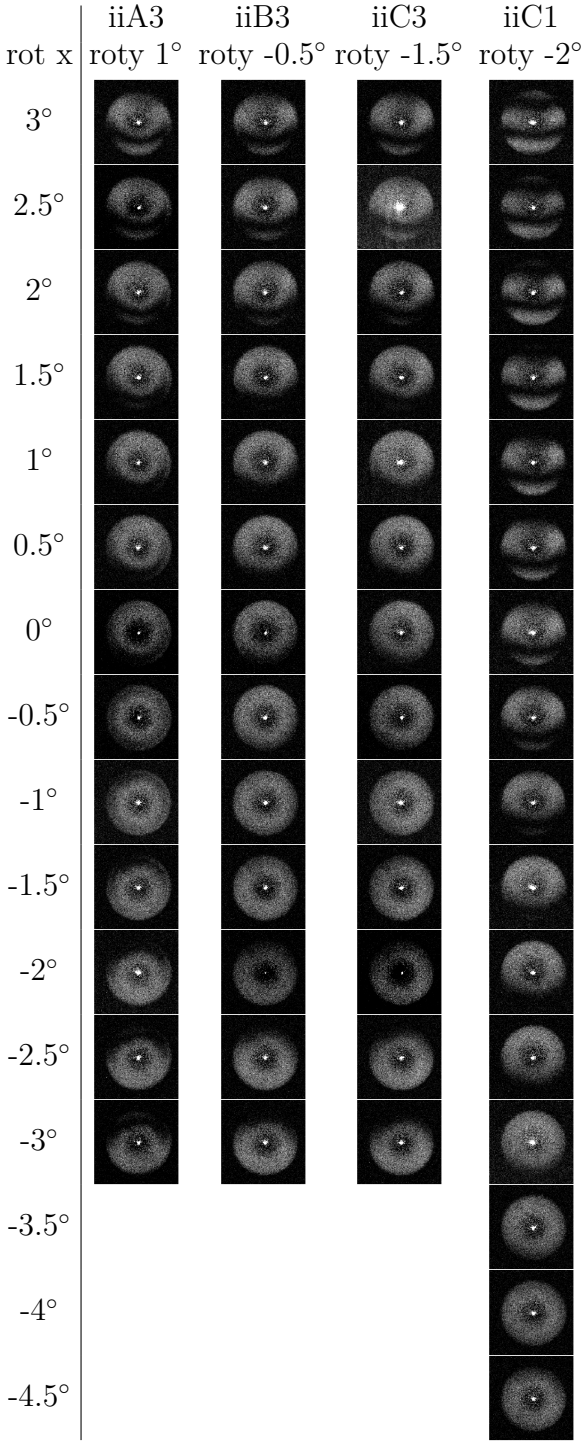

Table 4.26: Mönch diffraction efficiency maps recorded at different rotation angles around x, made at a specific rotation angle around y for each zone plate.

One can conclude that by tilting a double-sided zone plate it is clearly possible to determine the offset between its two halves. What is apparent is also the fact that by doing this one can increase the diffraction efficiency: the efficiency of zone plate iiA3 increased from 5.2% to 5.4% to 5.5% when compensating for the misalignment in x and in y; of zone plate iiB3 from 6.3% to 6.3% to 6.4%; of zone plate iiC3 from 5.7% to 6.2% to 6.4%; and of zone plate iiC1 from 4.5% to 4.6% to 5.9%. For an already well-aligned zone plate such as iiB3 the increase in efficiency was small, but for zone plates such as iiA3 and iiB3 with intermediate offsets the increase was larger, and for a misaligned zone plate such as iiC1 it was substantial. Another important detail is that a zone plate like iiC1 is not suitable for X-ray imaging applications due to the large misalignment, but the end result when having compensated for all misalignments is. The measurements performed here can of course be extended to other double-sided zone plates fabricated during this master's thesis or elsewhere.

To conclude, one can not only quantify the misalignments and increase the diffraction efficiency by tilting, but also make previously unusable zone plates usable for imaging. Another advantage is the fact that one can distinguish between issues in the fabrication and issues in the alignment. A dark region in a diffraction efficiency map could be indicating a fabrication problem such as undeveloped or destroyed zones or zones with a wrong Ir duty cycle, but could also be a Moiré fringe. The two cases will behave differently under tilting – the former will stay even when rotating the zone plate while the latter will change just as described in this section.

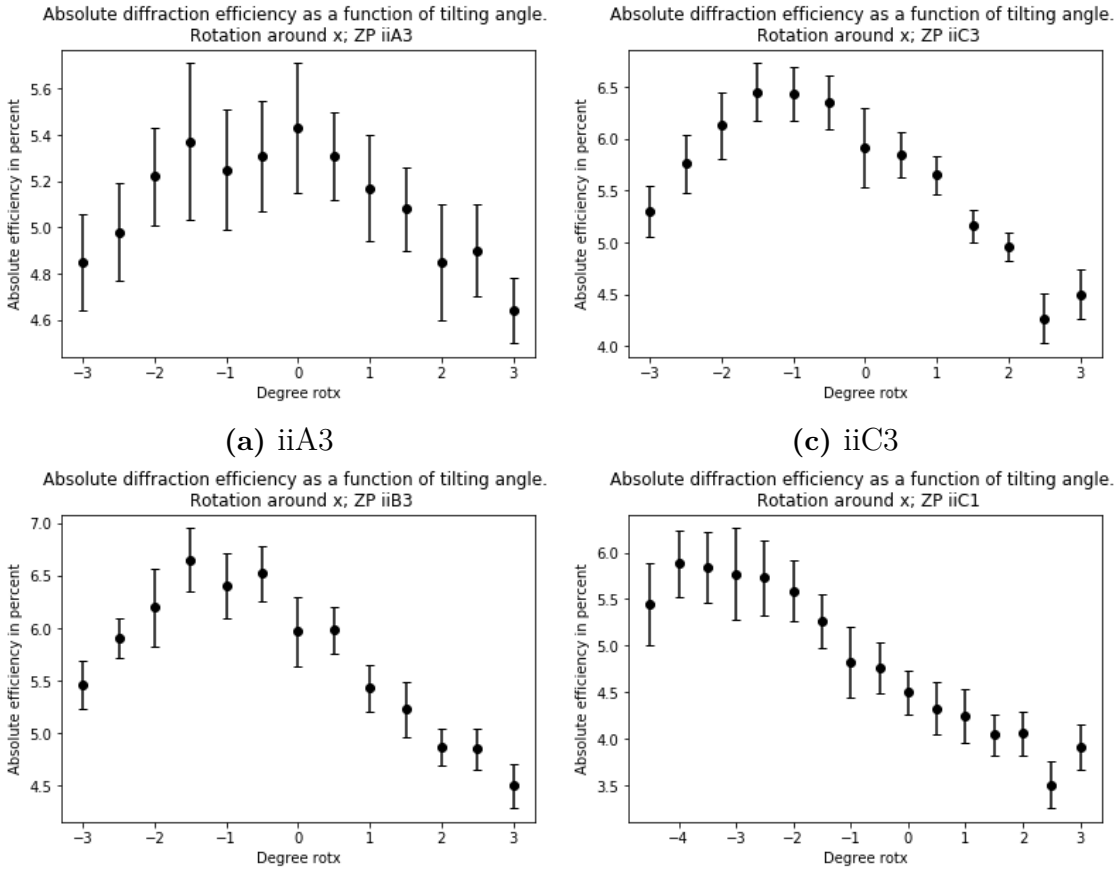

(a) iiA3 **(c)** iiC3

(b) iiB3 **(d)** iiC1

Figure 4.14: Absolute diffraction efficiencies as a function of tilting angle around x for four different zone plates. A slightly larger angle range was measured for ZP iiC1 in order to define the maximum. A maximum can be found in all curves, indicating an optimal tilting angle.

One can discuss how the tilting of a zone plate affects its function as a diffractive lens in an imaging application. As illustrated in Figure 4.15, one can see that for a tilted zone plate with a certain focal distance different parts of a sample will be imaged more or less focused compared to other parts. In other words, tilting of the zone plate will introduce astigmatism in the imaging. In a scanning transmission X-ray microscope this will lead to a decreased resolution in the imaging, since the focal spots will be separated along the optical axis due to the tilting. The beam can in that case be seen as effectively being larger. It will not introduce any other effects, since in scanning transmission X-ray microscopy only a certain point of the sample is imaged by the zone plate and the whole image is acquired by scanning over the whole sample. In a full-field transmission X-ray microscope, however, the astigmatism will also distort the image due to the reason mentioned above.

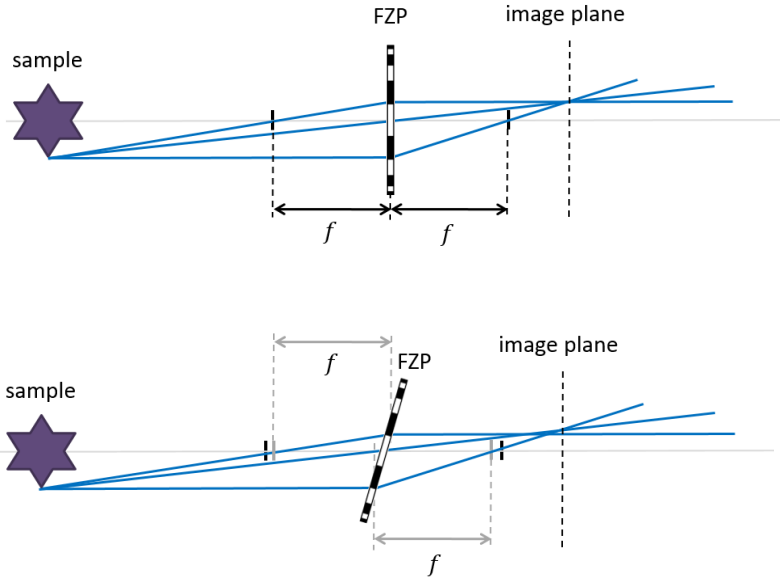

Figure 4.15: Imaging of a sample in transmission X-ray microscopy with a straight (top) and tilted (bottom) zone plate. With a tilted zone plate, phantom images are created in the image plane due to a mismatch of the focused rays from the sample.

As a concluding measurement a mesh-like scan was performed on zone plate iiB3, where the diffraction efficiency was recorded for a range of tilting angles in x and y simultaneously. The result is presented in Figure 4.16.

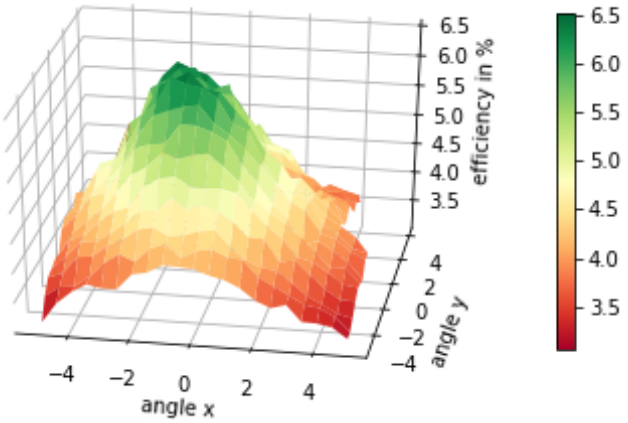

Figure 4.16: "Mesh" scan of the diffraction efficiency of zone plate iiB3 on sample VY181119a over a range of tilting angle combinations.

There is a clear peak in the surface plot, centered around (rot x, rot y) = $(-1°, -0.5°)$, well corresponding to the optimal values found in the previous measurements. This type of scan gives a more exact result for the optimal tilting position of a zone plate, but requires a lot more time. An equally reliable result was obtained by the two line scans as described earlier in this section.

5

Conclusion

In this master's thesis, a complete X-ray-tube-based setup has been built which enables measurements of the absolute diffraction efficiency of Fresnel zone plates. Not only an absolute value for the efficiency can be obtained, but also a spatially resolved map of it. In addition, the setup has a functionality which enables the measurement and compensation of the misalignment between the two halves of double-sided zone plates. A standard procedure for programming the measurements and processing the resulting data has been developed. The goals of this master's thesis can therefore be seen as reached. All of the measurements performed at the setup have been differential, using a set of filters of Cu and Ni, in order to monochromatize the broad X-ray tube spectrum down to a bandwidth of 0.646 keV. The choice of filters has been motivated through thorough characterization of the X-ray tube spectrum through simulations and spectrometer measurements which show a good correlation.

Measurements have been performed on both single- and double-sided zone plates, all fabricated during the course of the thesis, and the results have been compared. For the single-sided zone plates the maximum measured efficiency was 5.8% and for the double-sided it was 6.7%; the measurements revealed issues in the fabrication leading to large misalignments and size differences between the halves of double-sided zone plates, giving smaller efficiencies than expected.

Some of the measurements were compared to measurements performed at a synchrotron beamline, showing an excellent correlation in the diffraction efficiency mapping but some differences in the efficiencies. The agreement between the imaging results showed that the measurements at the X-ray tube setup are a very good replacement for the rarely possible measurements at a synchrotron.

The measurements with the X-ray-tube-based setup have given and will continue giving important information not only about the efficiency of double-sided Fresnel zone plates but also about their structure quality and alignment, providing insight and continuous feedback on the fabrication process. The availability and easiness in operation enables the systematic improvement of optics and gives strong advantages for the *X-ray Optics and Applications* group that would never have been possible with the limited access to beamtimes at synchrotrons.

Bibliography

[1] "X-ray Imaging." ESRF – The European Synchrotron. [online] Available at: http://www.esrf.eu/UsersAndScience/Publications/Highlights/2004/Imaging [Accessed 2018–02–20].

[2] B. Kaulich, P. Thibault, A. Gianoncelli, and M. Kiskinova, "Transmission and emission x-ray microscopy: operation modes, contrast mechanisms and applications," *Journal of Physics: Condensed Matter*, vol. 23(8), pp. 776–786, 2011.

[3] P. Willmott, *An introduction to synchrotron radiation: Techniques and Applications*. John Wiley and Sons, 2011.

[4] A. Snigirev and I. Snigireva, "High energy X-ray micro-optics," *Comptes Rendus Physique*, vol. 9, p. 507–516, 2008.

[5] "Synchrotron SOLEIL." Synchrotron SOLEIL. [online] Available at: https://www.synchrotron-soleil.fr/en [Accessed 2017–11–25].

[6] "X-ray Optics and Applications." Paul Scherrer Institut. [online] Available at: https://www.psi.ch/lmn/x-ray-optics [Accessed 2017–11–17].

[7] "ANATOMIX." Synchrotron SOLEIL. [online] Available at: https://www.synchrotron-soleil.fr/en/beamlines/anatomix [Accessed 2019–01–16].

[8] "Full-field Transmission X-ray Microscopy." Stanford Synchrotron Radiation Lightsource. [online] Available at: https://www-ssrl.slac.stanford.edu/txm/node/1 [Accessed 2018–03–09].

[9] "P05 The Imaging Beamline at PETRA III." Paul Scherrer Institut. [online] Available at: http://photon-science.desy.de/facilities/petra_iii/beamlines/p05_imaging_beamline/index_eng.html [Accessed 2019–01–23].

[10] "I13: X-ray Imaging and Coherence." Diamond Light Source. [online] Available at: https://www.diamond.ac.uk/Instruments/Imaging-and-Microscopy/I13.html [Accessed 2019–01–23].

[11] "TOMCAT – X02DA: Tomographic Microscopy." Paul Scherrer Institut. [online] Available at: https://www.psi.ch/sls/tomcat/tomcat [Accessed 2019–01–23].

[12] I. Mohacsi, I. Vartiainen, M. Guizar-Sicairos, P. Karvinen, V. A. Guzenko, E. Müller, E. Färm, M. Ritala, C. M. Kewish, A. Somogyi, and C. David, "High resolution double-sided diffractive optics for hard X-ray microscopy," *Optics Express*, vol. 23(2), pp. 776–786, 2015.

[13] S. Gorelick, J. Vila-Comamala, V. A. Guzenko, R. Barrett, M. Salome, and C. David, "High-Efficiency Gold Fresnel Zone Plates for Multi-keV X-rays," *10th International Conference on X-ray Microscopy*, vol. 1365, pp. 88–91, 2011.

[14] Z. Y. Zhang, C. L. Guo, R. Q. Wang, H. X. Hu, *et al.*, "Hybrid-level Fresnel zone plate for diffraction efficiency enhancement," *Optics Express*, vol. 25(26), pp. 33676–33687, 2017.

[15] "Fresnel Zone Plate Theory." CXRO – The Center For X-Ray Optics. Lawrence Berkeley National Laboratory. [online] Available at: `http://zoneplate.lbl.gov/theory` [Accessed 2018–03–08].

[16] D. A. Buralli and G. M. Morris, "Effects of diffraction efficiency on the modulation transfer function of diffractive lenses," *Applied Optics*, vol. 31(22), pp. 4389–4396, 1992.

[17] S. Werner, S. Rehbein, P. Guttmann, S. Heim, and G. Schneider, "Towards high diffraction efficiency zone plates for X-ray microscopy," *Microelectronic Engineering*, vol. 87(5-8), pp. 1557–1560, 2010.

[18] "X-ray Interactions With Matter." CXRO – The Center for X-ray Optics. [online] Available at: `http://henke.lbl.gov/optical_constants/` [Accessed 2018–02–20].

[19] H. W. Schnopper, L. P. V. Speybroeck, J. P. Delvaille, A. Epstein, E. Källne, R. Z. Bachrach, J. Dijkstra, and L. Lantward, "Diffraction grating transmission efficiencies for XUV and soft x rays," *Applied Optics*, vol. 16(4), pp. 1088–1091, 1977.

[20] J. Vila-Comamala, S. Gorelick, E. Färm, C. M. Kewish, A. Diaz, R. Barrett, V. A. Guzenko, M. Ritala, and C. David, "Ultra-high resolution zone-doubled diffractive X-ray optics for the multi-keV regime," *Optics Express*, vol. 19(1), pp. 175–184, 2011.

[21] K. Jefimovs, J. Vila-Comamala, T. Pilvi, J. Raabe, M. Ritala, and C. David, "Zone-Doubling Technique to Produce Ultrahigh-Resolution X-Ray Optics," *Physical Review Letters*, vol. 99, 264801, 2007.

[22] F. Marschall, J. Vila-Comamala, V. A. Guzenko, and C. David, "Systematic efficiency study of line-doubled zone plates," *Microelectronic Engineering*, vol. 177, pp. 25–29, 2017.

[23] K. Jefimovs, J. Vila-Comamala, T. Pilvi, J. Raabe, M. Ritala, and C. David, "Zone-Doubling Technique to Produce Ultrahigh-Resolution X-Ray Optics," *Physical Review Letters*, vol. 99(26), 2007. 264801.

[24] D. Paganin, *Coherent X-Ray Optics*. Oxford Series on Synchrotron Radiation, 2006.

[25] "Spectrometry of X-ray radiation fields." PTB – National Metrology Institute of Germany. [online] Available at: https://www.ptb.de/cms/en/ptb/fachabteilungen/abt6/forschungsnachrichtenabt6/news-from-the-annual-report.html?tx_news_pi1%5Bnews%5D=4482&tx_news_pi1%5Bcontroller%5D=News&tx_news_pi1%5Baction%5D=detail&tx_news_pi1%5Bday%5D=29&tx_news_pi1%5Bmonth%5D=9&tx_news_pi1%5Byear%5D=2008&cHash=ca29ab2a42c283fc29bf21126869455f [Accessed 2018–06–27].

[26] A. Thomson, D. Atwood, E. Gullikson, M. Howells, *et al.*, *X-ray Data Booklet*. Lawrence Berkeley National Laboratory, University of California, 2009.

[27] F. E. Zink, "X-ray tubes," *RadioGraphics*, vol. 17(5), pp. 1259–1268, 1997.

[28] "100 kV Microfocus X-Ray Source L10101." Hamamatsu Photonics. [online] Available at: https://www.hamamatsu.com/resources/pdf/etd/L10101_TXPR1012E.pdf [Accessed 2017–11–25].

[29] "List of classifications, volumes 1-121." World Health Organization – International Agency for Research on Cancer. [online] Available at: http://monographs.iarc.fr/ENG/Classification/latest_classif.php [Accessed 2018–06–14].

[30] "Deterministic effects." Radiopaedia. [online] Available at: https://radiopaedia.org/articles/deterministic-effects [Accessed 2018–06–14].

[31] C. A. Roobottoma, G. Mitchell, and G. Morgan-Hughes, "Radiation-reduction strategies in cardiac computed tomographic angiography," *Clinical Radiology*, vol. 65, pp. 859–867, 2010.

[32] A. G. Michette, G. R. Morrison, and C. J. Buckley, *X-Ray Microscopy III: Proceedings of the Third International Conference, London, September 3–7, 1990*. Springer, 2013.

[33] F. Zernike, "The phase contrast process in microscopic examinations," *Physikalische Zeitschrift*, vol. 36, pp. 848–851, 1935.

[34] G. Schmahl and D. Rudolph, *Proposal for a phase contrast x-ray microscope X-ray Microscopy: Instrumentation and Biological Applications ed P. C. Cheng and G. J. Jan*. Springer, Berlin, 1987.

[35] U. Neuhäusler, G. Schneider, W. Ludwig, M. A. Meyer, E. Zschech, and D. Hambach, "X-ray microscopy in Zernike phase contrast mode at 4 keV photon energy with 60 nm resolution," *Journal of Physics D: Applied Physics*, vol. 36, pp. A79–A82, 2003.

[36] C. Holzner, M. Feser, S. Vogt, B. Hornberger, S. B. Baines, and C. Jacobsen, "Zernike phase contrast in scanning microscopy with X-rays," *Nature Physics*, vol. 6(11), pp. 883–887, 2010.

[37] "pco.edge gold 4.2 deep cooled scientific cmos camera." PCO. [online] Available at: `https://www.pco.de/fileadmin/user_upload/pco-product_sheets/pco.edge_gold_42_data_sheet.pdf` [Accessed 2018–06–09].

[38] "Photon Counting Head H10682 Series." Hamamatsu Photonics. [online] Available at: `https://www.hamamatsu.com/eu/en/product/type/H10682-210/index.html` [Accessed 2017–01–17].

[39] "MOENCH: Micropixel with enhanced position resolution using charge integration." Paul Scherrer Institute - Detectors Group. [online] Available at: `https://www.psi.ch/detectors/moench` [Accessed 2018–06–09].

[40] S. Cartier, M. Kagias, A. Bergamaschi, Z. Wang, *et al.*, "Micrometer-resolution imaging using MÖNCH: towards g_2-less grating interferometry," *Journal of Synchrotron Radiation*, vol. 23(6), p. 1462–1473, 2016.

[41] "spec – Software for Diffraction." Certified Scientific Software. [online] Available at: `https://www.certif.com/content/spec/` [Accessed 2018–03–13].

[42] S. Chen, A. Lyon, J. Kirz, S. Seshadri, Y. Feng, M. Feser, S. Sassolini, F. Duewer, X. Zeng, and C. Huang, "Absolute zone plate efficiency measurement using laboratory X-ray sources," *Journal of X-Ray Science and Technology*, vol. 16, p. 235–241, 2008.

[43] "Simulation of X-ray Spectra – Online tool for the simulation of X-ray Spectra." Siemens Healthcare. [online] Available at: `https://www.oem-xray-components.siemens.com/x-ray-spectra-simulation` [Accessed 2018–06–26].

[44] "X-123CdTe Complete X-Ray & Gamma Ray Spectrometer." Amptek. [online] Available at: `http://amptek.com/products/x-123-cdte-complete-x-ray-gamma-ray-spectrometer-with-cdte-detector/` [Accessed 2018–06–08].

[45] "DPPMCA Display & Acquisition Software." Amptek. [online] Available at: `http://amptek.com/products/dpp-mca-display-acquisition-software/` [Accessed 2018–06–28].

[46] L. E. Ocola and V. R. Tirumala, "Nanofabrication of super-high-aspect-ratio structures in hydrogen silsesquioxane from direct-write e-beam lithography and hot development," *Journal of Vacuum Science & Technology B: Microelectronics and Nanometer Structures Processing, Measurement, and Phenomena*, vol. 26(6), 2008. 2632-2635.

[47] Y. Chen, H. Yang, and Z. Cui, "Effects of developing conditions on the contrast and sensitivity of hydrogen silsesquioxane," *Microelectronic Engineering*, vol. 83(4-9), 2006. 1119–1123.

A

Derivation of the effect of a pinhole on the X-ray tube spectrum

The following section describes the derivation of the influence of a pinhole of a certain size on the spectrum from the X-ray tube. The variables are as follows: g is the distance from the source to the zone plate, $d = 2 \cdot R$ the zone plate diameter, dr its outermost zone width, r_{cut} the remaining contributing radius of it after the cutting of the pinhole, h Planck's constant, c the speed of light, s' the pinhole size, b_1 the optimal working distance for the energy E_c, and $b_E(E)$ the working distance for an energy E.
Using

$$f = \frac{d \cdot dr}{\lambda} = \frac{d \cdot dr \cdot E}{h \cdot c} \tag{A.1}$$

and the lens equation

$$\frac{1}{g} + \frac{1}{b_1} = \frac{1}{f}, \tag{A.2}$$

the working distance of a zone plate for a certain chosen energy E_c can be written as

$$b_1 = \frac{g \cdot d \cdot dr \cdot E_c}{g \cdot h \cdot c - d \cdot dr \cdot E_c}. \tag{A.3}$$

The working distance for any other energy E can then be written as

$$b_E(E) = \frac{g \cdot d \cdot dr \cdot E}{g \cdot h \cdot c - d \cdot dr \cdot E}. \tag{A.4}$$

We now assume that for a certain zone plate, the pinhole has been put at the optimal working distance b_1 corresponding to the chosen energy E_c. The X-ray cones for energies $E \neq E_c$ will then be cut by the pinhole, as illustrated in Figure 3.8a. From the similarity of the triangle formed from the dark blue dashed cone emerging after the pinhole and the triangle of the dark blue cone, one can write the relation

$$\frac{s'/2}{b_E(E) - b_1} = \frac{r_{cut}}{b_E(E)}. \tag{A.5}$$

Re-expressing then yields

$$r_{cut}(E) = \frac{s' \cdot b_E(E)}{2 \cdot |b_E(E) - b_1|} \tag{A.6}$$

where the absolute value is used in order for the expression to apply to energies focused both too close and too far away compared to the pinhole position. This expression, where for a fixed value of b_1 the value from (A.4) for $b_E(E)$ was inserted as a function of energy, is the one which was used for the graphs shown in Figure 4.5a.

For the simulation of the corresponding intensity coming out of the zone plate as a function of energy, the efficiency profile shown in Figure 3.8b is expressed as a function of radius r and outer zone plate radius R:

$$\eta = \sin\left(\frac{\pi/2}{R} \cdot r\right) \tag{A.7}$$

from which the intensity from the total contributing area of the zone plate is derived by integrating over a circle with radius r_{cut}:

$$\begin{aligned}
I(r_{cut}) &= \iint\limits_{r<r_{cut}} \sin\left(\frac{\pi/2}{R} \cdot r\right) dA && \text{(A.8)}\\
&= \int_0^{r_{cut}} 2\pi \cdot r \sin\left(\frac{\pi/2}{R} \cdot r\right) dr && \text{(A.9)}\\
&= 4R \int_0^{r_{cut}} \frac{\pi/2}{R} \cdot r \sin\left(\frac{\pi/2}{R} \cdot r\right) dr && \text{(A.10)}\\
&= \left\{\frac{\pi/2}{R} \cdot r = y\right\} && \text{(A.11)}\\
&= \frac{8R^2}{\pi} \int_0^{r_{cut}\cdot\frac{\pi/2}{R}} y \sin y \, dy && \text{(A.12)}\\
&= \frac{8R^2}{\pi}\Big[y(-\cos y)\Big]_0^{r_{cut}\cdot\frac{\pi/2}{R}} + \frac{8R^2}{\pi} \int_0^{r_{cut}\cdot\frac{\pi/2}{R}} -\cos y \, dy && \text{(A.13)}\\
&= -4Rr_{cut} \cdot \cos\left(r_{cut} \cdot \frac{\pi/2}{R}\right) + \frac{8R^2}{\pi} \cdot \sin\left(r_{cut} \cdot \frac{\pi/2}{R}\right). && \text{(A.14)}
\end{aligned}$$

B

Collection of remaining single-sided Fresnel zone plate results

This Appendix presents the rest of the results from the diffraction efficiency measurements made during the course of this master's thesis. In each section, first a table with diffraction efficiency maps made with the Mönch are presented, followed by tables with the heights, maximum theoretical diffraction efficiencies, and measured absolute diffraction efficiencies of the zone plates.

B.1 Sample VY180821a "mark"

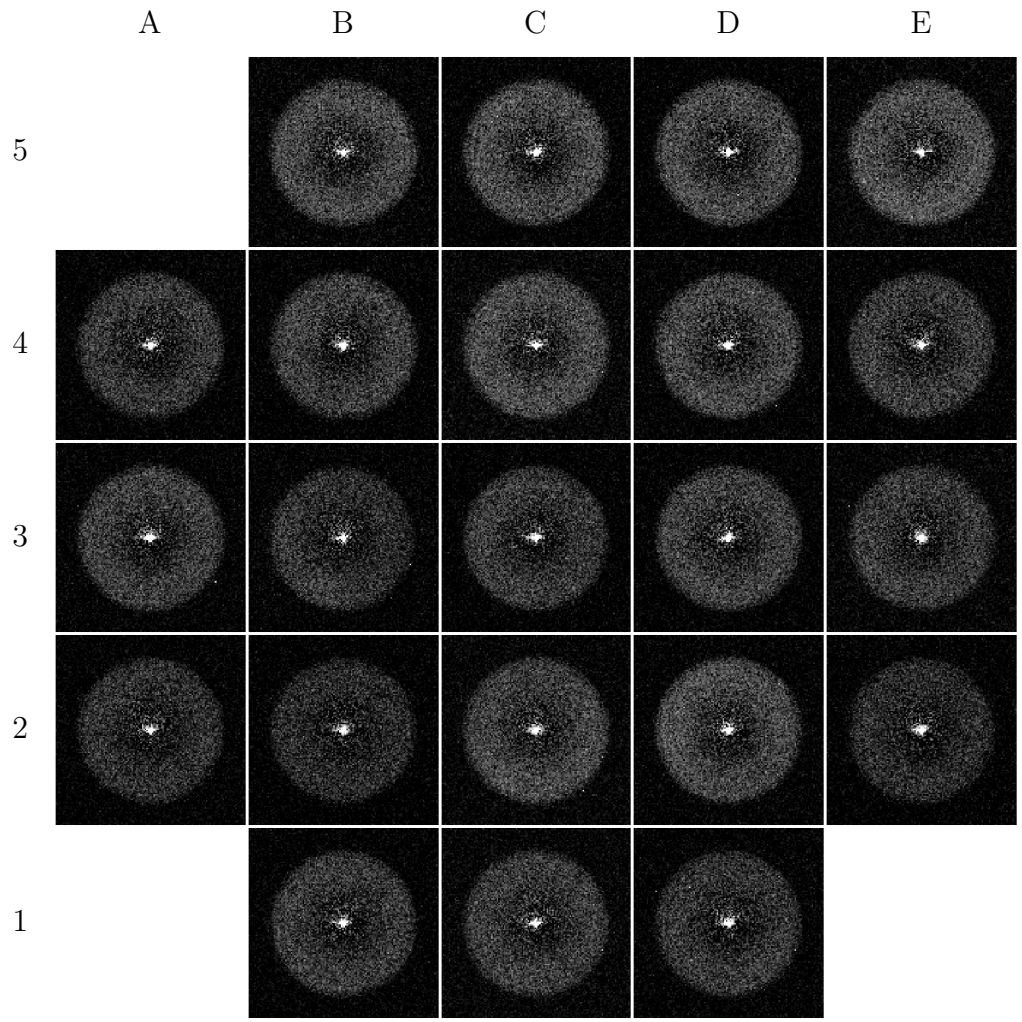

Table B.1: Mönch diffraction efficiency maps of sample VY180821a "mark".

	A	B	C	D	E
5		0.77	0.82	0.82	0.82
4	0.68	0.73	0.77	0.77	0.77
3	0.70	0.78	0.77	0.73	0.70
2	0.66	0.67	0.73	0.85	0.64
1		0.71	0.68	0.69	

(a) ZP heights in μm.

	A	B	C	D	E
5		18.6	20.4	20.5	20.3
4	15.5	17.4	18.6	18.8	18.9
3	16.3	19.1	18.9	17.4	16.3
2	14.8	15.2	17.4	21.3	14.3
1		16.5	15.8	16.1	

(b) Corresponding max. theoretical diffraction efficiencies in percent.

	A	B	C	D	E
5		4.5	4.8	4.7	4.9
4	3.6	4.3	4.5	4.4	4.0
3	4.0	3.9	4.1	4.1	3.6
2	3.4	3.4	4.2	4.8	3.0
1		3.8	3.7	3.6	

(c) Measured ZP efficiencies in percent.

Table B.2: ZP characteristics: VY180821a "mark".

B.2 Sample VY180827b "no mark"

This sample was made using hot development.

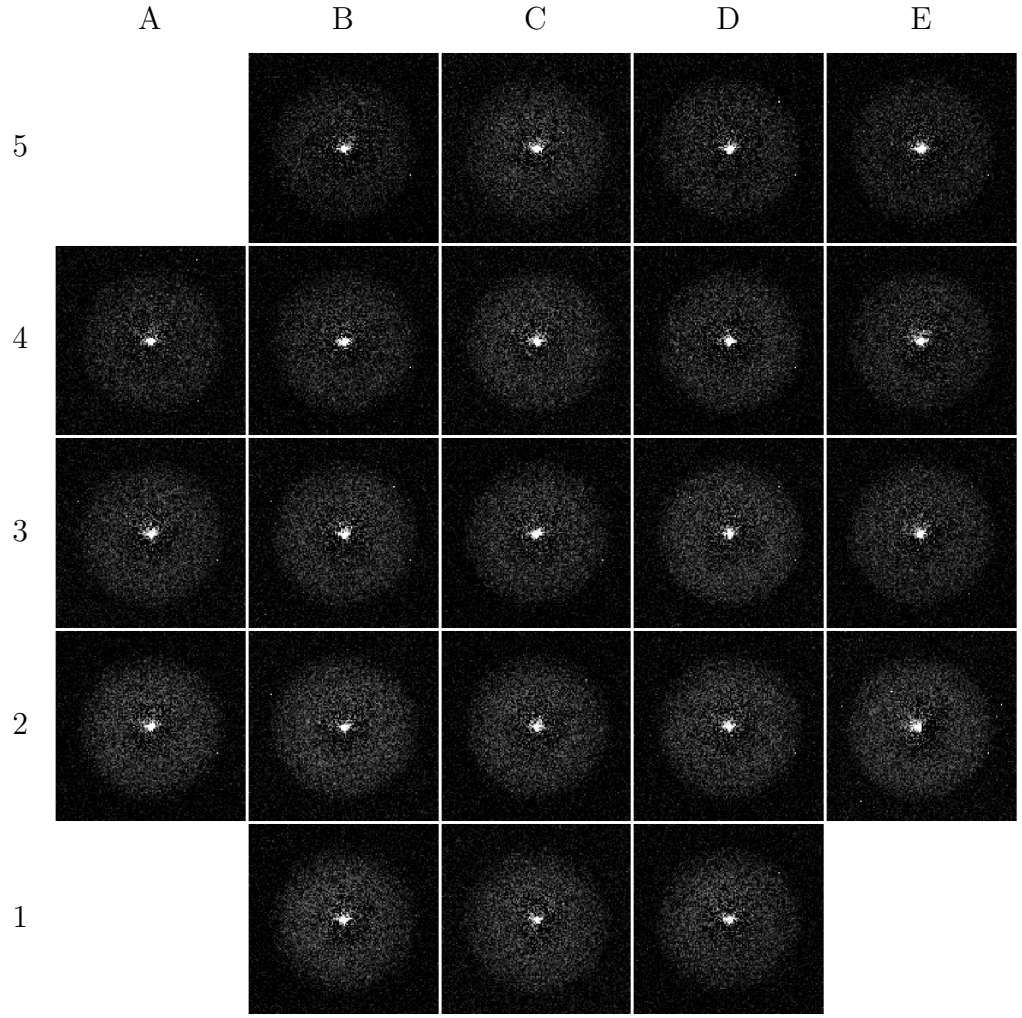

Table B.3: Mönch diffraction efficiency maps of sample VY180827b "no mark".

	A	B	C	D	E
5		0.56	0.68	0.58	0.48
4	0.52	0.62	0.62	0.59	0.56
3	0.59	0.65	0.68	0.64	0.57
2	0.81	0.74	0.77	0.71	0.64
1		0.81	0.85	0.78	

(a) ZP heights in μm.

	A	B	C	D	E
5		11.3	15.5	12.0	8.9
4	10.1	13.5	13.7	12.4	11.6
3	12.3	14.6	15.8	14.1	11.6
2	20.2	17.7	18.8	16.9	14.4
1		20.0	21.4	18.9	

(b) Corresponding max. theoretical diffraction efficiencies in percent.

	A	B	C	D	E
5		1.8	1.9	2.0	1.5
4	1.6	2.0	2.2	2.2	1.8
3	2.0	2.2	2.4	2.5	1.9
2	2.8	2.7	2.6	2.6	2.4
1		2.7	2.5	2.5	

(c) Measured ZP efficiencies in percent.

Table B.4: ZP characteristics: VY180827b "no mark".

B.3 Sample VY180919a "mark"

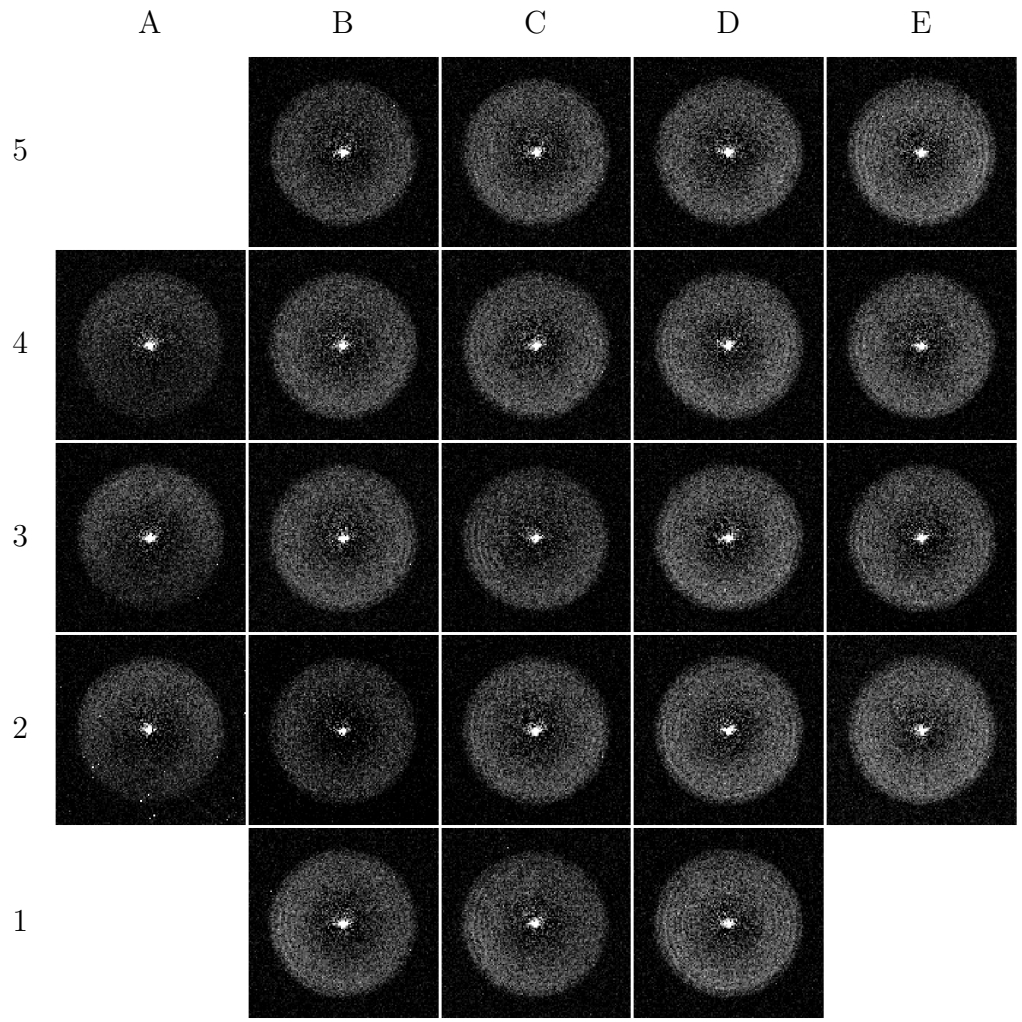

Table B.5: Mönch diffraction efficiency maps of sample VY180919a "mark".

	A	B	C	D	E
5		0.87	0.94	0.95	1.17
4	0.90	0.91	0.98	1.03	0.98
3	1.03	0.88	0.97	1.05	0.98
2	1.00	0.80	0.97	1.07	0.99
1		0.91	1.05	1.25	

(a) ZP heights in μm.

	A	B	C	D	E
5		22.0	24.2	24.5	29.4
4	23.1	23.4	25.3	26.5	25.2
3	26.5	22.4	25.0	27.1	25.2
2	25.9	19.7	25.1	27.5	25.5
1		23.2	27.1	30.6	

(b) Corresponding max. theoretical diffraction efficiencies in percent.

	A	B	C	D	E
5		4.3	4.7	5.1	5.8
4	2.6	4.5	4.9	5.5	5.1
3	3.4	4.4	4.5	5.4	5.2
2	3.3	3.6	4.8	5.5	5.3
1		4.7	4.7	5.7	

(c) Measured ZP efficiencies in percent.

Table B.6: ZP characteristics: VY180919a "mark".

B.4 Sample VY180919a "no mark"

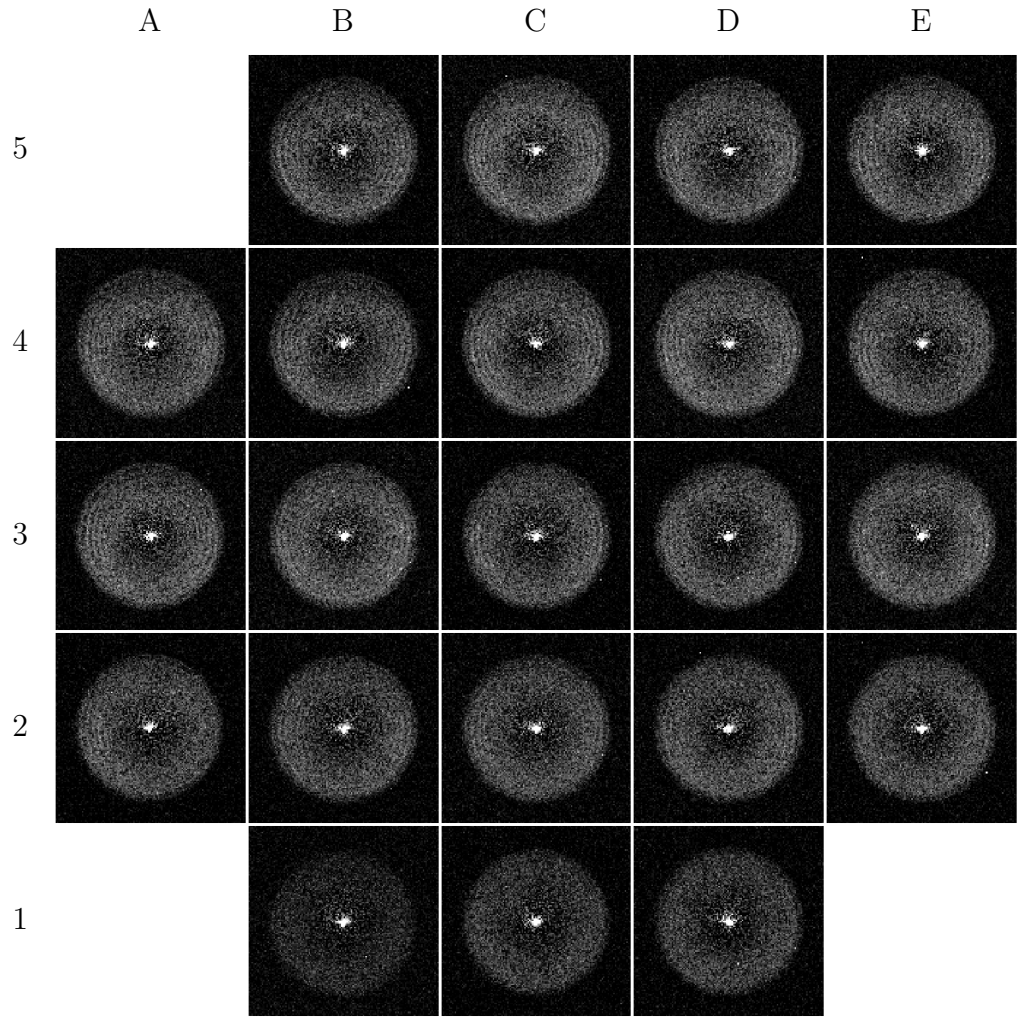

Table B.7: Mönch diffraction efficiency maps of sample VY180919a "no mark".

	A	B	C	D	E
5		1.36	1.27	1.26	1.26
4	1.35	1.31	1.23	1.17	1.17
3	1.30	1.10	1.06	1.01	1.02
2	1.07	0.92	0.94	0.92	0.87
1		0.71	0.81	0.82	

(a) ZP heights in μm.

	A	B	C	D	E
5		31.4	30.8	30.7	30.7
4	31.4	31.2	30.3	29.4	29.5
3	31.1	28.2	27.3	26.0	26.3
2	27.5	23.5	24.2	23.7	22.2
1		16.8	20.0	20.3	

(b) Corresponding max. theoretical diffraction efficiencies in percent.

	A	B	C	D	E
5		5.2	5.5	5.4	5.5
4	4.9	5.3	5.6	5.5	5.4
3	5.3	5.4	5.2	5.2	5.1
2	5.1	4.7	4.6	4.7	4.7
1		2.9	3.7	3.9	

(c) Measured ZP efficiencies in percent.

Table B.8: ZP characteristics: VY180919a "no mark".

B.5 Sample VY181015a ”no mark”

This sample was made using hot development.

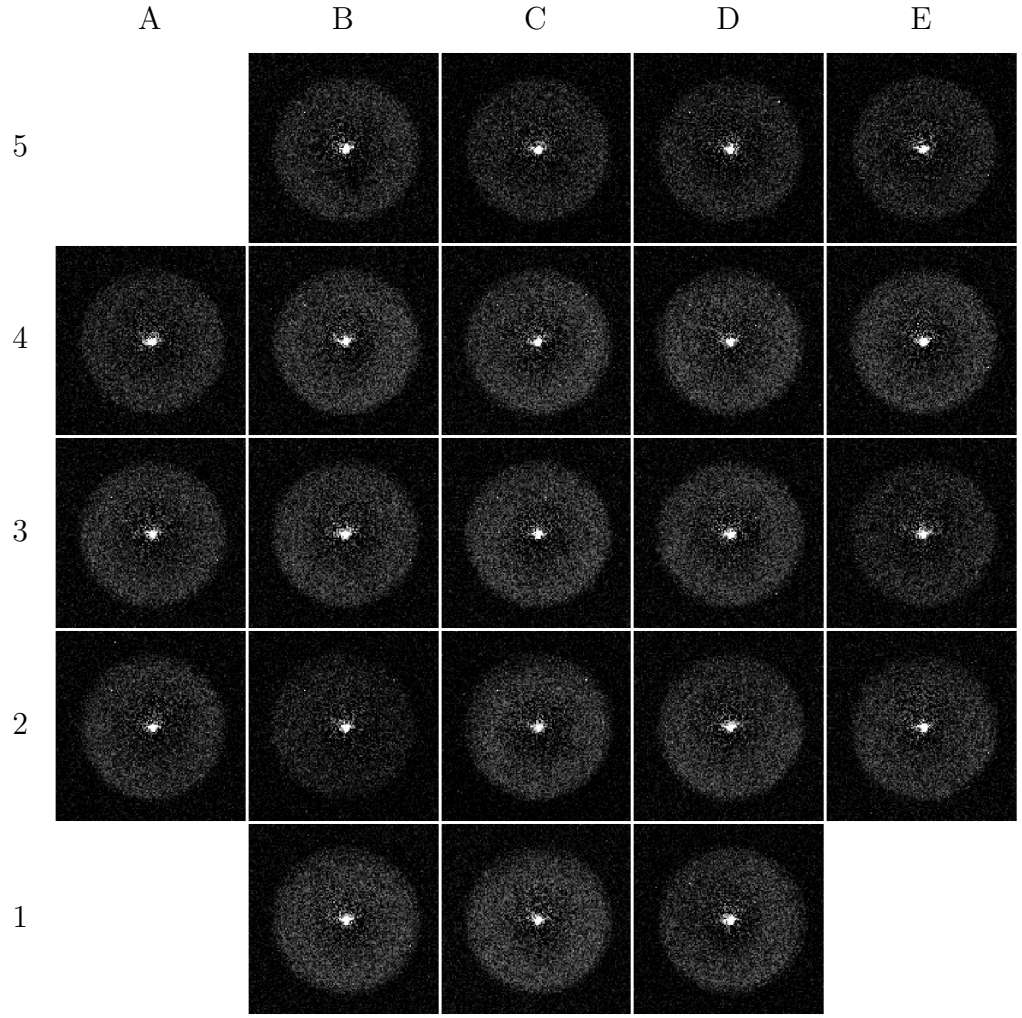

Table B.9: Mönch diffraction efficiency maps of sample VY181015a ”no mark”.

	A	B	C	D	E
5		0.59	0.61	0.63	0.56
4	0.60	0.78	0.71	0.93	0.72
3	0.70	0.70	0.77	0.73	0.59
2	0.67	0.83	1.00	0.60	0.98
1		0.97	1.00	0.66	

(a) ZP heights in μm.

	A	B	C	D	E
5		12.5	13.2	13.9	11.4
4	12.8	18.9	16.7	23.9	17.1
3	16.4	16.4	18.7	17.4	12.4
2	15.3	20.6	25.7	12.8	25.3
1		25.0	25.8	14.9	

(b) Corresponding max. theoretical diffraction efficiencies in percent.

	A	B	C	D	E
5		2.3	2.6	2.2	2.0
4	2.5	3.2	3.1	3.6	3.1
3	2.9	3.0	3.3	2.9	2.2
2	2.8	2.4	3.4	2.9	2.7
1		3.4	3.5	3.0	

(c) Measured ZP efficiencies in percent.

Table B.10: ZP characteristics: VY181015a ”no mark”.

B.6 Sample VY181015b "mark"

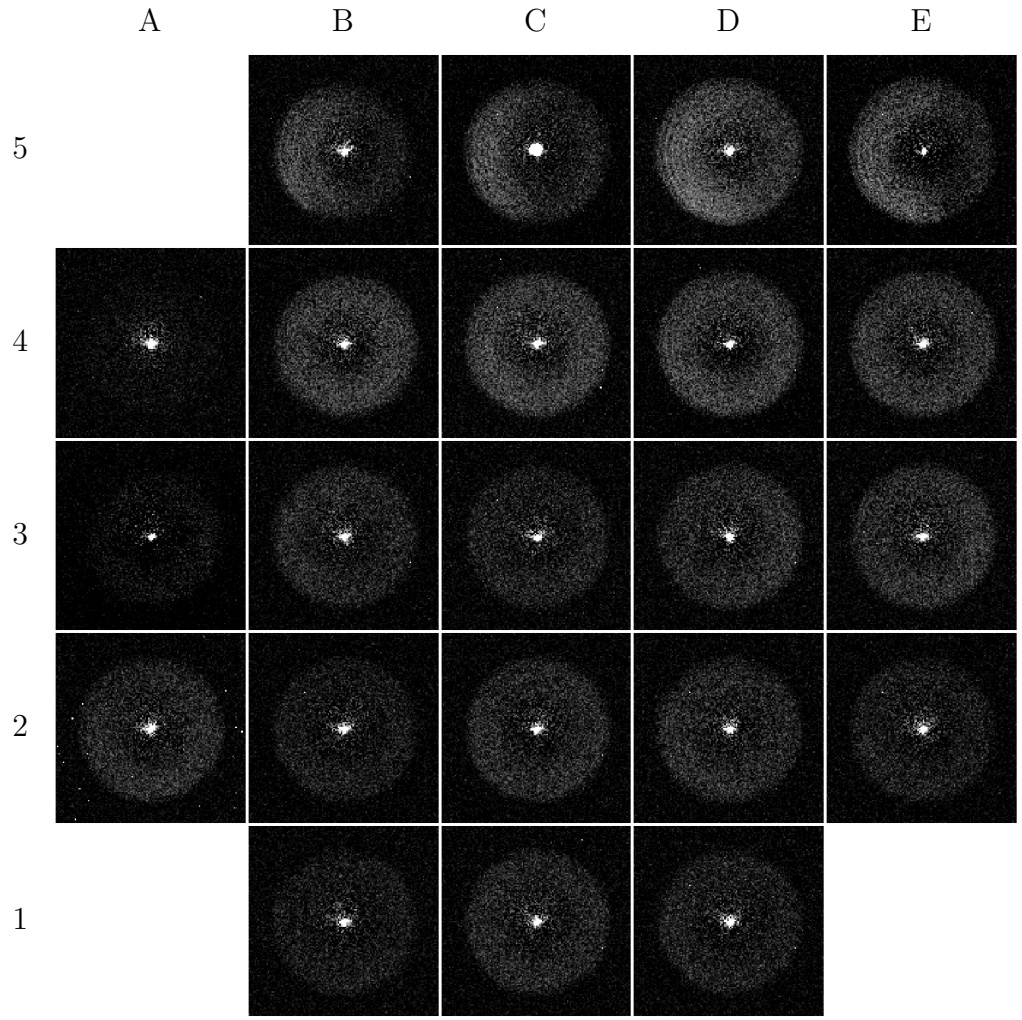

Table B.11: Mönch diffraction efficiency maps of sample VY181015b "mark".

	A	B	C	D	E
5		0.50	0.64	0.88	0.91
4	0.39	0.73	0.78	0.80	0.76
3	0.41	0.64	0.56	0.62	0.65
2	0.55	0.53	0.62	0.69	0.58
1		0.47	0.60	0.53	

(a) ZP heights in μm.

	A	B	C	D	E
5		9.4	14.2	22.3	23.3
4	6.1	17.5	19.0	19.6	18.5
3	6.6	14.3	11.6	13.5	14.4
2	11.2	10.3	13.4	16.0	12.1
1		8.5	12.9	10.3	

(b) Corresponding max. theoretical diffraction efficiencies in percent.

	A	B	C	D	E
5		2.4	3.1	4.2	2.0
4	0.6	3.4	3.7	3.8	4.0
3	1.2	2.3	1.9	2.5	2.8
2	2.3	1.7	2.5	2.6	2.0
1		1.4	2.3	1.8	

(c) Measured ZP efficiencies in percent.

Table B.12: ZP characteristics: VY181015b "mark".